Durham E-Theses

Fine structure in the charge ratio of cosmic ray muons at large zenith angles

Alexander, D.

Fine Structure in the Charge Ratio of

Cosmic Ray Muons at Large Zenith Angles

.

A Thesis submitted to the

University of Durham for the

Degree of·Doctor of Philosophy

——

D. Alexander, B.Sc.

October, 1970.

ABSTRACT

A horizontal spectrograph having a maximum detectable momentum of 200 GeV/c was constructed and used to measure the charge ratio of cosmic muons as a function of energy and zenith angle.

The effect of the earth's magnetic field on muon propagation in the atmosphere was evaluated and the observed ratios were corrected for this effect. The corrected ratios together with the results from the Japanese spectrograph, Kamiya et al. (1969), were examined in an investigation of the peaking in the charge ratio at muon energies $\sim$20GeV as observed in the results from the previous Durham spectrographs, Kelly et al. (1968).

The results of this investigation do not lend support to the existence of a fine structure at a unique energy of 20 GeV but high values of the charge ratio in the results from the present spectrograph at 40 GeV do indicate the possibility of a fine structure at an energy dependent on the azimuthal arrival direction of the muons. If this peaking is not of statistical origin then it would point to some further propagation effect. From the various possibilities considered, if such a fine structure is subsequently verified, it would appear that a further, detailed examination of the effect of Coulomb scattering on muon propagation in the atmosphere might profitably be pursued.

It was concluded, however, that although there exists the possibility of an azimuthal effect, the results point to those muons arriving at sea

level with energies < 150 GeV having been produced as a result of high energy nucleon interactions in the upper atmosphere with interaction characteristics conforming to the models discussed by MacKeown and Wolfendale (1966).

The spectrograph was also used in a subsiduary experiment to investigate the anomalous increase in the energy loss of relativistic charged particles in a plastic scintillation material as indicated by the results of Crispin and Hayman (1964), Smith and Stewart (1966) and Jones et al. (1968).

The results from this experiment point to normal behaviour of muons in the context of the Sternheimer energy loss theory.
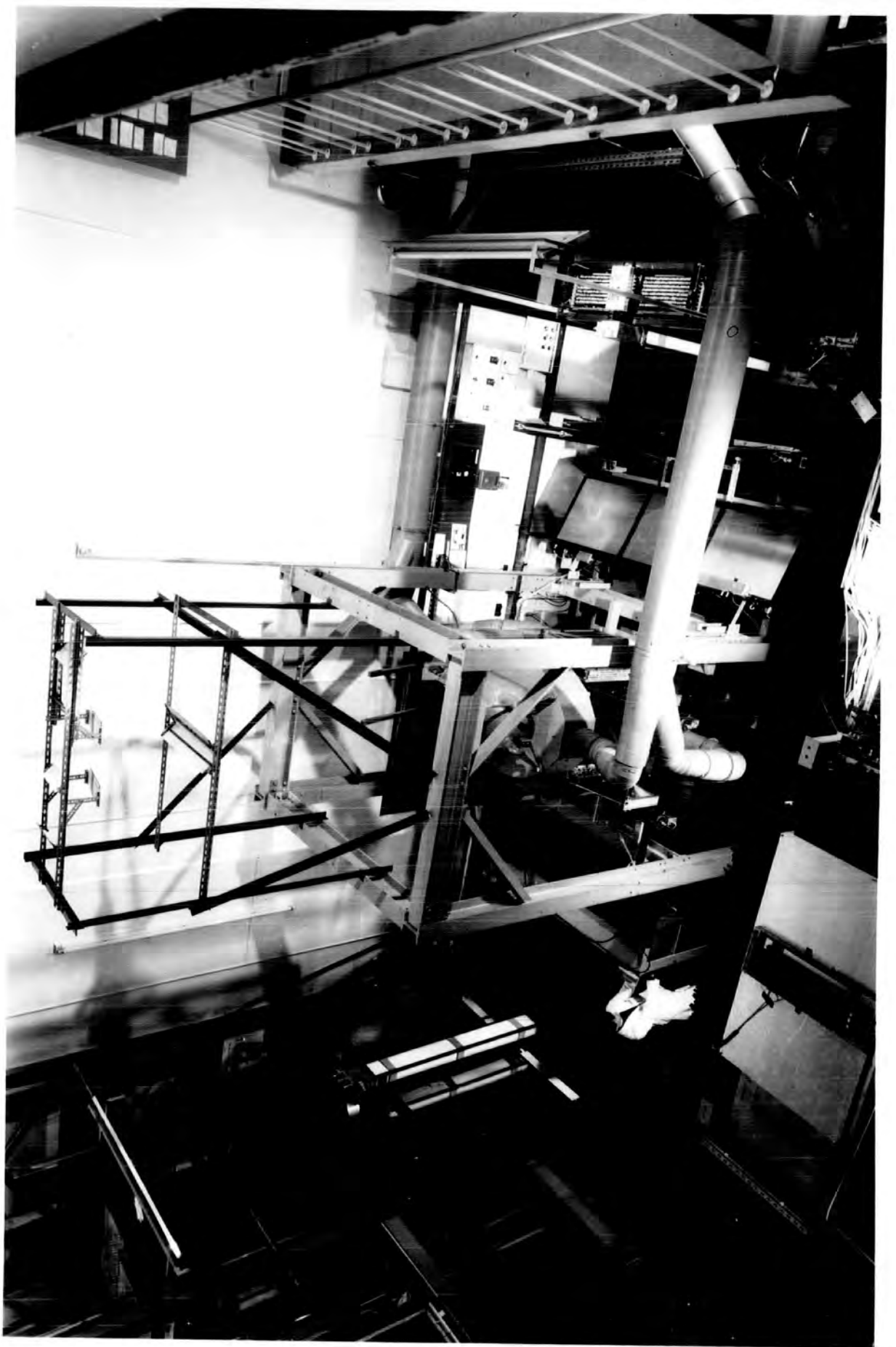
PREFACE

The work described in this thesis was carried out during 1967 - 1970 while the author was a research student under the supervision of Dr. M.G. Thompson, in the Cosmic Ray Group in the Physics Department of the University of Durham.

The author was solely responsible for the design, construction and running of the spectrograph, the data collection and its subsequent analysis and interpretation.

The experimental results were presented at the International Conference on Cosmic Rays, at Budapest (1969).

Work not described in this thesis, carried out during 1966-1967, on an earlier muon spectrograph and calculations on muon produced electron showers in air have been reported in papers Alexander et al. (1968a,b. 1969a).

The spectrograph as viewed from the western side of the

Sir James Knott laboratory.

The spectrograph as viewed from above the measuring

array D.

CONTENTS

CHAPTER 1

INTRODUCTION

1.1. The Cosmic Radiation

Since the turn of the century, when the existence of a cosmic
radiation incident at the top of the earth's atmosphere was first realized,
direct and indirect studies of this radiation have provided information
of great importance in the understanding of the very fundamentals of nature.
The impact that these studies have had has not only been in the initiation
of the whole field of elementary particle physics but also they have made
significant contributions to cosmology and astrophysics.

The character of the cosmic radiation has been examined directly in
investigations at mountain altitudes and in balloon, rocket and satellite
borne experiments. These experiments have established the energy spectrum
and have identified and measured the relative abundance of the major
components of the radiation up to energies as high as 2.10^{14}eV.

It has been found that the total energy spectrum falls off rapidly
with increasing energy. The exponent of the spectrum increases to a
constant value of -1.6 above a few Gev; the number of particles with
energies greater than 70 Gev is approximately 11 m^{-2}st^{-1}s^{-1}. The
results from the Russian Proton 1 and Proton 2 satellites, however,
are at variance with the above indicating an exponent of -1.7 over the
same energy range but credibility is given to the former "majority
results"-McCusker (1967).

At these energies, the radiation is found to be composed largely of protons, but nuclei with higher atomic number through to iron are observed with reasonable frequency. Nuclei as heavy as uranium have also been reported by Fowler et al. (1967). These results are of immediate astrophysical significance inasmuch as the contribution to the radiation from the heavier nuclei point to part of the radiation, atleast, originating from star systems in their later stages of evolution, supernovae for example.

Information on the primary spectrum beyond 10^{14}eV can only be obtained indirectly through studies of "Extensive air showers". EAS are produced from the secondary particles produced in the interaction of the cosmic radiation with the air nuclei of the upper atmosphere. In these interactions the secondaries are expected to be mainly pions. The charged pions, after production, have either the chance of decaying into muons or interacting with the air nuclei, whereas, the neutral pions, due to their relatively short lifetime of 10^{-16}s, will effectively decay spontaneously into two gamma rays producing large gamma-electron showers.

Broadly speaking, the nature and energy of the primary radiation is reflected in the total number and lateral distribution of the shower particles, that is, the electrons, muons and the hadrons in the shower core. For showers at maximum development, where the interpretation is insensitive to the interaction model parameters, it is found that the shower size is very nearly proportional to the primary particle energy. Absolute calibration, however, is closely related to the various model parameters.

The integral spectrum is now well established up to energies of about 10^{19}eV. The review spectrum of Greisen (1965) has been reproduced in fig. 1.1. At the highest energies, however, even with the largest air shower arrays, the detection rate is extremely small; only one shower to date has been detected with a size consistent with production by a primary of energy $\sim 10^{20}$eV, this being reported by Linsley (1963).

Information on the primary spectrum beyond 10^{20}eV is desirable for if there exists the 3°K black body radiation pervading the whole of space, the consequence of a "Primeval-fireball", then as pointed out by Greisen (1966), the photo-pion production could cause catastrophic modulation of the primary spectrum above 10^{20}eV. Apart from the giant air shower array at Sydney, a number of large aperture techniques are now being developed relying upon the remote detection of air showers. These methods, such as: radar detection, radio emmission detection and optical detection through ion-ization produced by the showers in passing through the atmosphere, have been reviewed by McCusker (1967).

The significance of the kink in the primary spectrum, in the energy range 10^{15}-10^{17}eV, is not clearly understood, however, it has been established that this kink is a characteristic of the cosmic radiation and is not due to a change in the shower production processes as was suggested by Reid et al. (1961). A reasonable explanation was put forward by Linsley (1962) who suggested that the magnetic fields in the spiral arms of our galaxy are strong enough to retain particles up to energies of 10^{15}eV. Above such energies, however, particles would be lost from the galaxy, the lightest particles going first. The

Fig. 1.1

Primary Energy (eV)
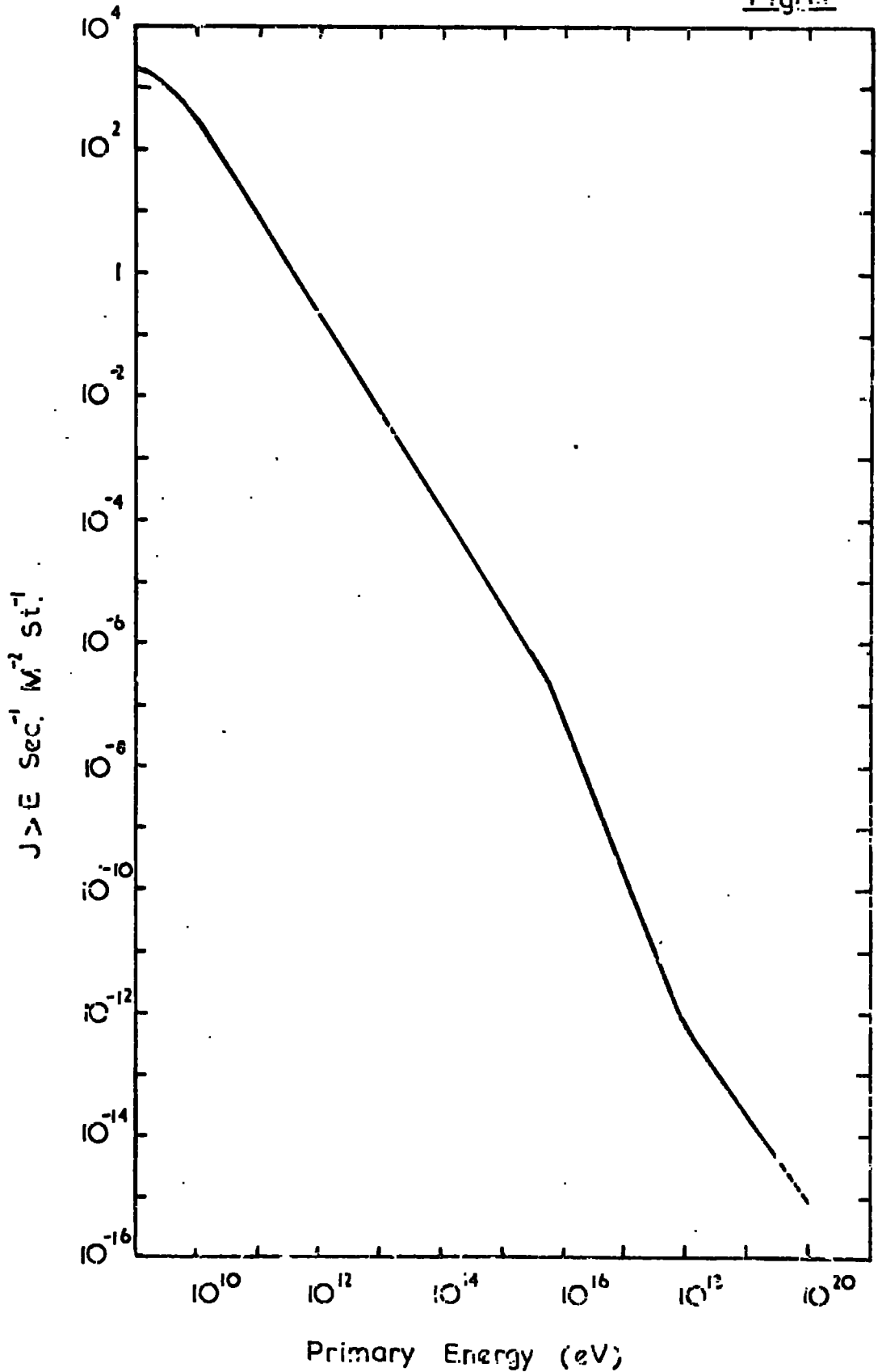
Integral Primary Spectrum—after Greisen 1966

levelling out of the spectrum beyond 10^{17}eV is to be attributed to a back-
ground radiation accelerated outside our own galaxy and as a consequence of
fragmentation of the heavy nuclei in inter-galactic space is expected to
be composed of protons.

1.2. Ultra High Energy Interactions

As a consequence of the rapid developments in accelerator technology,
it is now possible to produce protons in the laboratory with energies as
high as 70 GeV; the Serpukov 70 GeV proton synchroton produces a beam of
2.10^{11} particles every seven seconds. It is clear, from a consideration
of fig. 1.1, that experiments in an overlapping energy range using
accelerator beams are superior both qualitatively and quantitatively to
experiments relying upon the cosmic radiation as a nucleon source. The
cosmic radiation, however, can be considered as a source of particles
having energies extending many decades beyond the most optimistic
accelerator energy limit. In virtue of this energy range available in the
natural radiation and with the knowledge of it's energy spectrum and particle
composition, the cosmic ray physicists are able to pioneer the way not only
in those studies confined to investigations, at the highest energies, of the
behaviour of the interactions already observed in machine experiments but
also in investigations directed to looking for particle production processes
with threshold energies outside the range of present day machines.

Following such reviews as by Dekkers et al. (1965), Cocconi (1965)
and Koshiba (1967) on ultra high energy interactions observed in high
altitude experiments and EAS studies, then apart from some apparent large
values of the transverse momenta observed in EAS for interaction energies

$>10^{14}$eV, reported by such authors as Earnshaw et al. (1967), Miyake et al. (1968) and Matano et al. (1968) which, if real, could be explained in terms of quark production - McCusker (1967), the general characteristics of nuclear interactions, above a few GeV, would appear to be only slowly varying with energy, at most, and may be summarized as follows:

(a) The effective nucleon-nucleon inelastic cross-section is 44±6 mb from tens of GeV to tens of thousands of GeV.

(b) The average multiplicity of secondaries, mostly pions, is well represented by $\langle n \rangle \propto E^{0.25}$ although a logarithmic increase is favoured by many workers. E, here, is the total primary energy.

(c) The nucleon charge exchange probability is close to 0.5.

(d) The transverse momenta of the secondaries is well described by a Boltzmann distribution. For pions the average value is close to 0.4; this average appears to be closely related to the mass of the secondary.

(e) The average inelasticity of the proton is 40%, the surviving nucleon carrying away about 60% of the primary energy.

(f) Anisotropy in the angular distribution of the stable secondaries can be explained in terms of the isotropic decay of independent "Fireball centres".

(g) Isobar production is thought to be important in accounting for the long tail in the secondary particle energy spectra.

1.3. The Muon Charge Ratio

Muons, so far, have only been mentioned in the context of EAS but for the investigations of nucleon-nucleon interactions in the range 10^{11}-10^{14}eV, of no less importance are the studies on the unaccompanied muon component of the cosmic radiation at sea level. The importance of these muons stems from the major role that they play as the relatively stable, weakly interacting particles in the decay schemes of the possible secondary particles produced in the interactions of the primary radiation with the air nuclei of the upper atmosphere. The muons surviving to sea level, therefore, as a result of the primary radiation being largely protons (87% proton, 13% neutron), reflect the multiplicities, charge and composition of the secondaries produced. The relation between the spectra of the positive and negative muons is thus of particular importance and is conveniently expressed in terms of the charge ratio of the muons, R, or alternatively, expressed as a charge excess, δ , the definitions being as follows:

$$R = N^{+}/N^{-} \qquad \text{and} \qquad \delta = (N^{+}-N^{-})/(N^{+}+N^{-})$$

where N^{+} and N^{-} represent the numbers of the positive and negative muons observed over some energy range.

The experimental results on the sea level muon charge ratio have been reviewed by such authors as Puppi and Dallaporta (1952), Fowler and Wolfendale (1961), Aurela et al. (1966) and more recently by Flint and Nash (1970*). The combined results for energies greater than 1Gev

---

* In this review the results of the present work, as presented at the XIth International Conference on Cosmic Rays (Budapest) 1969, have been included.

have been reproduced in figs. 1.2 to 1.4; the data have been divided into groups representing large angle observations (a mean zenith arrival angle of 80°.) and those observations on the near vertical flux.

As a result of these surveys some general features have emerged and can be summarized as follows:—

(1) A ratio fairly well represented by a constant value of 1.25 over the majority of the energy range possibly reducing in the TeV range;

(2) A reasonable insensitivity of the ratio to the zenith arrival direction.

Any successful interaction model, as well as being consistent with these results, must take into account the general features of the interactions as summarized in the previous section. The general method followed is to compare the consequences of various models of particle production with the experimental data in the hope of distinguishing between one or other of these models. Those attempts at interpretation by authors to whom the more recent experimental data was available shall be summarized here.

a) <u>Quasi-statistical models</u>. MacKeown and Wolfendale (1966) considered phenomenological models characterized by pure pion production and also with mixtures of pion and kaon production. It became clear that pure pion production, even considering fluctuations in multiplicity and inelasticity, were not able to account for the observed ratios. The inclusion of a kaon component was significant due to the possible high K^{+}/K^{-} ratio which follows through strangeness conserving production

processes. The kaons were assumed to be produced in fixed proportions with the pions; the K^+/K^- ratio was taken to be energy independent. The results of this analysis are summarized in fig. 1.2. It can be seen that for an effective K^+/K^- ratio of 4 (a value consistent with present accelerator data - Liland and Pilkuhn (1969)) the kaons and pions would have to be produced in equal proportions for a best fit.

b) <u>Isobar production models</u>. If the excitation of isobaric states of the nucleon, as observed in accelerator experiments, continues up to high energies then, due to the high energy obtained by the pions produced in the de-excitation of these isobaric states and the rapidly falling primary spectrum, the effect on the muon charge ratio should be considerable.

MacKeown and Wolfendale (1966) considered the $N^*(\frac{1}{2}, \frac{3}{2})$ and $N^*(\frac{1}{2}, \frac{5}{2})$ isobars produced both with a constant total cross-section in the forward cone of 3 mb and also with a falling cross-section given by $\sigma = 9.65/\ln(E)$ together with a pionization process, as above, with a cross-section of 30 mb. The consequence of such a model can be seen in fig. 1.3; the dotted lines indicate the effect of the inclusion of a $K\Lambda$ decay mode for the isobars with a branching ratio $b = 0.10$.

Pal and Peters (1964) adopted a more general approach to the problem using the observed muon charge excess to determine some of the character-istics of an "average" isobar. In this treatment the isobar assumes a large excitation cross-section, the excitation probability being 0.7 ± 0.07; the average number of pions produced in the decay is 3.5 ± 0.15; the lower limit for the isobar mass is taken as 2200 MeV (chosen such that the maximum transverse momenta, as expected in a decay to the ground
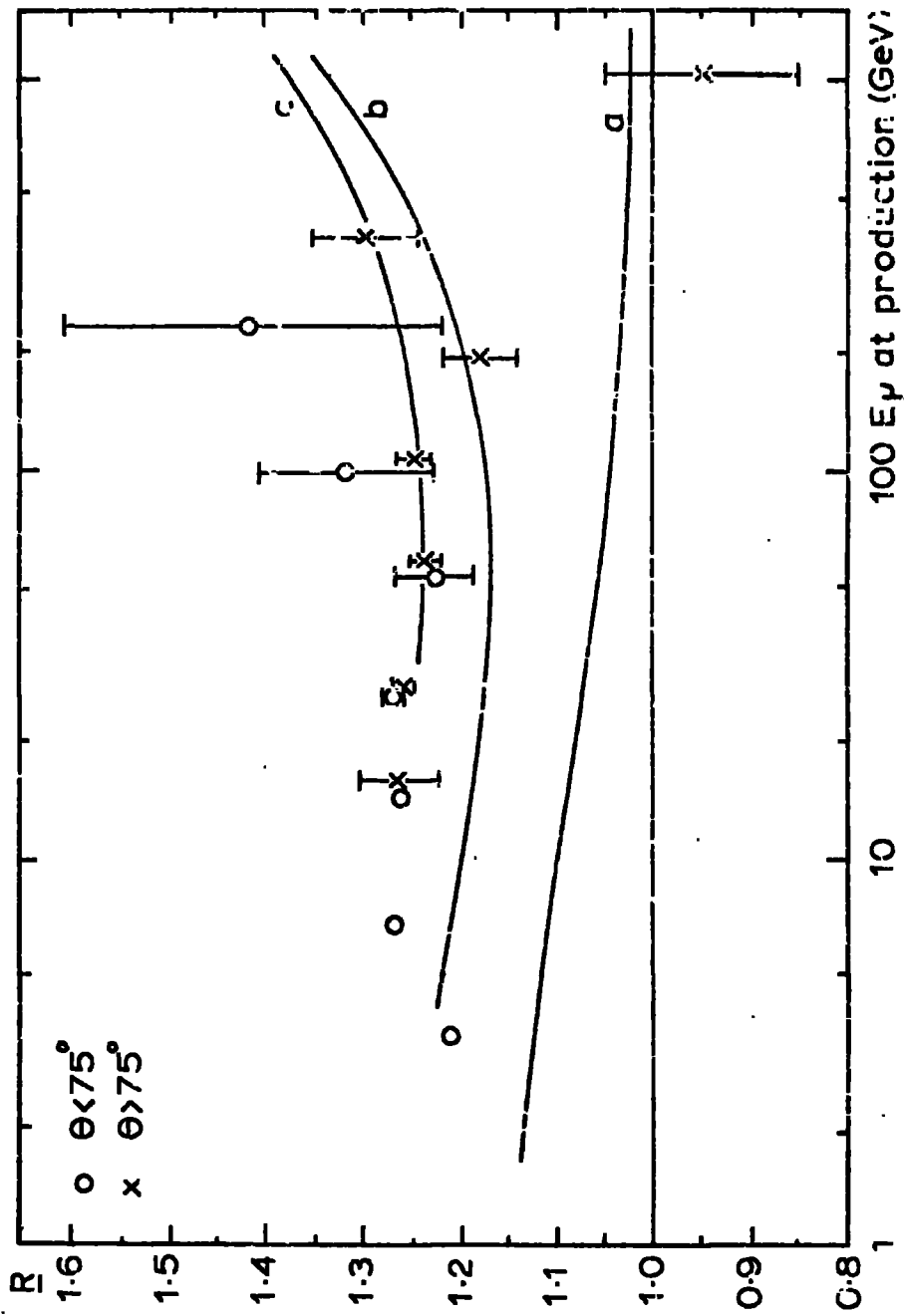
Fig. 1.2   The charge ratio for $\theta = 0^\circ$; (a) ionisation including fluctuations in multiplicity, (b) as (a) with $K/\pi = 0.2$ and $K^+/K^- = 4$, (c) as (b) with $K/\pi = 0.5$.
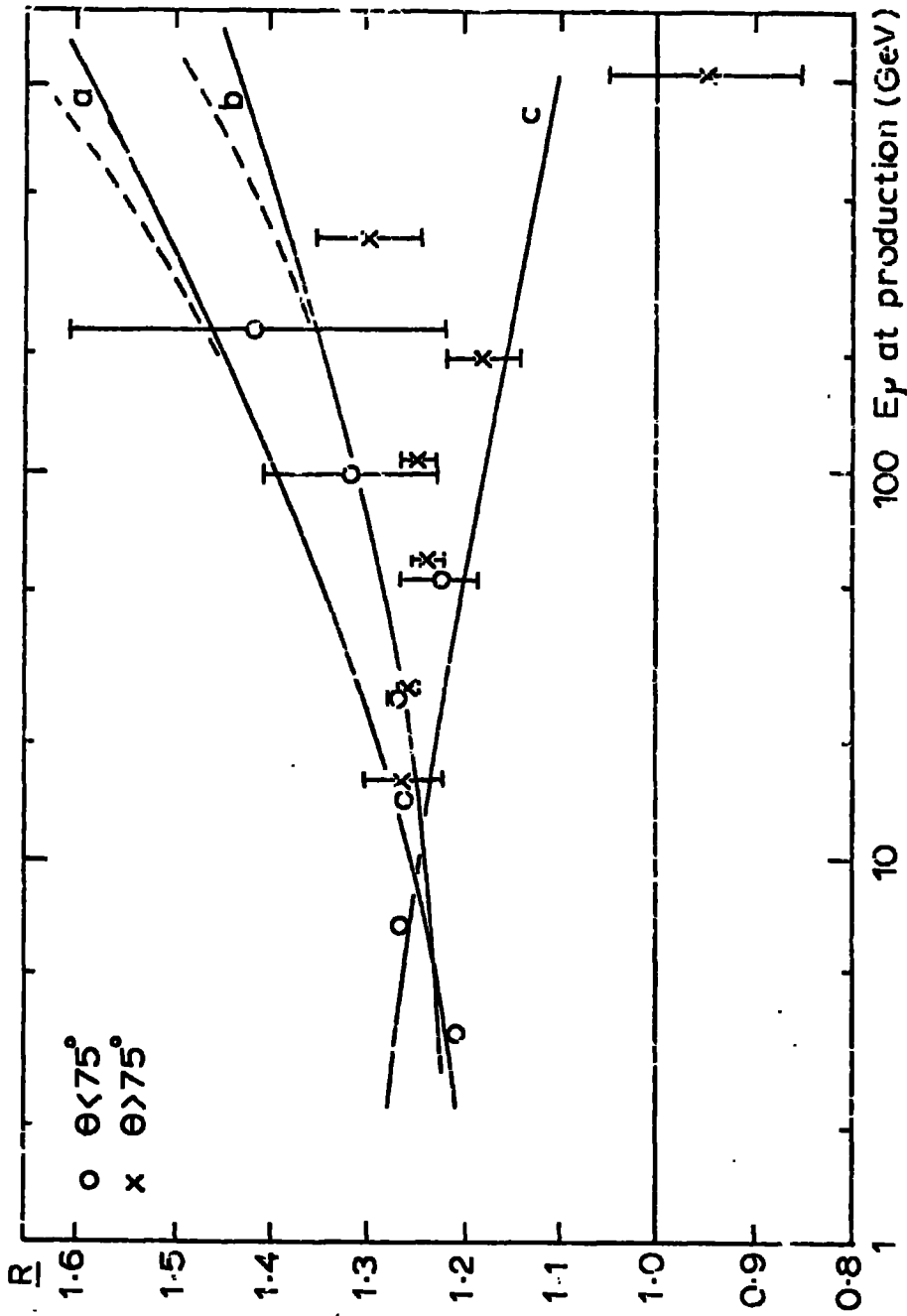
Fig. 1.3 The charge ratio for $\theta = 0^\circ$; (a) simple isobar model σ_I const., (b) as (a) but including fluctuations in pionisation, (c) with $\sigma_I \propto 1/\ln E$. The dashed curves show the effect of the $K\Lambda$ decay mode with branching ratio 0.10.

state, is 900 MeV/c, this being close to the upper limit normally encount-
ered experimentally); the net charge excess of the pions is 0.35; 25% of
the incident energy goes into the pion flux produced via isobar decay,
(15 -20)% of the energy going into particle creation in the c-system of
nucleon-nucleon collision. The consequences of such a description are
displayed in fig. 1.4; the effect of various values of the branching ratio,
b, for the decay mode $N^* \rightarrow K\Lambda$ is indicated. The experimental data can
be seen to be best described by this model for small values of b.

A further general isobar, the Aleph-baryon, although proposed by
Koshiba et al. (1968) in the context of nuclear emulsion jets, is worth
mention. For infact if the downward trend of the observed charge ratio
above a few hundred Gev is real, here could lie an explanation. The
excitation probability for the Aleph-baryon in inelastic collisions is
$< 2.10^{-3}$ for $E < 30$ GeV, 0.3 - 0.42 for $100 < E < 400$ GeV, 0.8 for 1000
$< E < 10,000$ GeV and is characterized by decay branching ratios of 70%
for Aleph $\rightarrow N + \phi$ and 30% for Aleph $\rightarrow N + \eta'$.

c) <u>The X-process</u>. The Utah experiment produced some rather
unexpected results on the muon spectrum as measured deep underground,
first reported by Bergeson et al. (1968). The results suggest that a
certain proportion of the muons are produced either directly or via some
short lived particle, so accounting for the apparent disappearance of
the so called "Sec θ enhancement" as would normally be expected for muon
production via meson decay. Although it is conceivable that some unseen
systematics might have influenced their observations on the muon spectrum
itself, it is unlikely that the charge ratio measurements would likewise
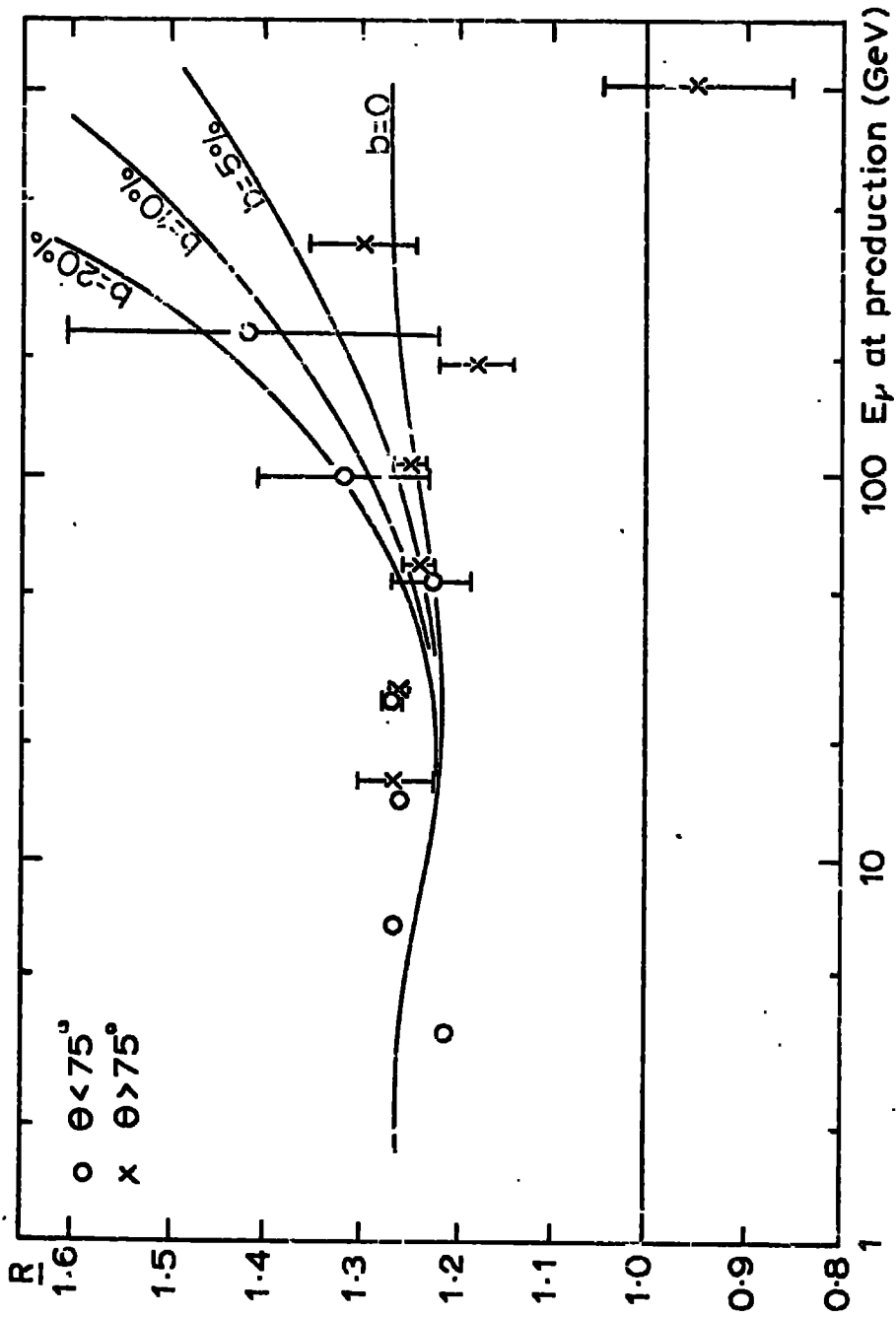
Fig. 1.4 The charge ratio for $\theta = 0^{\circ}$ as from the model of Pal and Peters (1964).

have been affected. The results of the measurements on the charge ratio of the underground muons, as produced by Parker (1969), are shown in fig. 1.5. The predictions of a simple model involving an X-process are also shown. The results appear to be consistent with an X-process with R=0.02, r_π = 1.25 and K/π =0.05, where R represents the fraction of muons produced via the X-process and r_π is the charge ratio of the muons produced through pion production - here r_x is assumed to be 1.0.

Apart from simple pionization, it is clear that there is little to choose between the models below ≈ 100 GeV and it is only at energies well above this that the model predictions become diverse. Noting that the model descriptions so far have been for the vertical direction only, of significance is; that due to the kaons having a shorter lifetime and greater mass than the pions then, if there is a sizeable kaon contribution to muon production, a variation in the charge ratio with zenith would be expected. In fig. 1.6 the expected variations in $R(0^{\circ})$ / $R(80^{\circ})$ for different kaon contributions are shown together with the observed variations as presented by Flint and Nash (1969). Although these results on the angular variation are not decisive, they do provide some indication of a kaon contribution to muon production. Clearly, taking the above considerations as a whole, it will not be until much more experimental data on the charge ratio above 100 GeV is available that any firm conclusions on the interaction mechanisms can be made nor is there any point in considering more sophisticated production models until that time.
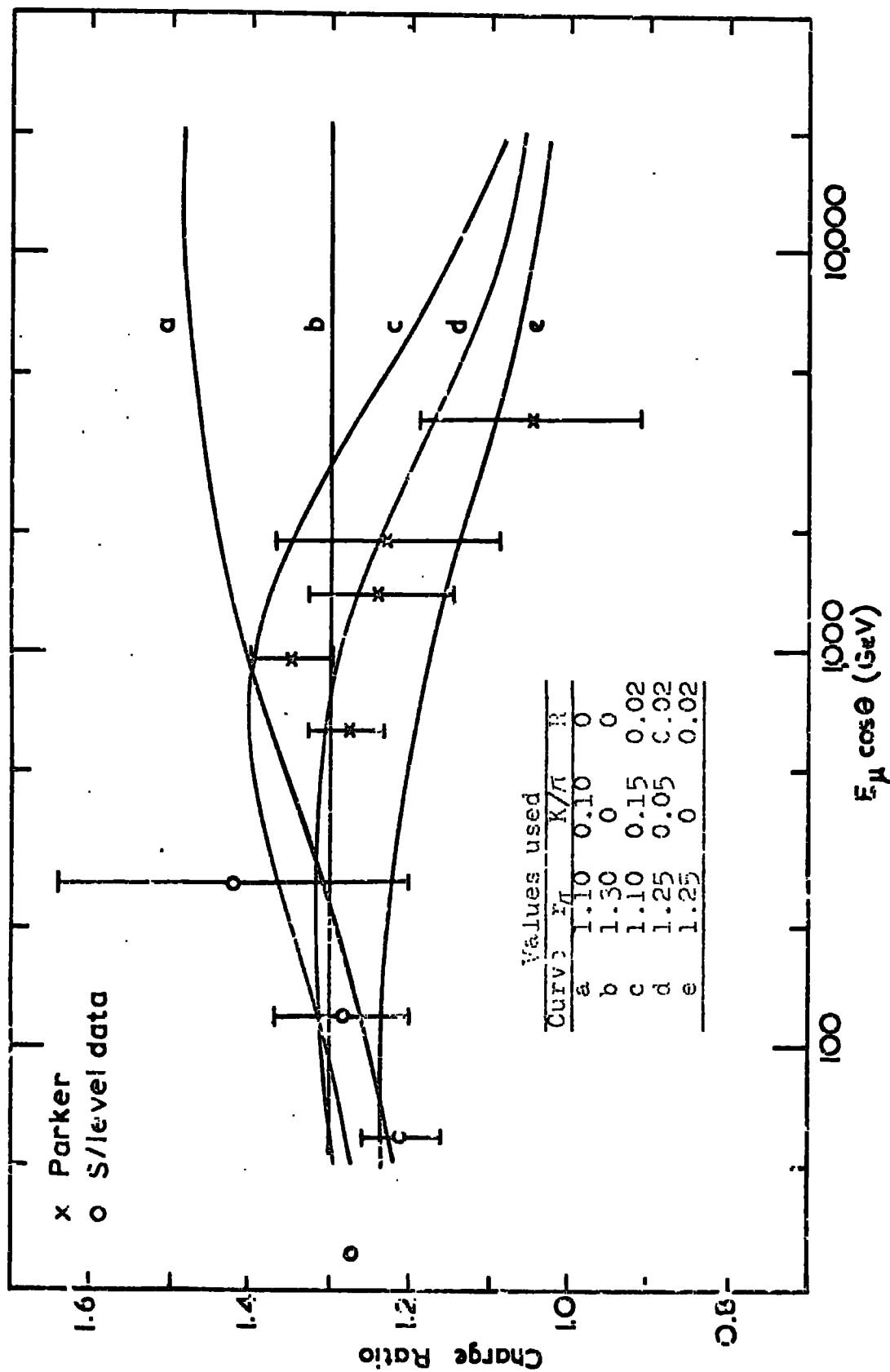
Fig. 1.5 Charge ratio from Tschbar model with $r_K = \infty$, $r_X = 1.0$, and other parameters as tabulated.
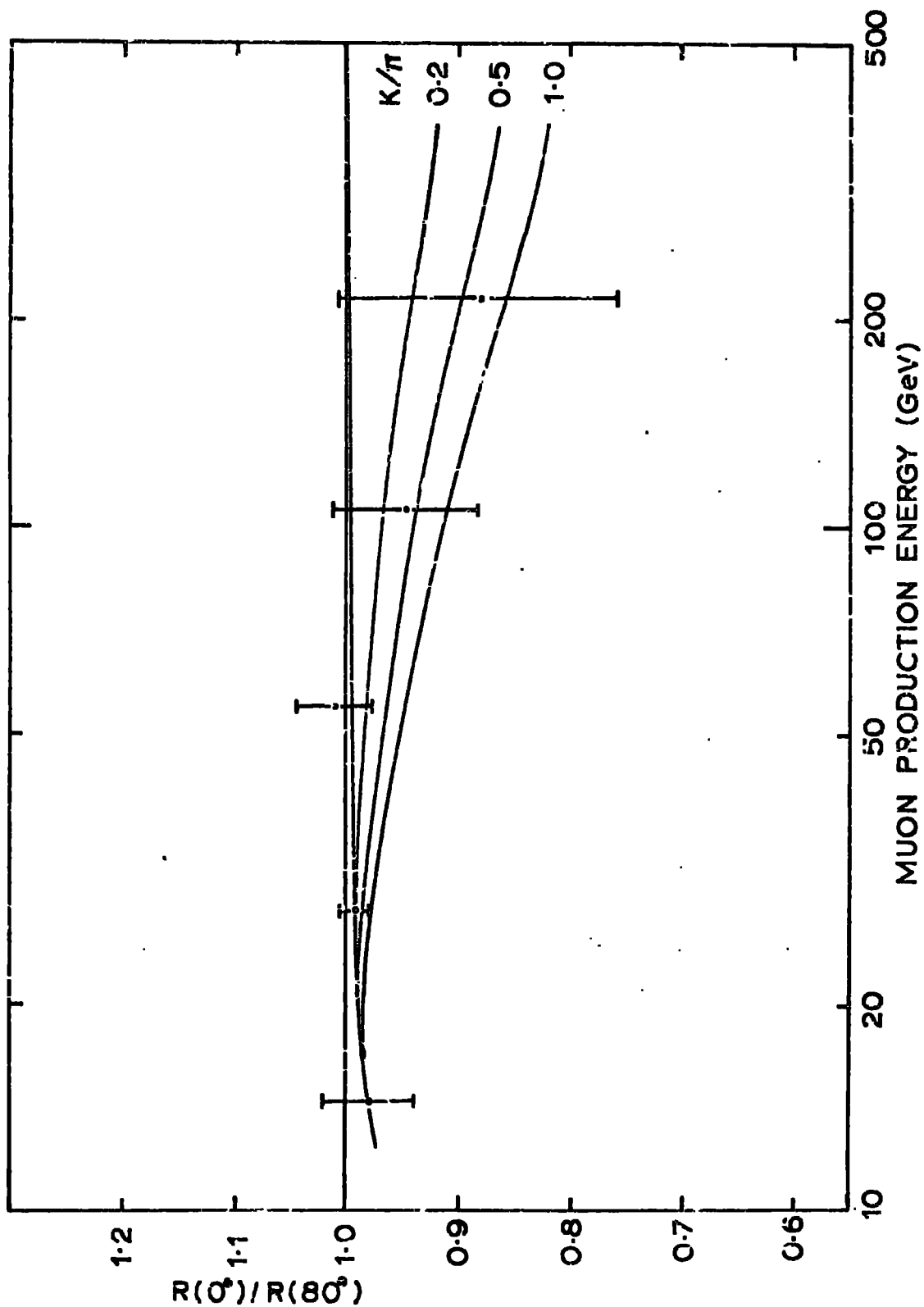
1.4. The Present Experiment

It can be seen from the discussion of the previous section that, as well as the necessity for an improvement in the statistics on the charge ratio data, model calculations provide the incentive for the experimentalists to extend measurements out to the highest possible energies. Kelly et al. (1968), however, drew attention to muon charge ratio measurements in the intermediate energy range 10-100 GeV. In their paper they produced the combined results of the two horizontal Durham spectrographs - Pattison (1963), MacKeown (1965) - plotting the ratios as a function of the muon sea level energy for various zenith angles in the range $77.5^{\circ} - 90^{\circ}$. These results have been reproduced in fig.1.7. These authors pointed out a rapid increase in the charge ratio with increasing zenith angle of muons arriving at sea level with energies close to 20 GeV.

The models considered so far can in no way account for such a narrow peaking in the charge ratio, especially as the peaking occurs at a unique sea level energy independent of the muon arrival direction. Also angular variations such as expected from a significant kaon production or through the dilution of the positive excess by muons produced in other than first generation collisions, at these energies, are small and in the wrong sense. It was suggested that such a fine structure might be explained by a possible difference in the behaviour of positive and negative muons or some neutral, weakly interacting particle having a lifetime of some 5.10^{-6}s which would have to decay preferentially into a positive muon.

The present work is concerned with the investigation of this apparent fine structure. For the purposes of these investigations a
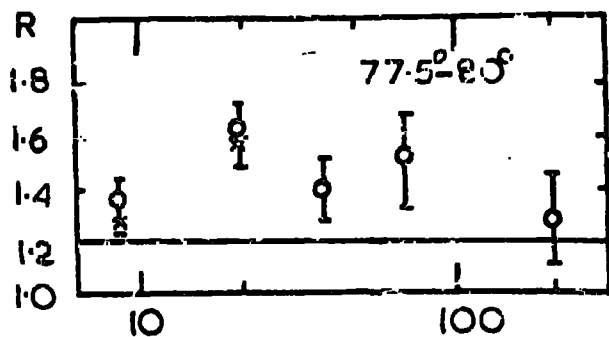
Fig. 1.7   Charge ratio results published by Kelly et al. (1968). Crosses represent the ratios before correction for the geomagnetic effect.
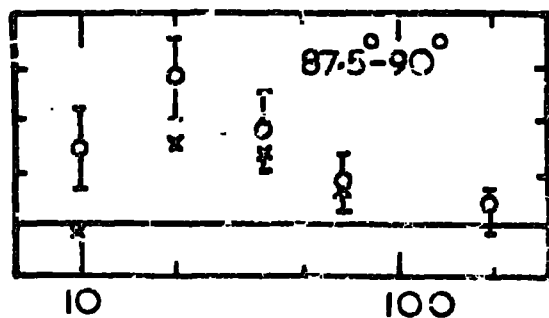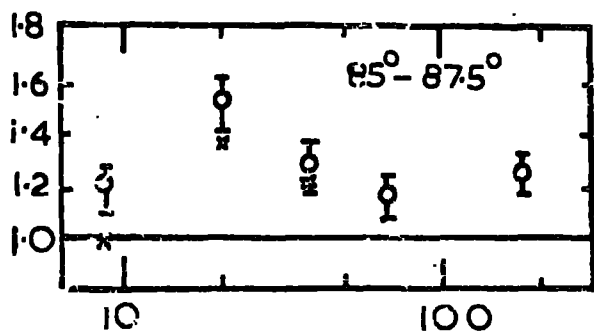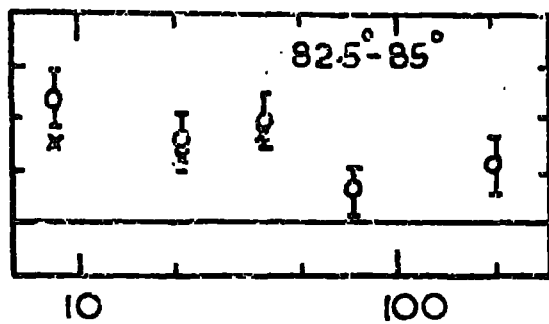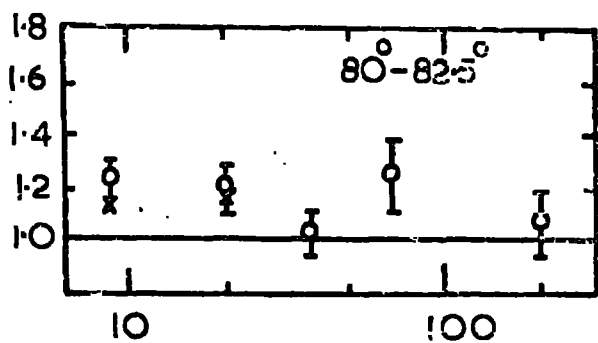
MUON ENERGY AT SEA LEVEL (GeV)

horizontal spectrograph was constructed having a maximum detectable momentum of about 200 GeV/c. This spectrograph differed from the previous Durham horizontal spectrographs inasmuch as the deflection was by means of an air gap magnet, in the horizontal plane, as opposed to a deflection in the zenith by a solid iron magnet and also, the axis of the present spectrograph lay along a line 27° East of the geomagnetic meridian as compared with 7.8° East for the previous spectrographs.

In the analysis of the data, special attention has been given to the modulation on the observed charge ratio through the effects of the earth's magnetic field. The results of this experiment together with other large angle data, notably that of Kamiya et al. (1969) have been compared with the previous Durham results in the investigation of a possible fine structure in the muon charge ratio in the energy range 10 - 100 GeV.

The spectrograph was also used in a subsidiary experiment to examine the energy loss of muons in a plastic scintillator material. The results of this experiment are discussed in the context of the anomalous increase in the energy loss of charged particles as reported by Jones et al. (1968). A report of this experiment appears in Appendix A.

CHAPTER 2

THE SPECTROGRAPH

2.1. Operational Principles

The force, F, acting on a charged particle moving in a magnetic field is given by

$$F = q \, (\bar{V} \times \bar{B}) \qquad (2.1)$$

where q is the charge of the particle, $\bar{V}$ the velocity and $\bar{B}$ the magnetic induction. Since the force experienced by the particle is normal to its direction of travel, then for a uniform magnetic field, the particle will follow a ⸗Spiral⸗ path with a radius, r, satisfying the relation

$$mv^2/r = q \, v \, b, \qquad (2.2)$$

alternatively written in the form

$$mv \, d\theta = q \, b \, dl, \qquad (2.3)$$

where b is the component of $\bar{B}$ normal to the direction of motion and dθ is the angular deflection suffered by the particle in travelling a distance dl in the magnetic field. The relations (2.2) and (2.3) are exact for all particle velocities providing m is taken to be the relatavistic mass of the particle. Expressing b in gauss, l in cm and representing the momentum mv in units of eV/c, denoted by p, the general form of equ. (2.3) becomes

$$\theta = 300 \int \frac{b.dl}{p} \text{ radians;} \qquad (2.4)$$

the integral is taken along the particle trajectory. Equ. (2.4) provides the basis of operation for all magnetic spectrographs.

The present spectrograph, which produced particle deflection in a horizontal plane between the poles of an air cooled electromagnet, is

illustrated in fig. 2.1. Detection of those particles traversing the
spectrograph was by means of plastic scintillation counters S1,S2,S3,
$\overline{S5}$ and $\overline{S6}$ and the liquid scintillation counters $\overline{A}$ and $\overline{D}$. The charged
particles passing through the counters caused ionization in the scin-
tillation material; the light so produced was converted into electrical
pulses by means of photomultiplier devices. The output pulses from the
photomultipliers were then passed to the spectrograph control unit. If
pulses arrived simultaneously from the counters S1,S2 and S3 and no
pulses arrived from counters $\overline{S5}$, $\overline{S6}$, $\overline{A}$ and $\overline{D}$, the occurrence of an event was
signalled. Counters $\overline{S5}$ and $\overline{S6}$ were incorporated in the spectrograph
design in order to provide a high immunity against unwanted triggers by
the numerous vertical multiparticle air showers. $\overline{A}$ and $\overline{D}$ covered gaps
in the flash tube arrays.

A,B,E,F,C and D were arrays of neon flash tubes (Conversi tubes). A
charged particle passing through these tubes would leave a number of ions
and electrons in its wake, and providing that a large enough electric field
was applied across the affected tubes within a few microseconds of the
passage of the particle, a glow discharge would develop along their lengths.
This discharge could be maintained for a few microseconds before self
quenching occured, allowing normal photographic techniques to be employed
in making a permanent record of those tubes which had flashed. A high
voltage pulse was passed to the flash tube arrays when the control unit
signalled an event, and the tubes which had flashed were photographed
through a system of mirrors. The particle trajectories were thus
permanently recorded for a subsequent analysis.

SPECTROGRAPH PLAN   Fig. 2.1
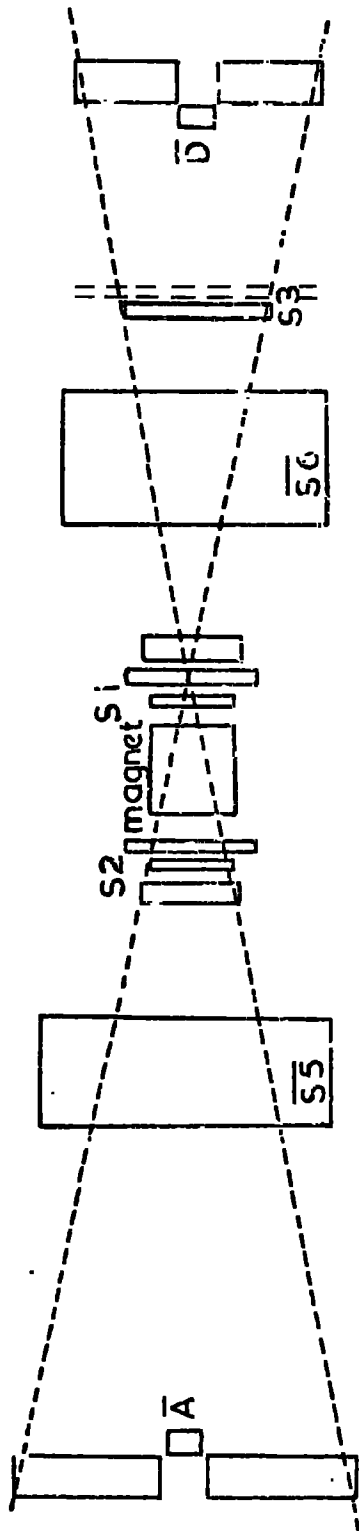
Scale 50cm

Deflection Plane
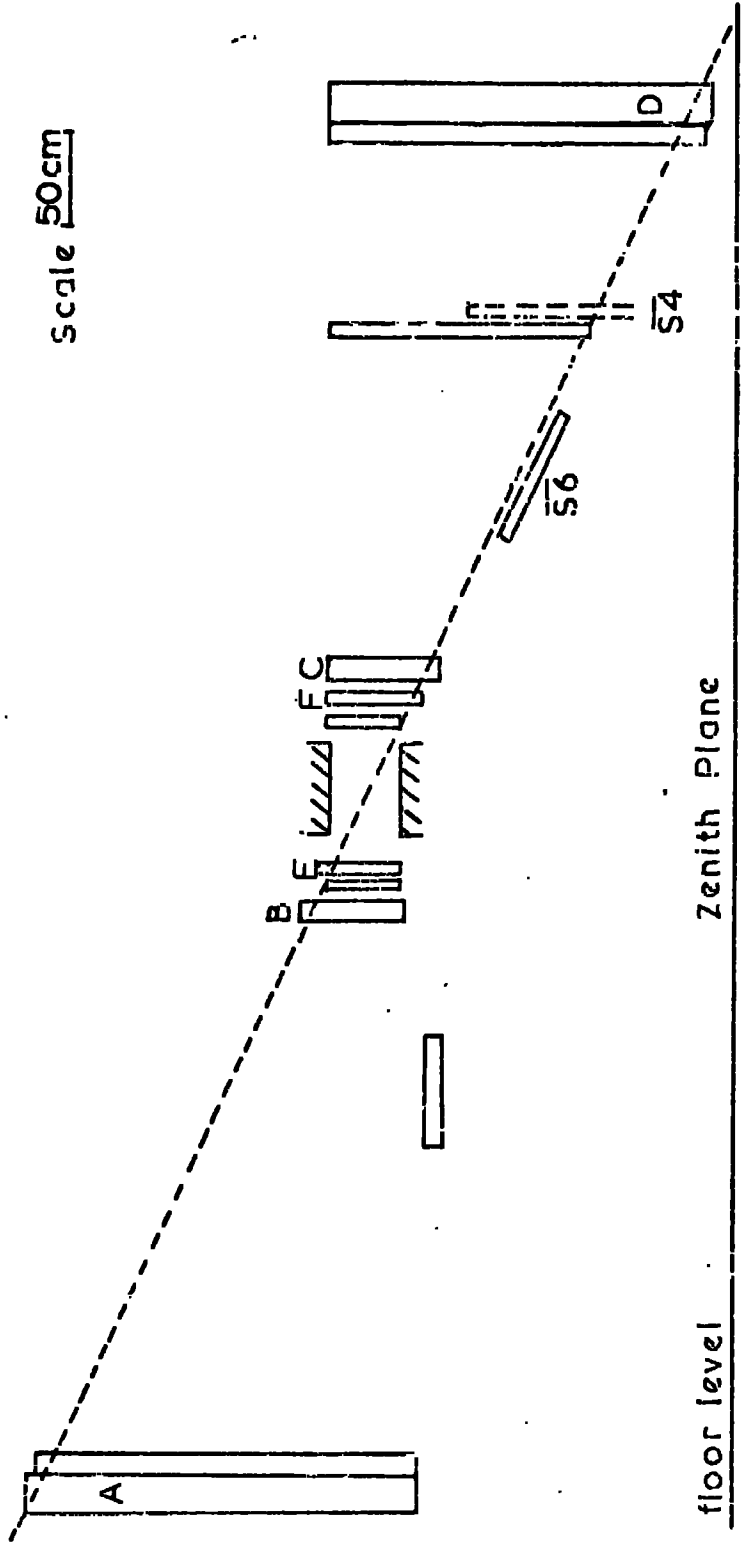
Zenith Plane

floor level

2.2. The Scintillation Counters

2.2.1. The Plastic Scintillation Counters

Phosphors of Ne 102 A material, the dimensions given in table 2.1., were viewed over their two shortest edges by means of 5 cm, 53 AVP photo-multiplier tubes, coupled by trapezoid light guides as illustrated in fig. 2.2a. The outputs from each end of the scintillation counter were added after the emmitter follower output stages. This design gives a good uniformity of response, discussed by Ashton et al. (1965).

As the performance of the photomultiplier tubes is severely affected by magnetic fields, magnetic shields, consisting of an inner mu-metal cylinder of diameter 5.9 cm and thickness 1 mm concentric with an outer steel cylinder of diameter 7.6 cm and thickness 0.45 cm, were fitted around the photomultiplier tubes. The shielding of the photocathode region is of particular importance, as here slow moving photoelectrons suffer the largest deflections. Due to the proximity of the counters, S1 and S2, to the magnet, the light guides were extended by the addition of 5 cm perspex cylinders of length 61 cm; the outer steel shielding was extended along the cylinder becoming part of the light tight system, fig. 2.2b. Due to variations in the direction of the magnetic field over the length of this steel tubing an axial field was induced within the shield. It was possible to reduce the effect of this field on the performance of the photomultiplier tube , to an undetectable amount, by extending the inner mu-metal shield a distance of it's radius beyond the photocathode. The photocathode was so situated in a region of minimum field; the field induced within the mu-metal cylinder at this point largely backed off the inducing axial field.

a) Counters S3,$\overline{S4}$,$\overline{S5}$,$\overline{S6}$
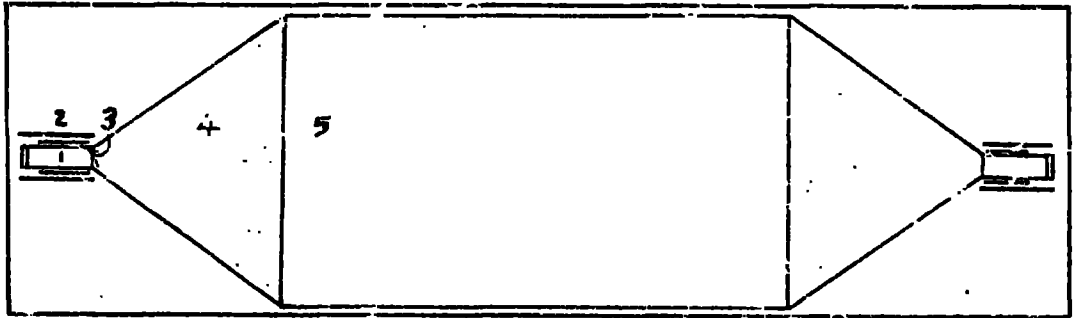
b) Counters S1,S2
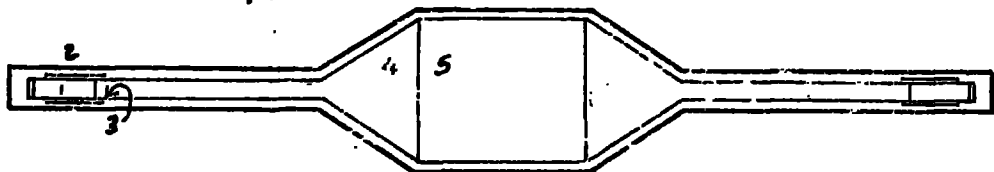
1)   Photomultiplier

2)   Steel cylinder

3)   Mu-metal cylinder

4)   Perspex light guide

5)   Phosphor

TABLE 2.1

The Dimensions of the Ne 102A Phosphors

Scintillation Counter	Length	Breadth	Thickness
S1	37.6	43.7	5
S2	37.6	43.7	2.25
S3	133	75	5
S4	133	75	5
S5	155	55	3.8
S6	133	75	5

(All dimensions in centimetres)

2.2.2 The Liquid Scintillation Counters

The scintillation counters, $\bar{A}$ and $\bar{D}$, were designed as a cheap addition to the spectrograph to .eliminate triggering by those particles which passed through the central gaps in the flash tube arrays, A and D, thus leading to a higher yield of useful events and a reduction in film consumption. The counters' dimensions were 200 x 10 x 17.8 cm and were constructed out of white opaque Darvic. The counters were filled with a liquid scintillator (liquid paraffin containing 0.5 g/l of para-terphenyl and 0.005 g/l of Popop, the additives acting as wavelengths changers). Mirrors were placed at the bottom of each counter; the scintillator being viewed from the top by two 53 AVP photomultiplier tubes.

2.3. The Flash Tube Detectors

The flash tube arrays consisted of rows of neon flash tubes. Separating each row was an aluminium sheet acting as electrode by which the high voltage pulse could be applied across the tubes. The type, dimensions and geometries for each array are summarized in tables 2.2a,b. Optical insulation, required to prevent sympathetic flashing between the flash tubes, was achieved by covering the large diameter tubes in Fablon tubing and by painting black the smaller high pressure tubes.

The high voltage pulses for each array were supplied from an RC system switched by means of a surge diverter (G.E.C E3073). The RC system was remote from the surge diverter; connection was by means of coaxial cables terminated at· the RC end by filters. For arrays B,E,C and F, of overall estimated capacitance 7,100 pf, the driving capacitor was a 0.05 mfd rapid discharge capacitor (Hivatronic) and for the arrays A and D, with capacitances of 9,400 pf and 7,000 pf respectively, two

TABLE 2.2a

Row Offsets* for the Flash Tube Arrays

Row	A(West)	A(East)	D(West)	D(East)	B	C	E	F
1	8.35	9.31	7.8	5.38	4.75	4.56	0.57	0.53
2	7.29	10.26	7.01	4.25	4.36	4.16	1.10	1.12
3	8.31	9.24	7.92	5.31	4.89	4.46	0.0	0.0
4	7.35	10.17	6.92	4.37	4.46	4.85	0.0	0.0
5	10.22	7.31	7.94	5.42	4.88	4.44		
6	7.35	10.04	7.04	4.48	4.46	4.85		
7	8.42	9.17	8.15	5.35	4.78	4.54		
8	7.48	9.99	7.22	4.60	4.37	4.14		

* The values in the table represent the position of the first tube in each row relative to some arbitrary reference line internal to each array. The references were on the west sides of arrays A, B, C and D, and for measurements in arrays E and F a base plate was used as reference. All distances are expressed in centimetres.

TABLE 2.2b

Array Tube Configurations and Characteristics

Arrays		A and D	B and C	E and F
Diameter(cm)	Internal —	1.513	0.587	1.550
	External —	1.742	0.766	1.786
Pressure (atm)		0.9	2.3	0.9
Length (cm)		200	45	70
Orientation		Vertical	Vertical	Horizontal
Tube spacing (cm)		1.905	0.799	1.775
Row spacing (cm)		2.8	1.0	1.8
Number of rows		8	8	4
Number per row		82/60	61/60	23/28

0.1 mfd capacitors (Plastic Capacitors Inc.) were used. The discharge resistance chain associated with each capacitor was of value 75 ohms.

The filter on the input to the capacitor system for arrays B,C,D and E was a low pass filter with a characteristic impedance of 75 ohms, a T- section filter terminated symmetrically by m derived half-filters, m = 0.67, giving an attenuation >50 db for frequencies higher than 3.9 mHz; the lower cut-off frequency was 2.0 mHz. A simple T-section filter of characteristic impendance 38 ohms, having a lower cut-off frequency of 0.8 mHz, terminated the two parallel 75 ohm input leads to the capacitor driving arrays A and D. The filters were included to eliminate a large high frequency component, with peak to peak voltages greater than 6KV, seriously affecting the rising edge of the RC pulse, a consequence of "jitter" in the switching characteristics of the surge diverter. This high frequency component adversely affected the performance of the flash tubes insomuch as it caused a drastic increase in the electron temperature in the neon so resulting in rapid diffusion of the electrons to the tube walls before the main body of the pulse had time to become effective. Results of measurements on the internal tube efficiencies, as converted from observed tube layer efficiencies, for the system with and without the filters, are produced in table 2.3. The time delay refers to the time interval between

Table 2.3.

Flash Tube Efficiency Measurements (%)

Arrays	Without filter Delay 34 μs	With filter Delay 34 μs	Delay 2 μs
B,C	47.5 ± 1.8	62.5 ± 2.5	97.4 ± 2.2
E,F.	59.5 ± 2.9	86.1 ± 2.6	100.1 ± 1.9
A,D	90.6 ± 1.7	92.7 ± 1.8	98.6 ± 2.0

the passage of the particle and the arrival of the high voltage pulses at each flash tube array. The errors quoted in the table include a contribution due to the uncertainty in the factor used in converting from layer efficiency measurements to tube internal efficiencies. The pulse shapes for the final working system including the filters are sketched in fig. 2.3.

In arrays B and C the flash tubes were not positioned symmetrically with respect to the electrodes and, in consequence, the discharge in those flash tubes which lay nearest the earth plates (the pulse was negative) appeared to be weak; infact, the discharge did not fill the whole tube but tended to track along the wall nearest to the earth plate. The intensity problem was resolved by the addition of a 2 cm extension of the electrodes. The extensions were constructed such that the plate separation at the tube extremities was equal to the tube external diameters; the higher field, and introduced symmetry, drew the discharge out across the tube.

2.4. The Magnet

The deflecting magnet was of Blackett type construction of overall weight 11 tons. A three phase supply was rectified providing a magnetizing current of 64 amps; the power dissipated in the magnet windings was 20 kW. The windings, enclosed in copper ducting, were cooled by means of a forced air current; the ambient temperature difference between air on input to that at output was $23^{o}C$. The pole pieces were 45 cm square set 38 cm apart, and operating at 64 amps the field at the centre of the air gap was 4kg. A switch in the current supply facilitated field reversal.

For the purposes of the experiment, the magnetic field was represented by a two dimensional, 10 cm matrix, which corresponded to the field

PULSE SHAPES

Fig. 2.3

Arrays B,C

Arrays A,D
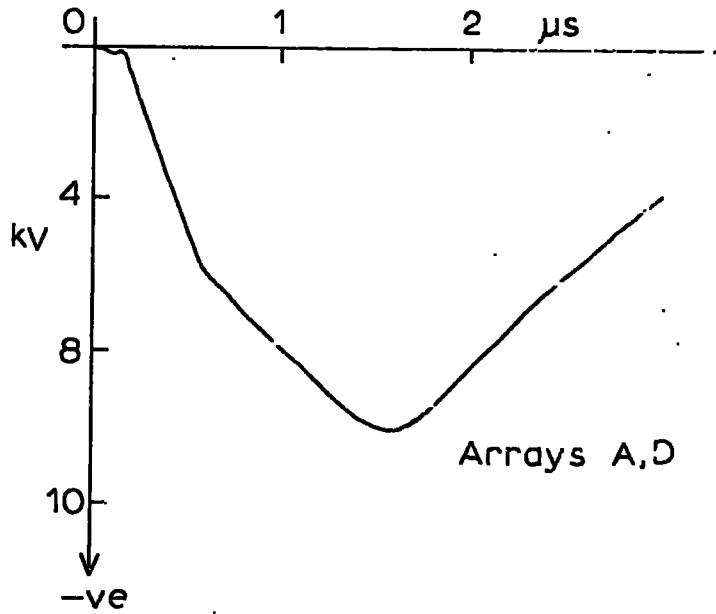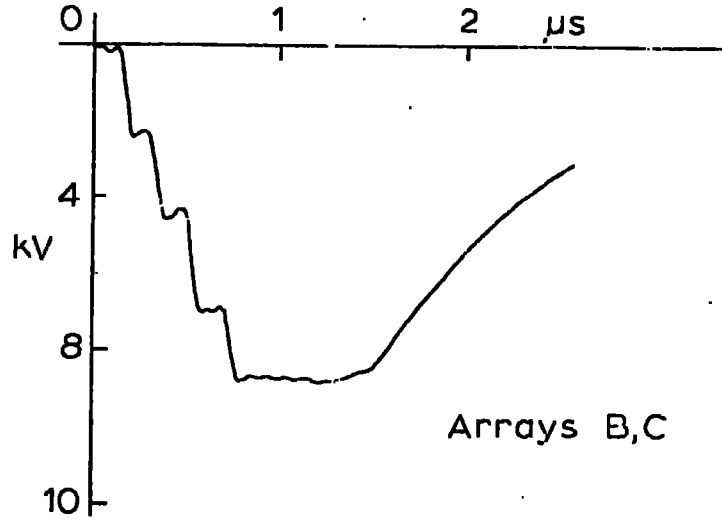
distribution across the horizontal plane which was intersected normally by the field lines. This matrix, fig. 2.4, was constructed from a three dimensional survey of the vertical component of the magnetic field using a search coil and flux meter. Calibration of the coil was carried out to within 2% by comparison with values obtained using a Hall probe in the magnet's fringe field. The Hall probe had been standardized using a standard permanent magnet. Direct measurements using the Hall probe between the magnet pole pieces were unreliable due to the wide temperature variations there.

In calculating the particle momentum, the field integral, $\int b.dl$, was taken as the line integral along the projection of the particle's trajectory on the field matrix plane. The finite deflection of the particles between the flash tube arrays A, B and C, D in the fringe field of the magnet amounted to an effective reduction in the line integral, as calculated between the arrays B and C, of some 2%.

2.5. The Optical System

To maximize efficiency in event recording, a mirror system was constructed such that each event could be recorded completely by one camera which was positioned on a platform on top of the magnet. The system consisted of two mirrors for each flash tube array. So that distortion was kept to a minimum, front silvered mirrors were used throughout the system except in the case of the two large mirrors associated with arrays A and D; these mirrors, each 7' x 1', were of plastic film construction.

As was shown by Coxell (1961), the light emitted by flash tubes is strongly collimated. In view of this fact, the mirrors were set so that the camera was able to view the centre of each array normally, but due

Figure 2.4

THE MAGNETIC FIELD MATRIX

86	136													136	86
110	175	303	515	850	1250	1580	1740	1680	1530	1230	836	493	300	175	115
128	205	350	590	1010	1510	1930	2120	2030	1850	1420	960	572		204	124
136	222	375	641	1085	1680	2084	2230	2190	2050	1665	1040	620		221	134
130	222	373	647	1092	1693	2080	2218	2190	2025	1622	1030	618	370	222	133
122	200	337	610	1030	1498	1948	2070	2052	1936	1440	962	565	338	203	122
100	165	275	530	870	1250	1580	1700	1690	1560	1230	82	470	280	168	100
73	127													125	72

B   POLE   C

each square = 10 x 10 cm.

1 unit = 1·748 gauss

to the extent of the arrays A and D, intensity variations across their width had to be considered. With the chosen optical path length of 7.7m, however, the existing intensity variation across these arrays was well within the exposure latitude of the film used. Compatible with this path length, a 90mm lens, having a maximum aperture of f2.8, was fitted to the camera.

The spectrograph was operated in total black-out with the camera shutter left permanently open. On the passage of a particle through the spectrograph, a system of fiducials on each array, a display system and a clock were illuminated before the film was automatically wound on to expose a new frame in readiness for the next event. The display system indicated the date, film number and the direction of the magnetic field. Due to the importance of knowing the field direction for the determination of the particle's charge, the magnetic field indicator was coupled directly to the field reversal switch, so elliminating any uncertainties as might be expected from a manual setting of the indicator.

The spectrograph, while operating at maximum aperture, exposed some 500 feet of film each week. For operational efficiency a film processing system, able to process 100 foot lengths of film, was designed. The film, Ilford HPS, was loaded into a 100 foot capacity spiral and was developed and fixed using standard techniques. The film was dried on a specially constructed foam covered drum; air circulation and drum rotation was maintained using compressed air. The air was heated by means of a 1 kW element stretched along the length of the drum.

2.6. Projection and Track Measurement

The events were projected onto an accurate diagram of the flash tube arrays (half scale). Each event was brought in turn onto the scanning table by means of a cam operated reeling system. The position of the particle in each array was located by laying a cursor along a line which passed through the maximum possible number of flashed tubes, avoiding all those tubes which had not flashed. A further restriction was imposed on the positioning of the cursor by taking into account the general line of direction of the trajectory as assessed from the flashed tube configurations in the other arrays. The point at which the cursor intersected a scale, scribed along the centre of each array, was recorded on a punched card together with such information as the field polarity, film number, time, date and type of event. This information was then transferred to magnetic tape for later analysis using the NUMAC IBM 360/67 computer.

2.7. Event Description

As the spectrograph only accepted those particles arriving with zenith angles greater than 65°, then due to the great thickness of atmosphere traversed, the particles accepted by the spectrograph could be considered to be entirely muons; the strongly interacting particles of the cosmic radiation having been absorbed (Kelly et al. 1968). The description of the muon trajectory, however, was complicated in some cases by locally produced muon induced electron bursts or knock on electrons produced by the muons in the measuring arrays themselves.

A system of event coding was employed by means of which the events could be typified. The code consisted of three characters, the first being

a number denoting the factors influencing the trajectory reconstruction, while the second and third characters denoted the array or arrays in which the measurements were affected. The coding was as follows:-

"1" - An uncontaminated trajectory for which straight forward reconstruction was possible.

"2" - Some contamination was observed but not severe enough to cause any uncertainty in the location of the true track.

"3" - The measurement was so affected that the position of the particle could not be recorded without ambiguity.

"4" - Two possible tracks of type "1" were observed in one or more of the arrays. In this case both possibilities were recorded sperately and where possible, in the final analysis, the computer selected those tracks compatible with the passage of a single muon.

"5" - Multiple tracks, as in "4", were observed but the event also contained tracks as in "2".

"7" - Multiple tracks, as in "4", were observed but the event also contained tracks as in "3".

As an example of the coding, an event which had clear tracks in all arrays except for an electron burst in array A would be recorded as type 3A0. Actual trajectories of type 100 are displayed in plate 2.1.

Plate 2.1.   Photographed muon trajectories.

LARGE ANGLE AIR GAP SPECTROGRAPH

A Trajectory Reconstruction

A Typical Muon Event

CHAPTER   3

THE   OPERATIONAL   CHARACTERISTICS   OF   THE   SPECTROGRAPH

3.1.   Introduction

3.1.1.   Trajectory Description

For a trajectory, as represented in fig. 3.1a, a displacement, $\triangle$, may be defined such that

$$\triangle = (a + a_o) - (b + b_o) - \frac{\ell_1}{\ell_4} \left[(c + c_o) - (d + d_o) \right]. \quad (3.1)$$

In this description a_o, b_o, c_o and d_o are to be interpreted as the distances between the origin of a scale internal to the arrays A, B, C and D and a line parallel to the axis of the spectrograph. The trajectory intersects the array internal scales at the positions a, b, c and d. Gathering together the constant terms, equ. (3.1) may be rewritten in the following manner:

$$\triangle = \left[(a - b) - \frac{\ell_1}{\ell_4} (c - d) \right] + \triangle_o \quad (3.2)$$

where,

$$\triangle_o = \left[(a_o - b_o) - \frac{\ell_1}{\ell_4} (c_o - d_o) \right]$$

From a consideration of equ. (2.4) the momentum of the particle follows immediately and, providing $\triangle$ is small as compared with ℓ_1, can be expressed as follows

$$P = 300.(\ell_1 / \triangle) . \int d.bl. \quad eV/c . \quad (3.3)$$

However, as a , b, c and d can only be determined with a limited precision and also, as particle interaction with the spectrograph elements causes scattering of the trajectory, a momentum as derived using equ. (3.3)

a) The Displacement △
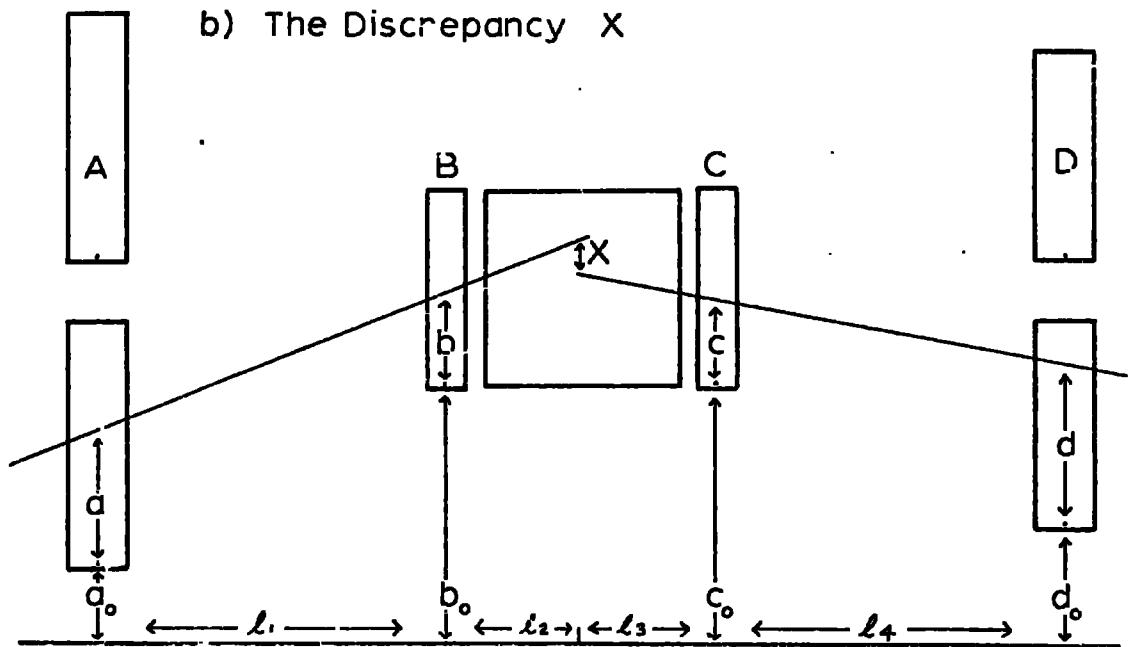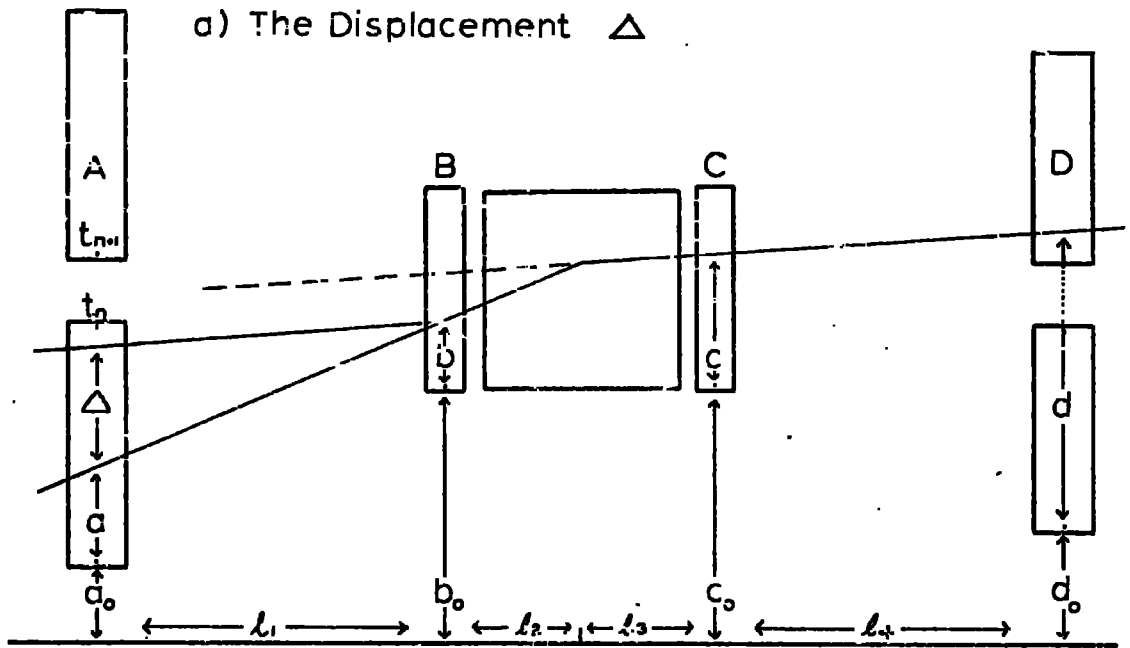
b) The Discrepancy X

will involve some error. An estimation of the deviation from the case of an ideal trajectory may be obtained through examination of the value X, as defined in fig. 3.1b. X is known as the discrepancy and is expected to be near zero for an ideal trajectory.

$$X = (1 + \frac{\ell_2}{\ell_1}) \cdot b - \frac{\ell_2}{\ell_1} \cdot a - (\frac{\ell_3}{\ell_4} + 1) \cdot c + \frac{\ell_3}{\ell_4} d + X_o \quad (3.4)$$

where,

$$X_o = (1 + \frac{\ell_2}{\ell_1}) \cdot b_o - \frac{\ell_2}{\ell_1} \cdot a_o - (\frac{\ell_3}{\ell_4} + 1) \cdot c_o + \frac{\ell_3}{\ell_4} \cdot d_o.$$

A description of the method employed in evaluating these spectrograph constants for the case of the present spectrograph follows in sect. 3.2.

3.1.2 Geometrical Considerations

It is the relative positions and the dimensions of the detecting elements of the spectrograph which determine the rate at which particles are detected and their effective angular range. As can be seen from fig. 2.1, particles incident with zenith angles between 65° and 90°, with an azimuthal range of some 24° about the axis of the spectrograph, could be accepted. For a detailed description of the spectrograph acceptance it is convenient to define an acceptance function $\Phi(\theta, \zeta, E)$. The acceptance function represents the fraction of those particles passing through one of the detecting elements with zenith angles between θ and $\theta + d\theta$, azimuthal angles between ζ and $\zeta + d\zeta$ and energies between E and E + dE which are accepted by the spectrograph. Since particle deflection is confined to the horizontal plane in the present case, two further terms may be defined, such that

$$Z(\theta) \cdot A(\zeta, E) = \Phi(\theta, \zeta, E) \quad (3.5)$$
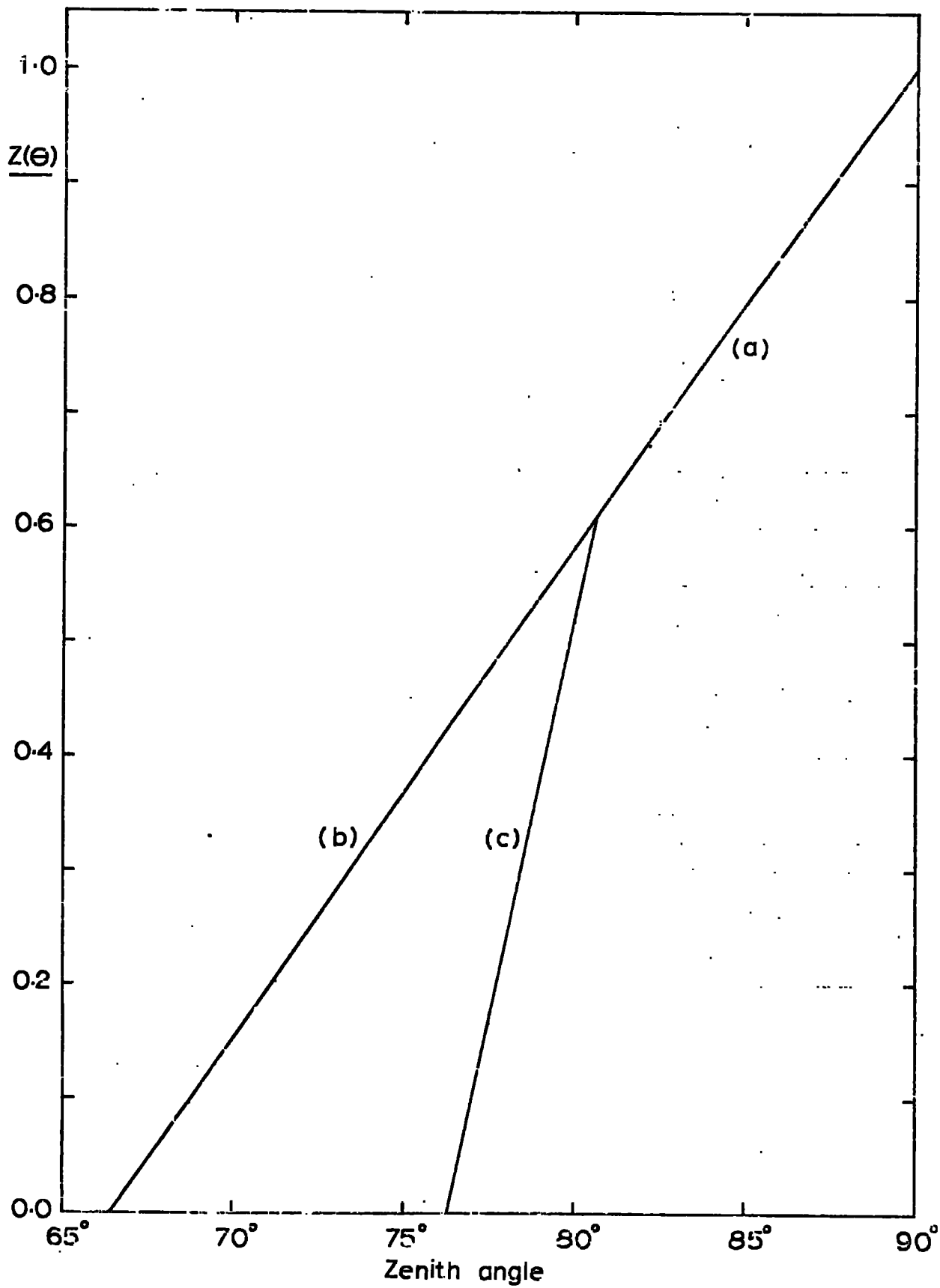
where, $Z(\theta)$ represents a zenith acceptance function and $A(\phi, E)$ represents an energy dependent azimuthal acceptance function.

The zenith acceptance is directly accessible through simple geometrical considerations and the function, evaluated as for the scintillator arrangement S1, S2, S3, $\overline{\overline{S5}}$, $\overline{\overline{S6}}$, $\overline{A}$ and $\overline{D}$, is represented by curves (a) and (b) in fig. 3.2. The zenith acceptance of the spectrograph was greatest for the largest zenith angle, 90°, but due to the rapidly falling spectrum with increasing zenith angle, it was necessary to introduce a further scintillation counter, $\overline{\overline{S4}}$, in order to maintain some balance in the data gathered over the whole range of zenith angles between 65° and 90°. The anticoincidence scintillation counter was introduced for phase 2 of the operation and was positioned so as to reduce the effective height of the scintillator S3. The zenith acceptance function, operative during phase 2 of the experiment, was as represented by curves (a) and (c) in fig. 3.2. The overall running times for each arrangement were as follows:

Phase 1 - $1.078.10^{6}$s

Phase 2 - $1.758.10^{6}$s.

The azimuthal acceptance function is a little more complicated due to it's energy dependence and also due to the gaps at the centres of arrays A and D. As each part of these arrays were independently positioned it is convenient to think of the spectrograph as comprising four geometries represented by trajectory types 1, 2, 3 and 4 in fig. 3.3. Clearly, by a consideration of equs. (3.2) and (3.4), there are required experimental constants X_{o_1}, ...X_{o_4} and Δ_{o_1}, ...Δ_{o_4} for complete trajectory descriptions. Although the azimuthal acceptance function was

SPECTROGRAPH GEOMETRIES   Fig. 3.3
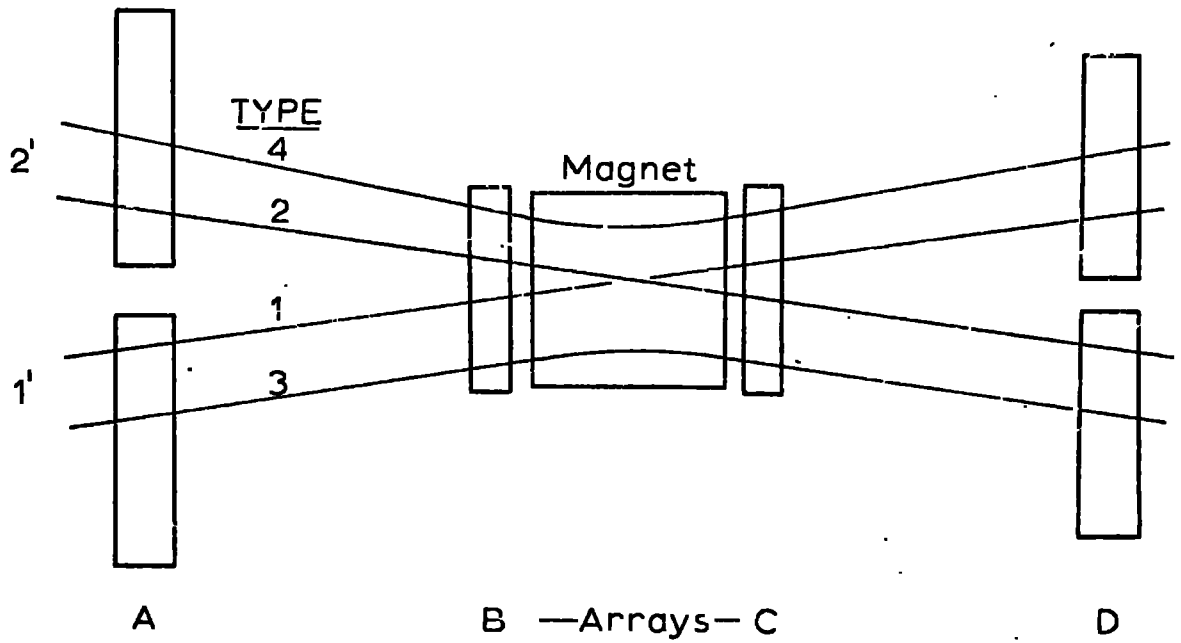
calculated for each geometry seperately, it was noted that for particles
with momenta above a few GeV/c geometries land 2 were dominant, therefore,
in the final analysis of the data, particles were considered to fall into
two main categories. The first category contained particles detected in
geometries 1 and 3, and the second contained particles detected in geo-
metries 2 and 4.

The method adopted in evaluating the azimuthal acceptance function
was to fire particles through the spectrograph in a computer simulation.
Particle trajectories were constructed being deflected in a magnetic
volume having characteristics as described in sect. 2.1. For a
particular energy and azimuthal arrival direction these particle traj-
ectories were made to cross an area, representing the detector S1,
with a uniform line density of 16 particles per centimetre. The fraction
of those trajectories which successfully intersected all the detection
elements of the spectrograph was taken as the azimuthal acceptance
function. The acceptance functions, for particles having momenta 3.2
and 102.4 Gev/c, are plotted in figs. 3.5 and 3.6 as a function of the
azimuthal angle as measured relative to the spectrograph axis. The
contributions from category 1 and 2 trajectories are denoted by $I = 1'$
and $I = 2'$ respectively. The contributions from geometries 3 and 4 to the
acceptance function appear as the small humps at small azimuthal angles.
For momenta above 1 Gev/c, the total acceptance over all azimuthal angles
was found to vary by less than 0.5%.

The corrections to be applied to the experimental data, due to the
effect that the earth's magnetic field has on the muon flux, depend upon
the arrival directions of the muons both in the zenith and azimuthal
planes. The implications of the angular variations in the azimuthal
acceptance function in this respect are discussed in chapter 5.
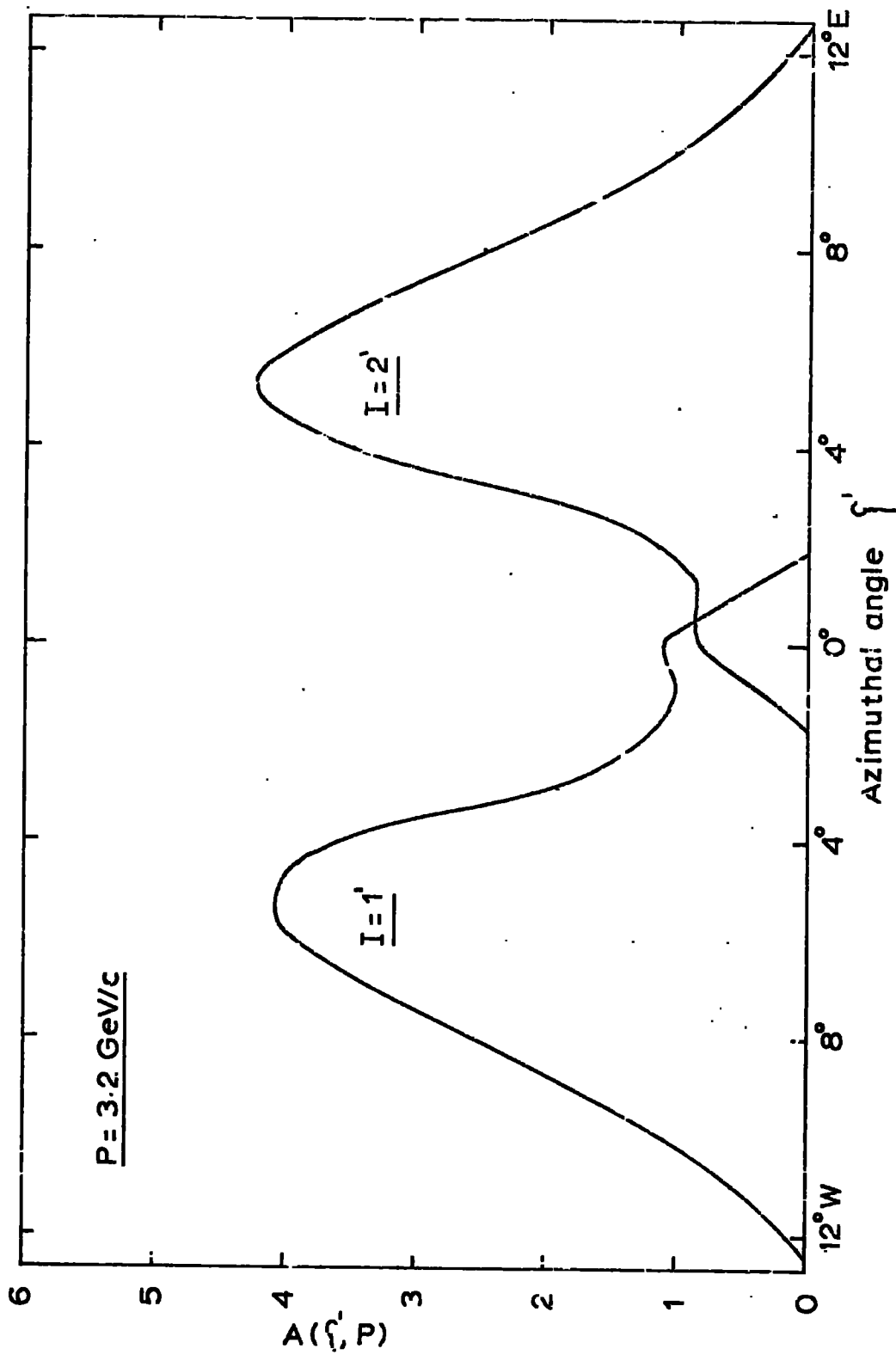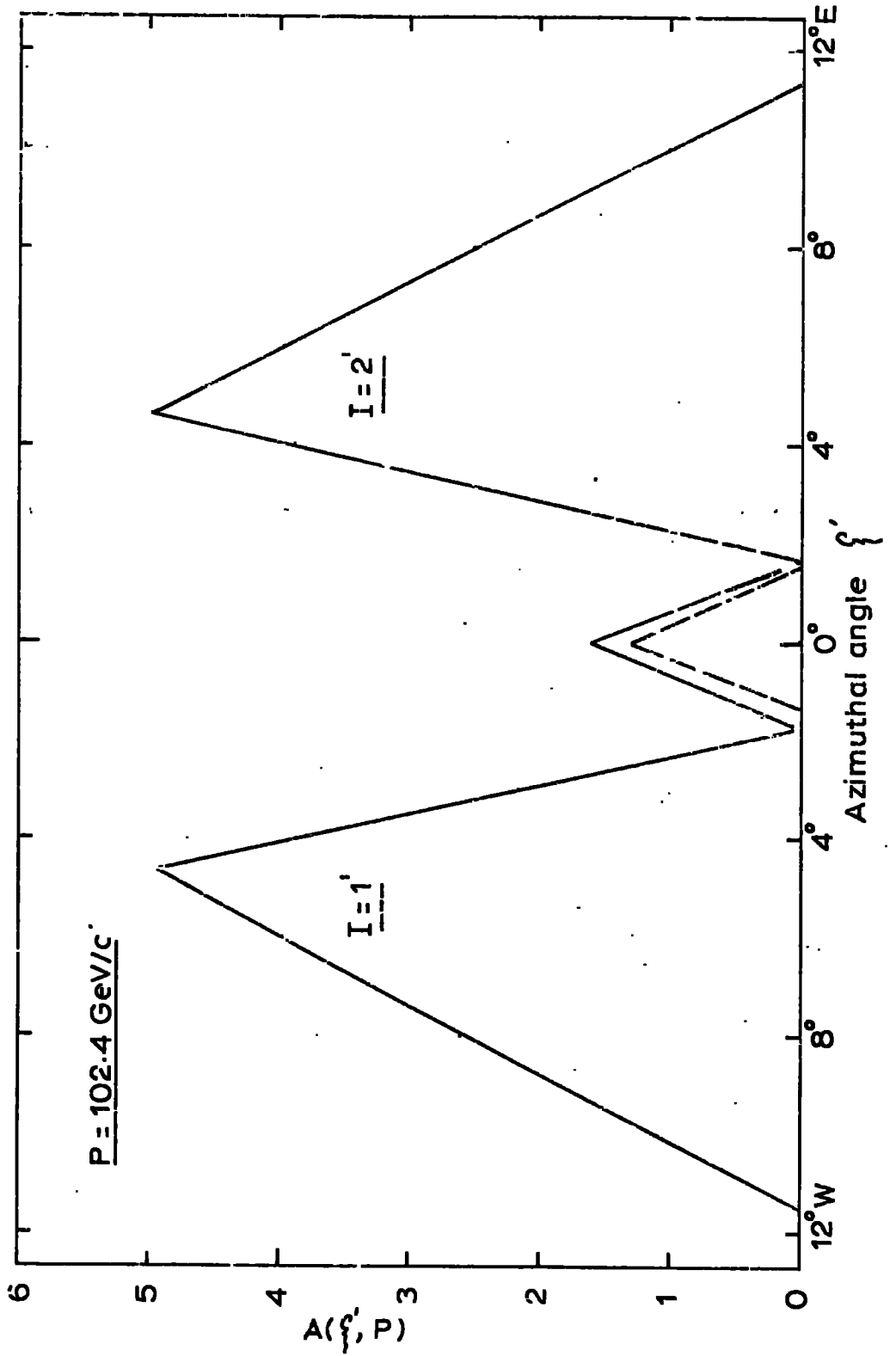
3.2. The Spectrograph Alignment

The flash tube arrays were secured , each by four adjustable bolts, to fixed mounts. By adjustment of the bolts it was possible to set the tubes vertical to within 0.01cm along their lengths. The effect of natural bowing in the tubes on track location was minimized by loading the tubes into the arrays with the direction of the bow set parallel to the axis of the spectrograph. Deviations from parallelism between the arrays were allowed for in the computations of particle momenta by using position dependent values for the tray separations.

Only the relative values of the array separations appear in equ. (3.2) and (3.4). Initial values of these relative separations were obtained by suspending plumbs from a steel rule stretched above the spectrograph locating the measuring levels in each array. An independent method of measurement employed, was to drop plumbs from the measuring levels themselves to the floor, the position there being marked per-manently. After the dismantling of the spectrograph, the floor marks were accessible, so making possible a second survey of the array separations. The resultant values for the separations, after combining the two sets of measurements, are listed in table 3.1. Also as a result of the second survey, approximate values for the array constants a_o, b_o, c_o and d_o were obtained and these are listed in table 3.1. The results from a similar series of measurements on the separations of the scintillation counters are listed in table 3.2.

As has been shown in sect. 3.1.1, for a full trajectory description, spectrograph constants of the type Δ_o and X_o were required. It would have been possible to determine their values through direct measurements

TABLE 3.1.

ARRAY CONSTANTS

Seperation	Working values*(cm)	Mid values (cm)
ℓ_1	$296.49 + 6.763 \ 10^{-3}.a$	296.83
ℓ_2	67.26	67.26
ℓ_3	$56.30 - 4.195 \ 10^{-3}.c$	56.20
ℓ_4	$288.87 + 4.195 \ 10^{-3}.c$	289.00
		(error $\pm$ 0.04 cm)

Constants	Approximate values (cm)	
	(Category 1)	(Category 2)
a_o	0.0	19.9
b_o	66.5	66.5
c_o	66.6	66.6
d_o	42.4	24.4
		(error $\pm$ 0.1 cm)

*Track positions a and c are in tube spacings, c.f. table 2.2b.

TABLE 3.2.

THE POSITIONS OF THE DETECTING ELEMENTS

Counter	Relative heights (cm)		Distance to magnet-centre (cm)
	(Top)	(Bottom)	
S1	91.49	53.9	-34.1
S2	91.62	54.01	52.9
S3	91.93	-41.07	-235.0
S4	19.56	-55.44	-243.0
	(error ~ ±0.01 cm)		(error ~± 0.1cm)

on the relative position of the arrays but due to direct measurements
being difficult, in this case a consequence of the varying heights of
the array measuring levels and also some uncertainty in locating the
real position of the array scale origins, indeterminable errors would
have resulted. The values for the spectrograph constants were obtained
by an analysis of real muon trajectories. This was possible for the
present spectrograph since the contribution to the deflection from
instrumental scattering was small; the r.m.s. deflection through scattering
amounted to only 8% of the total deflection.

Initial values for X_{o_1} ,.....X_{o_4} were estimated using particles of all
momenta for magnetic fields in both directions. Using the criterion that
X_{o_n} be less than 1.0cm, 1,500 trajectories of type 100 and 200 (c.f. sect.
2.7 for description) observed in runs with the magnet switched off, were
examined initially setting Δ_{o_n} equal to zero. The distributions in Δ
so obtained, are presented in fig. 3.7 and fig. 3.8, these being the
distributions for type 1 and type 2 trajectories. The tail in the
distributions show the effect of the large angle scattering associated
with the lower energy particles in the sample. The values of Δ_{o_1} and
Δ_{o_2}, corresponding to the most probable values of the distributions in
Δ so defined, were computed by iteration, selecting only muons which had
displacements within 2.1cm of the previously calculated means. 90% of
the initially selected particles were used in the computations of the
stationary means. As these mean values were sensitive to the displacement
suffered through large angle coulomb scattering, the finally accepted
values of Δ_{o_1} and Δ_{o_2} were obtained by a combination of these means
with the medians of the distributions, weighting each according to

Zero field — Geometry 1 Fig.3.7

X < 1.0 cm

Zero field — Geometry 2   Fig. 3.8

X < 1.0 cm

Distributions in X with $X_0 = 0$ — Geometry 1   Fig. 3.9

+ve field

p>10 GeV/c

−ve field

p>10 GeV/c

Distributions in X with $X_o = 0$ — Geometry 2   Fig. 3.10
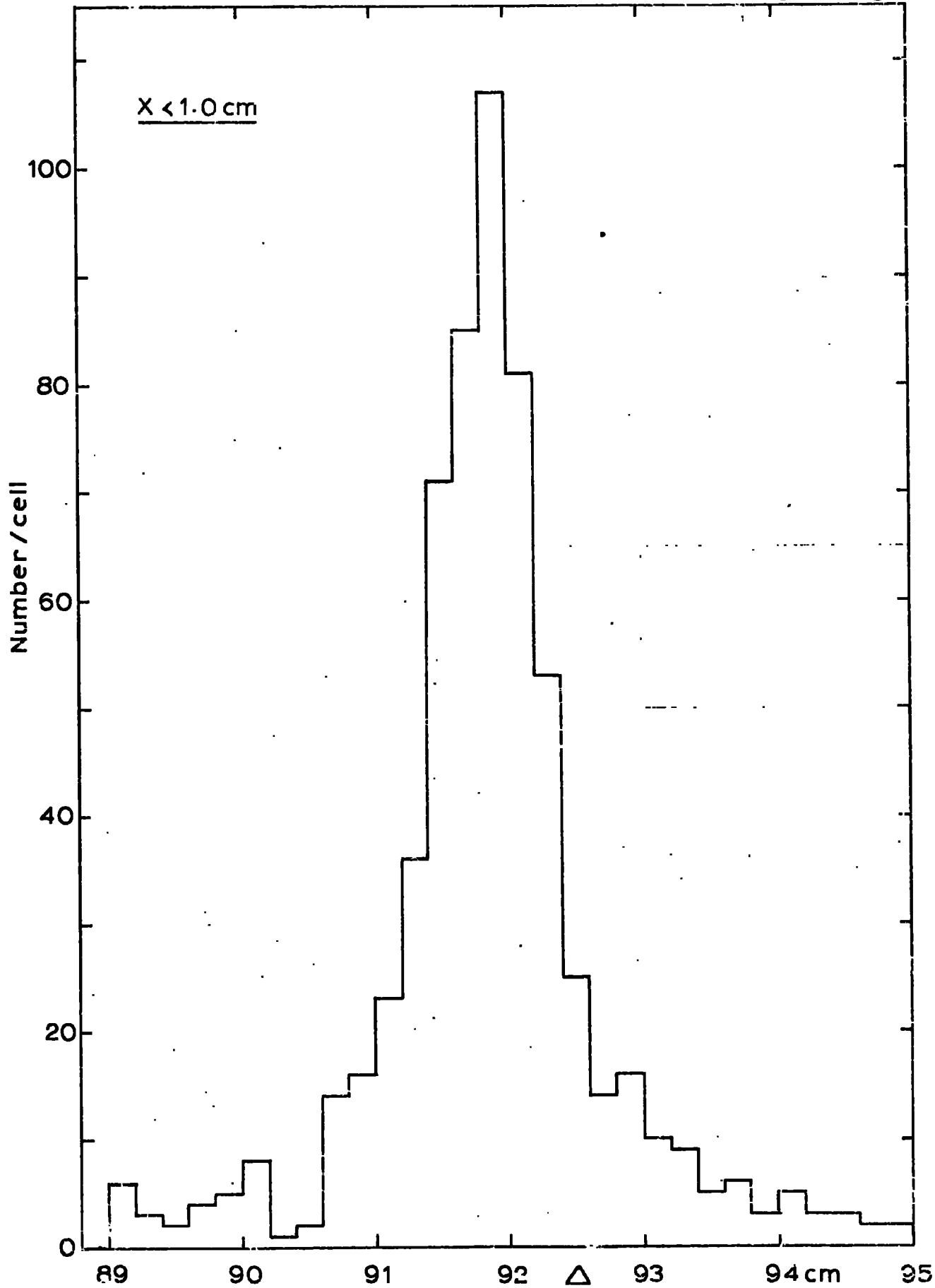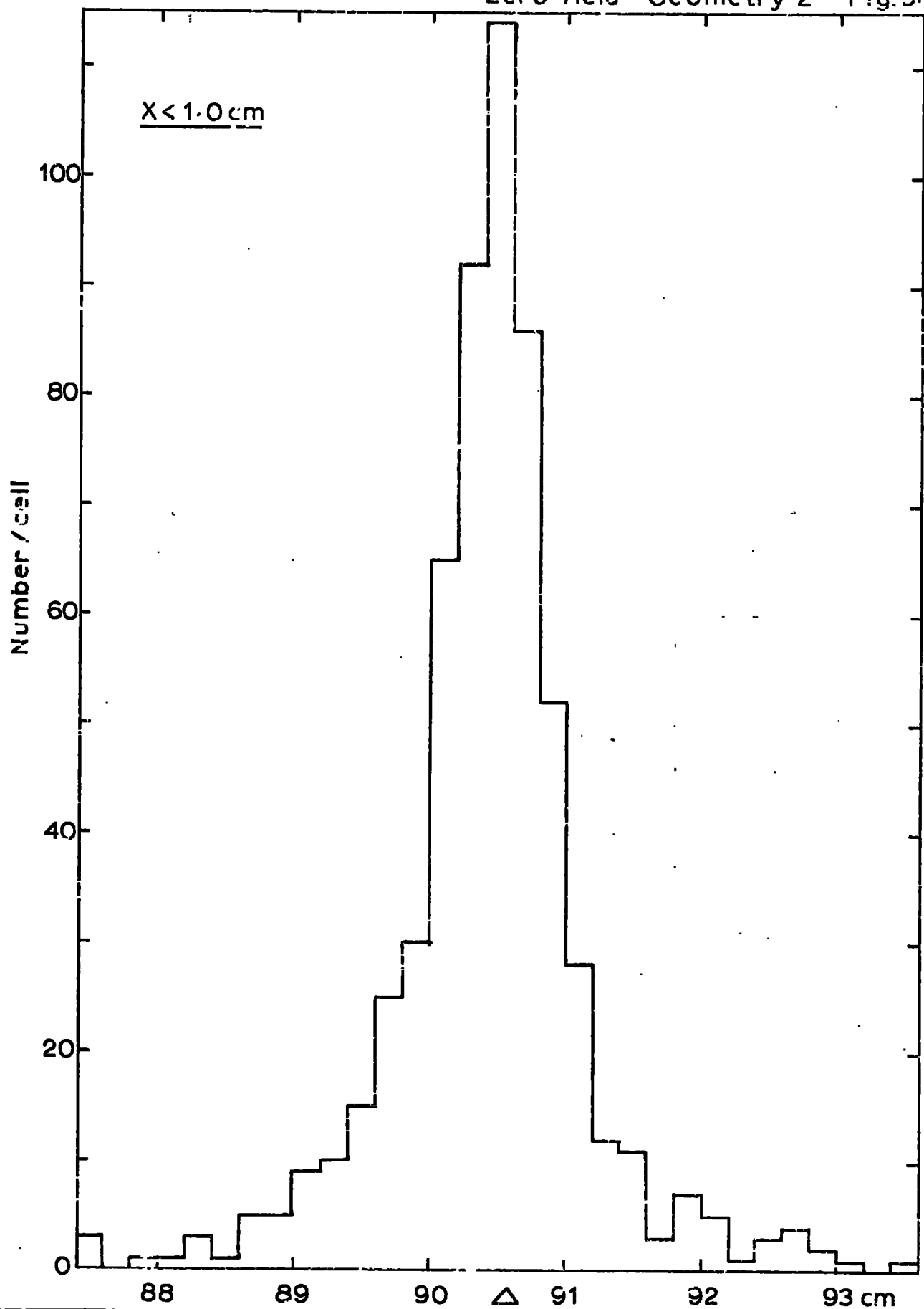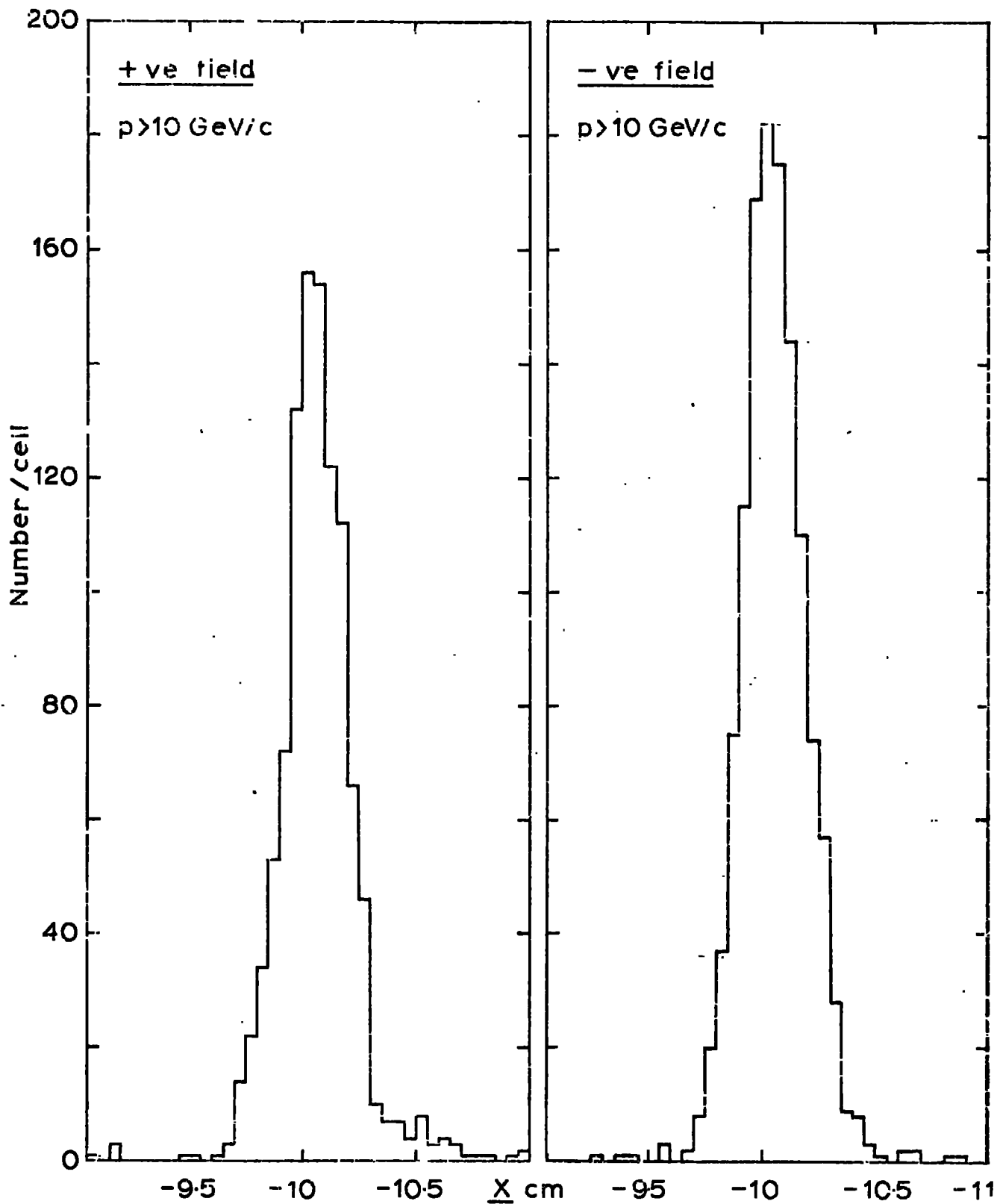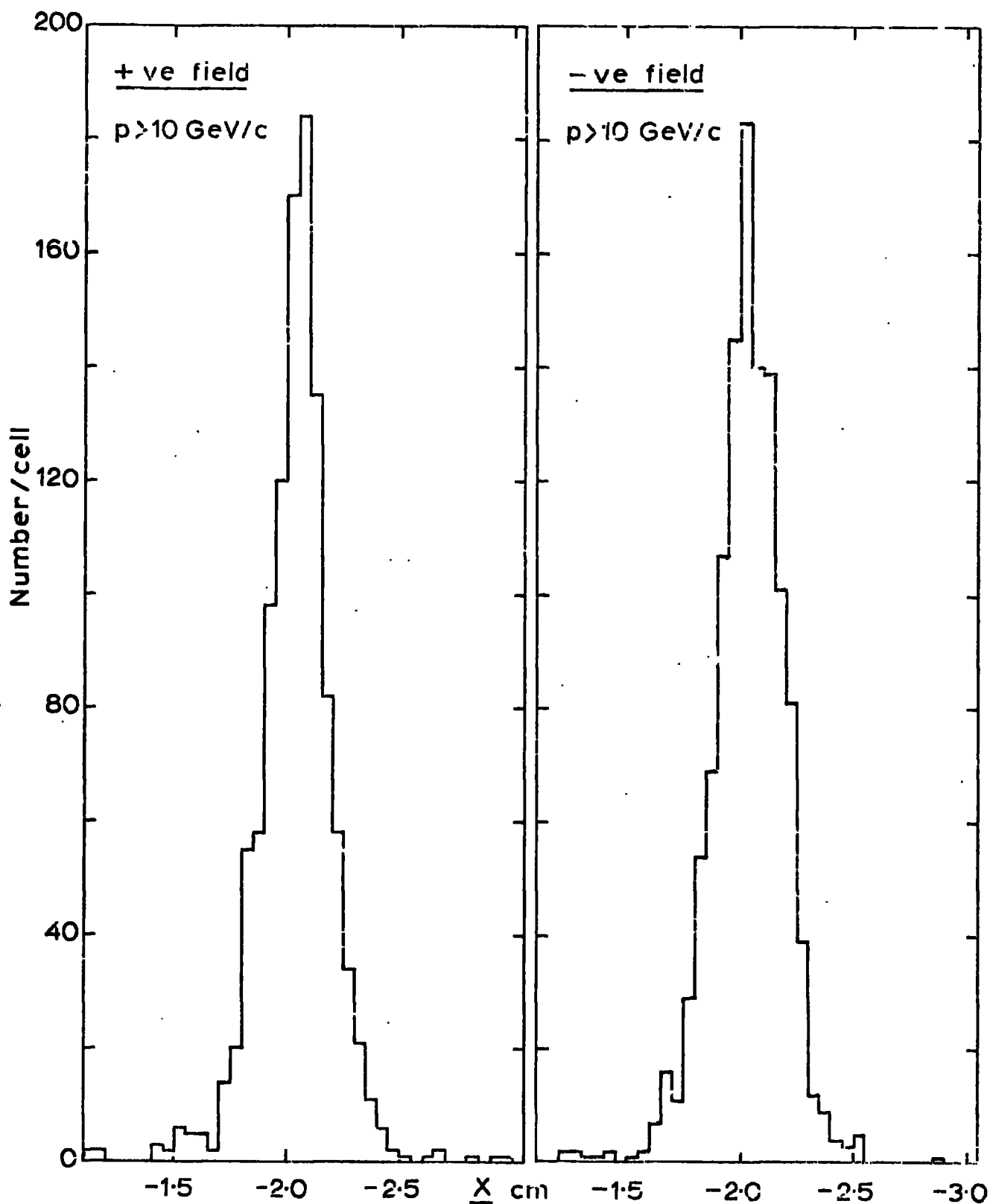
TABLE 3.3.

DISTRIBUTION CHARACTERISTICS

Zero Field ($-\Delta_o$)				
Geometry	Mean (cm)	Sample	Median (cm)	Sample
I = 1	91.891 ± .026	594	91.864 ± .033	590
I = 2	90.470 ± .026	590	90.457 ± .033	579
I = 3	110.52 ± .083	48	110.458 ± .104	51
I = 4	72.114 ± .097	54	71.936 ± .122	63

Negative Field ($-X_o$)				
Geometry	Mean (cm)	Sample	Median (cm)	Sample
I = 1	-10.053 ± .004	1238	-10.060 ± .005	1227
I = 2	- 2.036 ± .005	1166	- 2.039 ± .006	1161
I = 3	- 6.564 ± .019	101		
I = 4	- 5.535 ± .012	128		

Positive Field ($-X_o$)				
Geometry	Mean (cm)	Sample	Median (cm)	Sample
I = 1	-10.060 ± .005	1005	-10.064 ± .006	1032
I = 2	- 2.038 ± .005	1057	- 2.046 ± .006	1110
I = 3	- 6.524 ± .019	72		
I = 4	- 5.528 ± .017	107		

their respective errors. This procedure was justified by a consideration of the expected symmetry in the distributions in the displacements about Δ_{o_n}. The values for Δ_{o_3} and Δ_{o_4}, computed in this way, had large uncertainties associated with them as the number of muons accepted in geometries 3 and 4 were only 56 and 66 respectively. Using these values for Δ_{o_n}, it was possible to impose a restriction such that only muons with momenta >10 Gev/c were used in the computations of the final values for X_{o_n}. The distributions for X_{o_n}, for both positive and negative field directions, are shown in figs. 3.9 and 3.10.

Through the definitions of X_o and Δ_o, as in sect. 3.1.1, it can be seen that the pairs of values X_{o_1}, X_{o_3}, and Δ_{o_1}, Δ_{o_3} can be related through the value chosen for a_o, similarly X_{o_2}, X_{o_4}, and Δ_{o_2}, Δ_{o_4} are related through a change in the value d_o. Using the values of Δ_{o_1}, Δ_{o_2} and X_{o_1}, X_{o_2}, as already calculated, values for the required change in d_o and a_o were computed and hence accurate values for Δ_{o_3} and Δ_{o_4} followed. In table 3.3 the distribution characteristics and statistics are listed. The working values of the constants Δ_{o_n} and X_{o_n} are presented in table 3.4.

<p align="center">TABLE 3.4.</p>

	Δ_o (cm)	X_o (cm)
I = 1	−91.880 ± .029	10.057 ± .004
I = 2	−90.465 ± .029	2.038 ± .003
I = 3	−110.352 ± .038	6.549 ± .007
I = 4	−71.993 ± .038	5.546 ± .007

Arrays E and F, the zenith measuring arrays, were accessible to a
direct survey. The separation, 88.75 ± 0.02 cm, was measured using a
steel rule while the relative heights of the array scale origins for
E and F, measured using a cathetometer, were found to be 94.75 ± 0.01
and 95.30 ± 0.01 cm respectively. The resolution for this system in
measurements on the projected zenith angles was better than 0.25^o.
Cathetometer measurements of the vertical positions of the scintillation
counters, positioned within the geometry of the flash tube arrays, were
also possible; the results of these measurements are listed in table
3.2.

3.3. Instrumental Noise

3.3.1. The Maximum Detectable Momentum

Defining the maximum detectable momentum (m.d.m.) as being the
momentum corresponding to a displacement equal in magnitude to the
probable error in the measurement of such a displacement, then an estimate
of its values is derivable from an examination of the central portion
of the distribution in X.

For the present instrument, the relationship between the standard
deviation in the X distribution, x, and the standard deviation in the
associated displacements, d, was

$$d^2 = x^2 \left[23.1 . (1 + k^2)/(32.9 + k^2) \right] \tag{3.6}$$

where k is the ratio of the overall track location error in the arrays
A and D to that in the small tube arrays B and C. k was estimated to
be 1.41 ± 0.20 for the spectrograph; the main source of error in the
evaluation of k arose from the uncertainty in the absolute resolution
in each flash tube array. The above relationship was derived assuming

that the contribution to the spread in the X distribution from Coulomb scattering was negligible which was justified in this case as only the central portion in the X distribution was used in evaluating **x**.

An examination of the distribution in X returned a value of x = 0.125 ± 0.006 cm and since the product of the momentum and displacement for the spectrograph was 23.23 GeV/c.cm the resultant m.d.m. was 196 ± 15 GeV/c.

3.3.2 The Effect of Noise on the Muon Measurements

Due to the rapidly falling muon energy spectrum the effect of instrumental noise in spectrograph measurements will tend to cause an overestimate in the number of high energy muons incident at sea level. Of particular importance, as far as the measurements on the muon charge ratio are concerned, is the possibility that the error in the determination of the deflection might be such as to cause a wrong charge assignment. This wrong charge assignment has the effect of masking any charge excess in the incident muon beam and becomes significant when measurements are made near to and beyond the m.d.m. of the instrument.

Following MacKeown (1965), the relationship between the observed charge ratio, R_o, and the incident charge ratio, R_i, for muons incident with energies up to a few hundred GeV, is well represented by

$$R_i = \frac{(R_o + 1).\text{erf} (\triangle/d \sqrt{2}) + (R_o - 1)}{(R_o + 1).\text{erf} (\triangle/d \sqrt{2}) - (R_o - 1)} \qquad (3.7)$$

providing that the charge ratio varies only slowly with energy.

For various values of the incident charge ratio, the corresponding observed charge ratios, calculated using equ. (3.7), have been plotted as a function of $\triangle/d$ in fig. 3.11. The dashed curve, A, shows the

Fig. 3.11
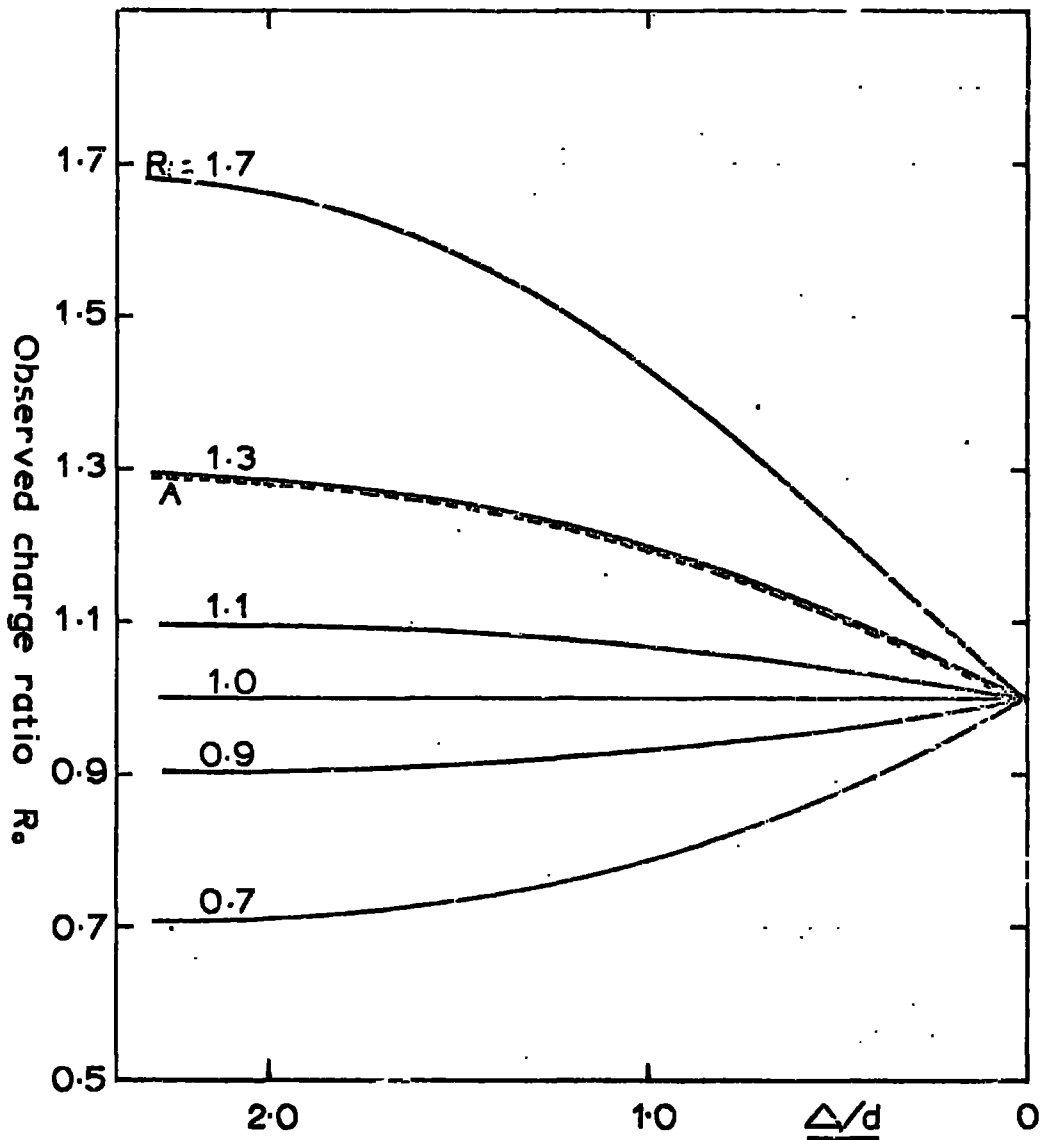
The observed ratio for various incident ratios
plotted vs. the displacement expressed in terms
of the standard deviation. For A, d is assumed
to have 30% contribution from Coulomb scattering.

effect of instrumental scattering, here the r.m.s. displacement through scattering is taken to be 0.3Δ.

CHAPTER   4

THE EXPERIMENTAL DATA

4.1. Event Selection

Events were recorded with frequencies 59.1 and 26.6 per second
for Phase 1 and Phase 2 of the spectrograph's operation; the general
paralysis of the spectrograph after each trigger was of duration
6.911 seconds. Of some 30,000 events scanned, the number accepted for
further computer analysis was 16,528. During the analysis by computer,
events further rejected fell into four main catagories comprising the
following:

1) type 3 and 7 events where the affected tracks were in the
   zenith measuring arrays E and F (lack of precision in the
   zenith measurement);

2) type 4 and 5 events where the multiple tracks occurred in
   arrays E and F (ambiguity in zenith angle assignment);

3) events where the central discrepancy X was found to be
   greater than 1.0 cm (this restriction being imposed to
   guard against those events containing tracks of unassociated
   particles or mistakes made during film scanning - this
   restriction is biassed against low momentum events, due to
   the consequences of Coulomb scattering in the elements of
   the spectrograph, but positive and negative muons will
   suffer similar rejection so unaffecting the overall
   measurement of the charge ratio);

TABLE 4.1a

Muon Data - Geometries 1 and 3

Zenith (Degrees)	charge	Cell boundaries (GeV)							
		0.2	4.0	10.0	15.9	25.1	39.8	63.1	158.5
65.0-67.5	+	33	20	17	7	4	1	0	3
	−	38	27	12	4	3	1	2	1
67.5-70.0	+	91	89	37	32	15	13	4	3
	−	85	61	36	21	10	6	3	4
70.0-72.5	+	115	106	42	35	28	11	13	3
	−	103	93	36	34	21	13	8	6
72.5-75.0	+	104	106	53	41	29	21	12	12
	−	97	93	52	31	20	22	17	3
75.0-77.5	+	93	145	78	76	47	33	34	15
	−	106	127	68	54	45	17	23	12
77.5-80.0	+	110	186	109	98	82	46	64	27
	−	137	140	110	88	69	42	48	26
80.0-82.5	+	68	102	82	92	80	68	45	35
	−	88	118	76	75	65	57	44	36
82.5-85.0	+	38	56	35	51	61	73	71	46
	−	56	60	44	54	37	41	37	23
85.0-87.5	+	11	22	11	26	46	34	40	23
	−	19	28	12	35	32	25	27	30
87.5-90.0	+	3	4	5	7	9	16	10	8
	−	7	9	6	6	4	8	12	8

TABLE 4.1b

Muon Data - Geometries 2 and 4

Zenith (degrees)	charge	Cell boundaries (GeV) 0.2	4.0	10.0	15.9	25.1	39.8	63.1	158.5
65.0-67.5	+	33	24	17	8	3	3	2	1
	-	31	21	4	8	3	2	1	0
67.5-70.0	+	76	76	42	37	14	5	9	2
	-	85	73	33	30	15	11	7	2
70.0-72.5	+	105	124	50	34	22	12	11	4
	-	102	92	33	31	27	12	7	7
72.5-75.0	+	93	102	72	30	28	22	16	9
	-	98	84	51	35	25	10	13	10
75.0-77.5	+	91	125	78	67	46	24	24	15
	-	111	130	59	68	47	17	20	9
77.5-80.0	+	104	145	95	99	91	57	41	20
	-	127	176	102	93	69	48	46	35
80.0-82.5	+	63	126	93	97	93	69	51	34
	-	123	138	89	81	65	44	46	21
82.5-85.0	+	16	47	50	70	80	46	53	23
	-	72	92	47	49	35	35	44	30
85.0-87.5	+	8	15	22	33	27	43	40	21
	-	25	26	20	25	37	25	36	17
87.5-90.0	+	9	1	5	3	6	8	12	4
	-	8	10	8	8	8	9	13	14

4) those muons being observed passing through the edges of the

arrays A and D (incomplete track definition causing a loss

of precision).

The number of particles falling into categories (1) and (2), (3), and

(4) were 376, 1,441 and 695 respectively.

The computer presented the accepted events, totalling 14,016,

in histograms, the muons being grouped according to their arrival

zenith angles, energies and trajectory type. The data comprising the

histograms, for spectrograph geometries 1' and 2', are presented in

tables 4.1a and 4.1b.

4.2. The Observed Charge Ratio

For the purposes of presenting the raw data in charge ratio form,

the results from both acceptance geometries were combined. The combined

data, having been grouped into zenith cells 65°-75° and 75°-90°, are

presented in charge ratio form in fig. 4.1. The errors on the ratios

were calculated in accordance with the relationship of equ. (B1.2).

In fig. 4.1, the effect of the earth's magnetic field, which is

expected to be most severe for muons arriving with the largest zenith

angles, is clearly indicated. An evaluation of the geomagnetic effect

follows in chapter 5. In chapter 6, the experimental results are

presented corrected for the instrumental effect and normalized to

values expected for measurements on the muon charge ratio arriving

along the magnetic meridian.
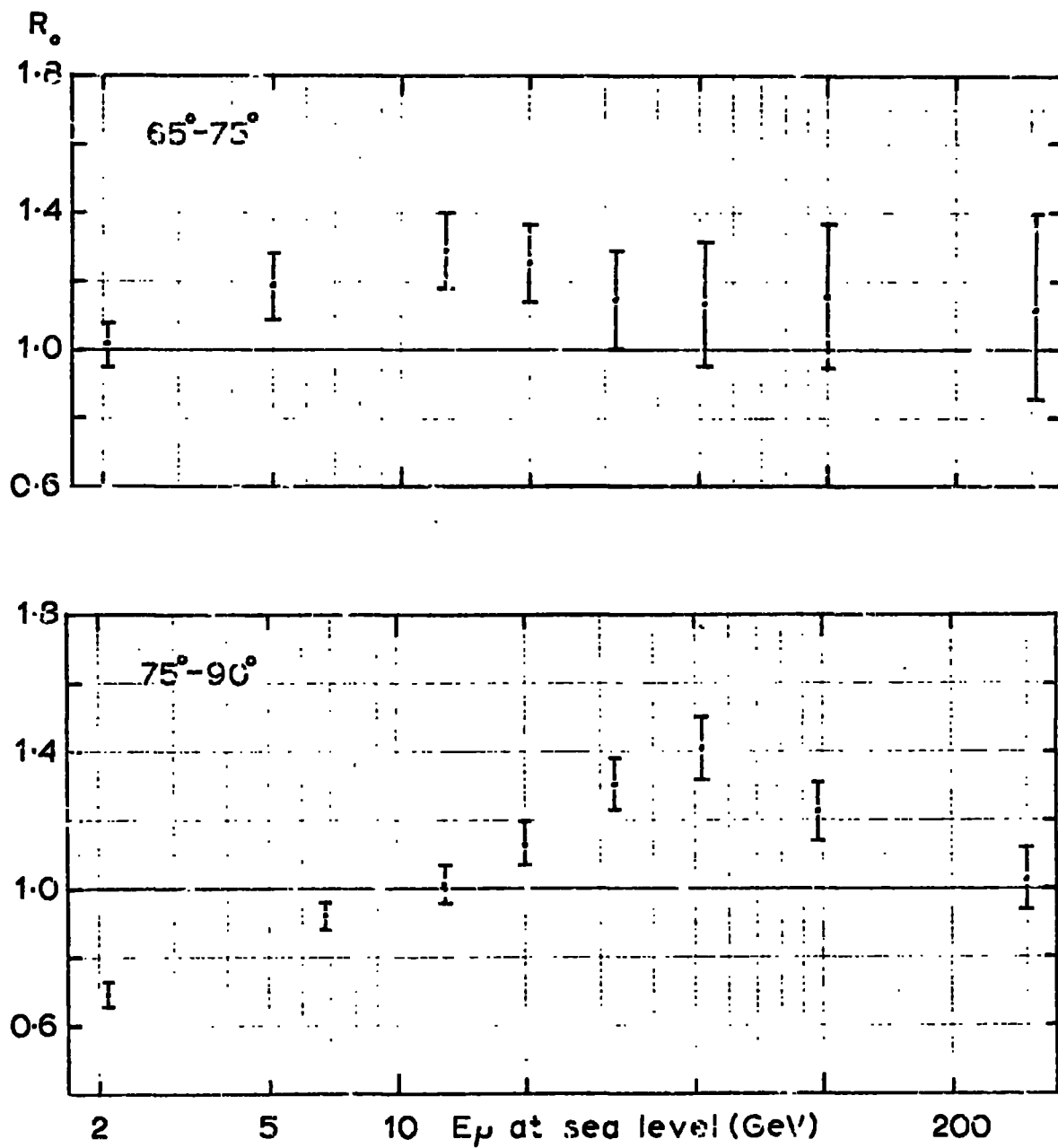
CHAPTER 5

THE GEOMAGNETIC CORRECTION FACTOR

5.1. Introduction

The present chapter is devoted to the development of the work of

Osborne (1966) and Maeda (1960,1964) on the sea level spectra of muons

to include the propagation of muons under the influence of the earth's

magnetic field. Although the total intensity of muons is only slightly

modified by the geomagnetic effect, the modulation on the charge ratio

itself can be severe. In order to compare the present observed charge

ratio results with those of other experiments a normalization to con-

ditions of minimum geomagnetic effect (propagation along the magnetic

meridian), through a geomagnetic correction factor, was necessary.

Geomagnetic correction factors have been computed for the present

experimental orientation and also for that of the previous Durham

horizontal spectrographs.

5.2. Notations and Definitions

For the purposes of a description of muon propagation in the

atmosphere, it is convenient to define a number of general propagation

parameters. E_μ, ϕ and Σ represent the energy, zenith angle and

azimuthal angle of the muons at production which correspond to similar

sea level parameters Eo, θ and ζ . The parameters θ, ζ , ϕ and Σ are

measured relative to a co-ordinate system with origin at the earth's

centre and with ordinate passing through the point of observation;

the azimuthal angles are measured relative to the direction of the geo-

magnetic meridian. y, z-(v,w) represent mutually normal vectors with z-(w) normal to the muon trajectory at production - (sea level) and also normal to the local vertical. For the purposes of the inclusion of the curvature of the earth's surface and its atmosphere in the propagation problem, it is convenient to define further parameters θ^*, the local zenith angle, and K, a propagation term (c.f. fig. 5.1), which are related as follows

$$\text{Sin } \theta^* = (K + R) \big/ (H + R) \tag{5.1}$$

where H is the altitude of the particle and R the earth's radius.

Defining x as the vertical depth from the top of the atmosphere, expressed in units of gm cm^{-2}, and assuming the atmosphere to be well described by a model as used by Osborne, the relationship between altitude H, pressure x, and density ρ are as follows:-

a) Below the level of the tropopause

$$x(H) = 1030.(1 - 0.02156.H)^{5.587} \text{ g cm}^{-2} \tag{5.2}$$

$$H(x) = 46.38071 - 13.398.x^{0.179} \text{ km} \tag{5.3}$$

$$\rho(x) = 4.170 \ 10^{-6}.x^{0.821} \text{ g cm}^{-3} \tag{5.4}$$

b) Above the tropopause

$$x(H) = 253.3.\exp(-0.1549 (H-10.3)) \text{ g cm}^{-2} \tag{5.5}$$

$$H(x) = 46.040 - 6.4576.\ln(x) \text{ km} \tag{5.6}$$

$$\rho(x) = 1.548 \ 10^{-6}.x \text{ g cm}^{-3} \tag{5.7}$$

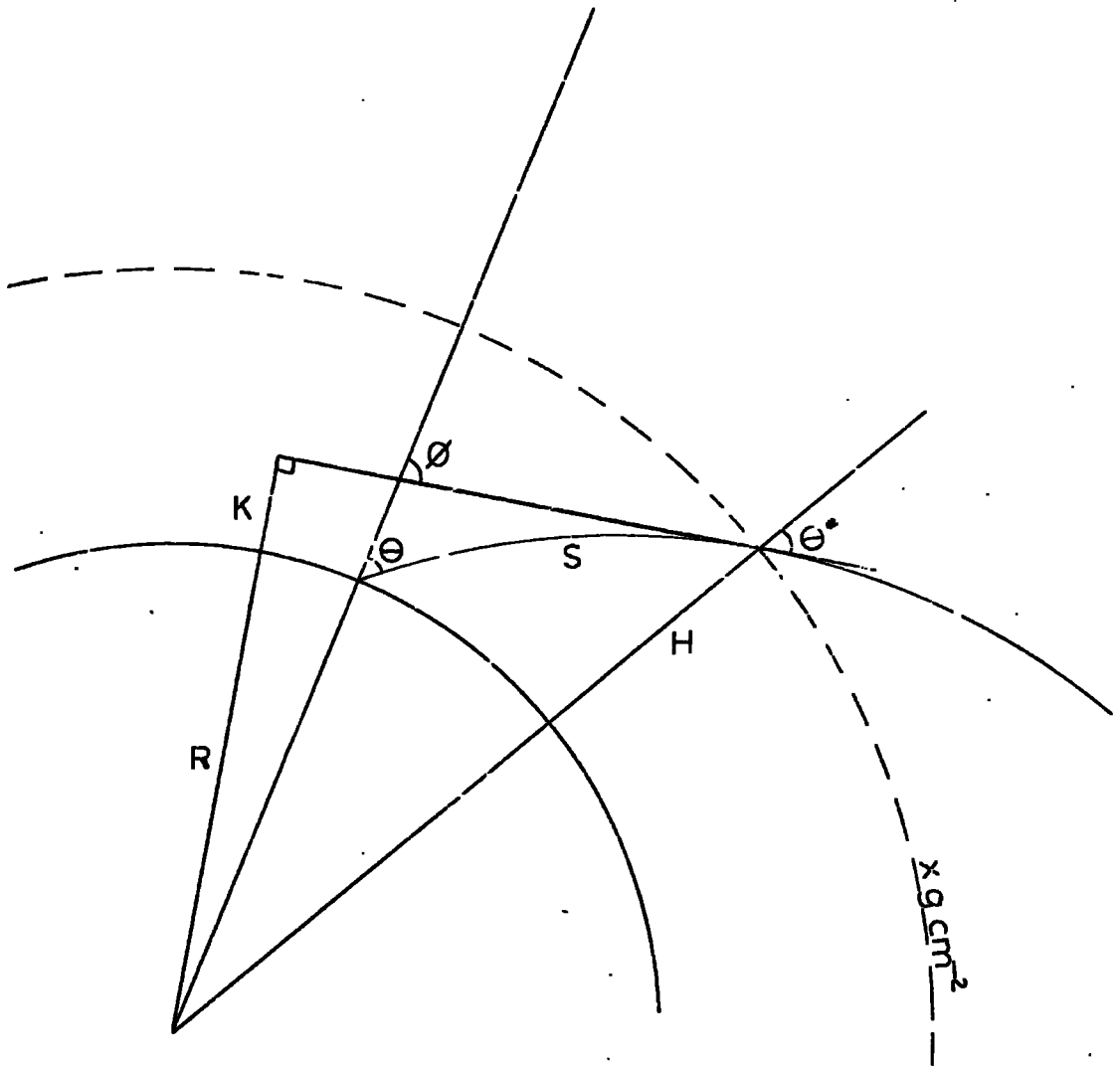The mean height of the tropopause is to be taken as 10.3km (x = 253.3 g cm^{-2}).

Fig. 5.1   Trajectory description

5.3. The Muon Sea Level Spectrum at Large Zenith Angles

5.3.1. Muon Spectrum from a Muon Production Spectrum

In their passage through the atmosphere after production, the muons will lose energy via the processes of ionisation and excitation, pair production in the Coulomb field of the air nuclei, and bremsstrahlung and nuclear interactions. Osborne, reviewing the contributions to the total energy loss through each process, arrived at a functional form for the total energy loss of muons in air which is as follows:-

$$-\left(\frac{dE}{dx}\right) = 2 \cdot 137 \, 10^{-3} + 7 \cdot 66 \, 10^{-5} \left[\ln Em + 2 \ln E + 0 \cdot 25 \left(\frac{Em}{E + 0 \cdot 106}\right)^2 \right] + 2 \cdot 73 \, 10^{-6} E \quad GeVg^{-1}cm^2 \tag{5.8}$$

for $E < (0 \cdot 504)/\sqrt{\rho}$ GeV and

$$-\left(\frac{dE}{dx}\right) = 2 \cdot 109 \, 10^{-3} + 7 \cdot 66 \, 10^{-5} \left[\ln Em + 0 \cdot 25 \left(\frac{Em}{E + 0 \cdot 106}\right)^2 - \ln \rho - \frac{0 \cdot 2538}{E\rho} \right] + 2 \cdot 73 \, 10^{-6} E \quad GeVg^{-1}cm^2 \tag{5.9}$$

for $E > (0 \cdot 504)/\sqrt{\rho}$ GeV

where Em is the maximum transferable energy of a muon to an electron in inelastic collisions, and for air is given by

$$E_m = E^2 / (E + 10.94) \text{ GeV.} \tag{5.10}$$

The energy loss function is plotted as a function of energy in fig. 5.2.

Not all the muons produced will arrive at sea level because of the probability of decay in flight. The lifetime of the muons is $\sim 10^{-8}$ s and the time of flight of muons between production and arrival at sea level is $\sim 10^{-3}$ s for the largest zenith angles. As a direct consequence of the relatavistic time dilation, however, and also due to the energy loss suffered by the muons being greatest over the last part of their trajectories the chances of survival remain appreciable. The survival

Fig. 5·2

x = 120 g cm^{-2}

x = 1030 g cm^{-2}

Muon energy (GeV)

Rate of energy loss — dE$_\mu$/dx (Mev g cm^{-2})
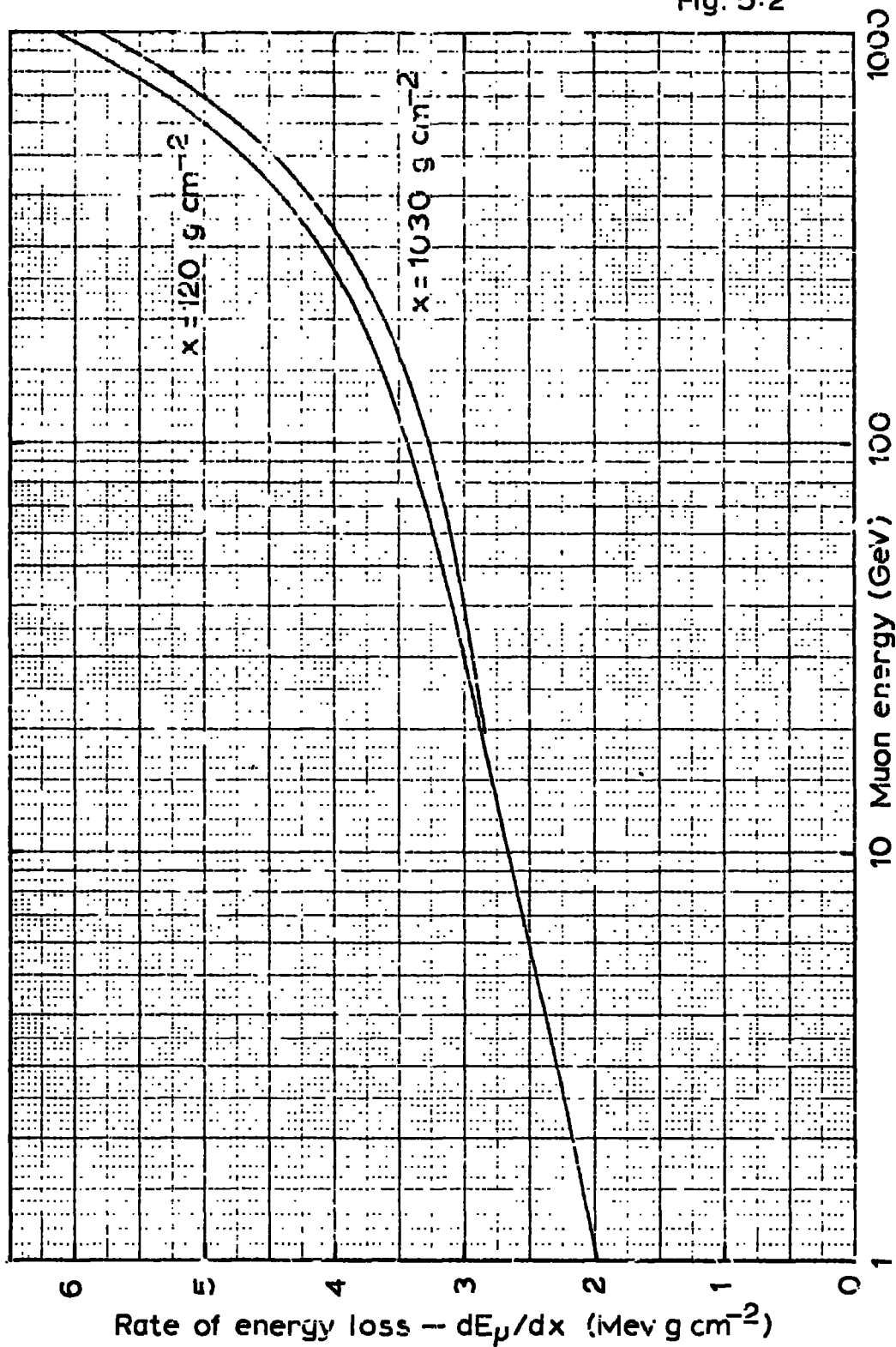
probability, SP, may be defined as follows

$$SP(x, E_o, \theta) = \exp\left[-\frac{m_\mu c^2}{c \tau_\mu} \cdot \int_x^{x_o} \frac{\sec\theta^*}{E(x', E_o, \theta)} \frac{dx'}{\rho(x')}\right] \qquad (5.11)$$

where $m_\mu c^2$ and τ_μ are the rest mass energy and lifetime of the muon respectively.

For some particular depth x in the atmosphere, the corresponding slant depth being $l(x, \ell)$, the number of muons produced by parents travelling with direction parameters ϕ and Σ (the angular spread of muons produced by pions is negligible above a few GeV, Maeda-1960) may be defined as N_μ (E_μ (x, E_o, ϕ, Σ), $l(x, \phi)$.) dl; these muons, if they survive, will arrive at sea level within some cell characterized by an energy E_o, a zenith angle θ and an azimuthal angle ζ. The contribution from muons produced at a depth $l(x, \phi)$ to the sea level intensity in a unit cell of energy, angle and area may be expressed, therefore, as

$$M_\mu(E_o, \theta, \zeta) = N_\mu(E_\mu(x, E_o, \theta, \zeta), \ell(x, \phi)) \cdot SP(E_\mu(x, E_o, \theta, \zeta), \ell(x, \phi))$$
$$\cdot J\left(\frac{E_\mu, \phi, \Sigma, y, z}{E_o, \theta, \zeta, v, w}\right) \cdot dl. \qquad (5.12)$$

J, a cell width correction, represents the Jacobian of E_μ, ϕ, Σ, y, z with respect to E_o, θ, ζ, v, w.

It is here noteworthy that for undeflected trajectories (the approximate case for propagation along the magnetic meridian without scattering) the Jacobian reduces to ($\partial E_\mu / \partial E_o$). For the cell width correction in this case Osborne used $\left[\frac{dE}{dl}(E_\mu, x) \Big/ \frac{dE}{dl}(E_o, x_o)\right]$ which for sea level muon momenta greater than 5 GeV/c does give a reasonable

fit, but in view of the fact that with increasing energy $(\partial E_\mu/\partial E_0)$ converges on unity more rapidly than the value used by Osborne, the error so introduced in evaluating the muon spectrum at 1000 GeV was 3% for the vertical muons and 6% for the large angle muons. As this discrepancy is largely due to the persistance of the density term in the energy loss relationship (equ. 5.9) and considering that the muon energy loss is most important deep in the atmosphere a better approximation would have been to use $\left[\frac{dE}{dt}(E_\mu;x_0)\Big/\frac{dE}{dt}(E_0,x_0)\right]$ as the cell width correction term which is accurate to within 1% for all muon arrival energies above a few GeV.

5.3.2. The Muon Production Spectrum

For pionization as the only process in inelastic collisions of the primaries, Maeda (1964) showed how the accurate integral expression for the pion intensity could be reduced, under given approximations, to the solution of the diffusion equations as used by such previous workers as Barrett et al. (1952), Smith and Duller (1959), Zatsepin and Kuzmin (1961) and Allen and Apostalakis (1961). He extended the calculations to include the production of kaon parents decaying through the $K_{\mu 2}$ mode. Osborne (1966) included all decay modes of both charged and neutral kaons with branching ratios $> 1.0\%$.

The general expression for the number of pions with energy E_π at a depth x, as derived by Maeda (1960), is

$$N_\pi(E_\pi, x, \theta') = \int_0^x \exp\left[-\int_{x'}^x \left(\frac{B_\pi(x'')}{E_\pi \, x''} + \frac{1}{L_\pi}\right) \cdot \frac{dx''}{\cos\theta'(x'')}\right] \cdot \exp\left[-\int_0^{x'} \frac{dx''}{L_n \cos\theta'(x'')}\right] \cdot \frac{F(E_\pi').dx'}{L_c \cos\theta'(x')} \quad (5.13)$$

where L_π is the absorption mean free path of pions,

L_n is the absorption mean free path of nucleons,

L_c is the collision mean free path of cosmic ray primaries,

$F(E_\pi^r)$ is a general function for the pion production spectrum, and

$$B_\pi = \frac{m_\pi c \cdot x''}{T_\pi \rho(x')}$$

The first term in the integrand of equ. (5.13) represents the loss of pions via decay and interaction, whilst the second term represents the primary nucleons lost through absorption in the atmosphere. With the assumption that the absorption lengths of the pions and nucleons are the same, $L_\pi = L_n = \lambda$, as discussed by Osborne (1966), and neglecting the energy loss of the pions and the weak dependence of B_π on x, a simplified expression for the pion intensity becomes

$$N_\pi(E_\pi, \ell(x,\theta)) = F(E_\pi) \cdot \exp\left(-\frac{\ell}{\lambda}\right) \cdot \ell \cdot \left(1 + \frac{B_\pi(x) \cdot \ell}{E_\pi \cdot x}\right)^{-1} \tag{5.14}$$

Thus, cosidering the possibility of pion to muon decay, the general expression for the muon production spectrum follows

$$N_\mu(E_\mu, \ell(x,\theta)) = \frac{2.341}{120} \cdot F(E_\pi) \cdot \exp\left(-\frac{\ell}{120}\right) \int_1^{1.746} S^{-(\delta+1)} \cdot \left(1 + \frac{S \cdot E_\mu x}{B_\pi \ell}\right)^{-1} \cdot dS \tag{5.15}$$

where the integral takes into account the decay spectrum of muons from pions in flight. Taking the sea level measurements of the vertical muon spectrum as a starting point, Osborne found that the pion production spectrum for all charged pions could be represented by the following relationships:-

$$F_\pi(E_\pi) = 7.16 \; 10^{-2}. \; A(E_\pi).E_\pi^{-1.93} \quad cm^{-2} \, s^{-1} \, st^{-1} \, GeV^{-1}$$

$$\text{for } E_\pi \leqslant 3.5 \; GeV \tag{5.16}$$

$$F_\pi(E_\pi) = 1.76 \; 10^{-1}. \; A(E_\pi).E_\pi^{-2.65} \quad cm^{-2} \, s^{-1} \, st^{-1} \, GeV^{-1}$$

$$\text{for } 3.5 < E_\pi < 2000 \; GeV \tag{5.17}$$

where A varies slowly with energy and has a value close to unity.

The inclusion of a contribution through kaon production follows similar arguments but as shown by Osborne, whether half the secondaries produced in the nuclear interactions are kaons or whether only pions are produced, the calculated muon intensities at large zenith angles show only a 5% sensitivity for muons arriving with energies around 100 GeV; the sensitivity falls off with decreasing muon energy. The geomagnetic effect only becomes important at energies less than 100 GeV and so for the purposes of the present work pions will be considered as the only muon parents and having a production spectra with general characteristics as described in equs. (5.16) and (5.17).

5.3.3. The effects of the Earth's Magnetic Field

Under the influence of the geomagnetic field after production the muons will suffer opposite deflections dependent on their charges with consequential differing path lengths to sea level. For those muons detected in the eastern azimuth the positive muons will have travelled longer distances than the corresponding negative muons. If one can assume a pion production spectra, therefore, for each charge as represented by $F_\pi^{\pm}(E_\pi)$ and neglecting any anisotropy produced in the incident proton beam or any deflection of the secondary pions in the short distance travelled between production and decay through geomagnetic deflection,

then the differential muon spectra for each charge assumes the form

$$\eta_\mu^\pm (E_0, \theta, \varphi) = \int_{x_0}^{0} N_\mu^\pm (E_\mu(x, E_0, \theta, \varphi), \ell(x, \phi)) . SP^\pm (E_\mu(x, E_0, \theta, \varphi), \ell(x, \phi))$$

$$. J\left(\frac{E_\mu, \phi, \Sigma, y, z}{E_0, \theta, \varphi, v, w}\right). \sin \theta. dx \quad GeV^{-1} sr^{-1} cm^{-2} s^{-1} \quad (5.18)$$

where

$$N_\mu^\pm = B. \frac{F_\pi^\pm(E_\pi)}{120}. \exp\left(-\frac{\ell(x, \phi)}{120}\right) \int_{1}^{1.746} S^{-(\gamma+1)} \left(1 + \frac{S. E_\mu. x}{B \pi. \ell(x, \phi)}\right)^{-1}. dS \quad (5.19)$$

and the affixes denote the muon charge..

At the largest zenith angles, where the geomagnetic effect is greatest, the majority of pions will decay rather than interact such that the integral in equ. (5.19) is approaching the value for complete decay and so may be approximated by a pion decay factor $D^\pm$ such that

$$D^\pm = a\left(1 + \frac{E_\mu. \rho(x)}{1.3884 \ 10^{-4}. \ell(x, \phi)}\right)^{-1}. \quad (5.20)$$

This approximation is tantamount to saying that the decay mouns are produced with a constant fraction of the parent energy, such that

$$E_\mu = \frac{m_\mu}{m_\pi}. E_\pi. \quad (5.21)$$

Suppressing the function parameters, in equ. (5.18) for simplicity in presentation and gathering together the constants into a term B', equ. (5.18) becomes

$$N_\mu^\pm = B'^\pm \int (E_\mu^\pm)^{-\gamma^\pm}. \exp\left(-\frac{\ell}{120}\right). D^\pm. SP^\pm. J^\pm. d\ell .$$

Assuming that the shape of the respective production spectra for the positive pions and negative pions are the same and of the form of the total spectrum as computed by Osborne, then $B'^+/B'^- = Rp$ where Rp is the charge ratio of muons at production. It follows immediately that

the charge ratio of the sea level muon flux, R_I, is given by

$$R_I = R_P \frac{\int (E_\mu^+)^{-2.65} \exp(-\ell/120). D^+. SP^+. J^+ \, d\ell}{\int (E_\mu^-)^{-2.65}. \exp(-\ell/120). D^-. SP^-. J^- \, d\ell} \qquad (5.22)$$

Since for muons of both kinds arriving at sea level along the meridian, the trajectories will be deflected similarly, the values of the integrands in equ. (5.22) will be identical such that $R_I = R_p$; a definition of the geomagnetic correction factor g follows directly:

$$g = \frac{\int (E_\mu^-)^{-2.65}. \exp(-\ell/120). D^-. SP^-. J^- \, d\ell}{\int (E_\mu^+)^{-2.65}. \exp(-\ell/120). D^+. SP^+. J^+ \, d\ell} \qquad (5.23)$$

Apart from the effects of the geomagnetic deflection, further modulations on the muon spectra; especially at low energies, are expected as a consequence of Coulomb scattering of the muons before detection. The scattering effect has been considered as a separate correction factor operating on g in sect. 5.5.

5.4. Calculations of the Geomagnetic Correction Factors.

5.4.1. Previous Calculations

For zenith angles greater than 80° and for different production depths and a number of geomagnetic azimuthal angles the propagation parameters, survival probabilities and deflections have been evaluated by Okuda (1963) and Maeda (1961). As these workers did not provide a comprehensive description of all the important parameters for the calculation of the geomagnetic correction factor, equ. (5.23), and since there does not exist any simple relationship between the geo-magnetic effect at different points of observation on the earth's

surface then, as far as the present work is concerned, their results are of academic interest only.

For the geomagnetic conditions of the previous Durham horizontal spectrographs, inclined at 7.8° East of the magnetic meridian, Kamiya (MacKeown, 1965) calculated a geomagnetic correction factor assuming a propagation of muons, produced at a unique atmospheric depth $(1(x,\phi) = 120 \text{ g cm}^{-2})$, under the influence of the horizontal component of the geomagnetic field only. The correction factor was assumed to be of the form

$$g = ((E^{-})^{-2.64}.SP^{-}.D^{-}/((E^{+})^{-2.64}.SP^{+}.D^{+}) \ . \tag{5.24}$$

For sea level muon energies below 10 GeV, as well as atmospheric scattering becoming important, the approximation of a unique depth of production was expected to impose severe restrictions on the applicability of the above factor, as has been discussed by Aurela et al. (1966). The effect of the one dimensional description was estimated to be small but causing an underestimate of the required correction factor. The cell width factor, arising through the Jacobian, was not considered.

The axis of the present spectrograph lay along a line 27° East of the geomagnetic meridian, and consequently, the extent of the geomagnetic effect was severe; a more rigorous approach to the problem than had previously been undertaken was demanded.

5.4.2. Present Calculations

Preliminary calculations showed that the variations in the value of the Jacobian, as evaluated for muons produced over the important first
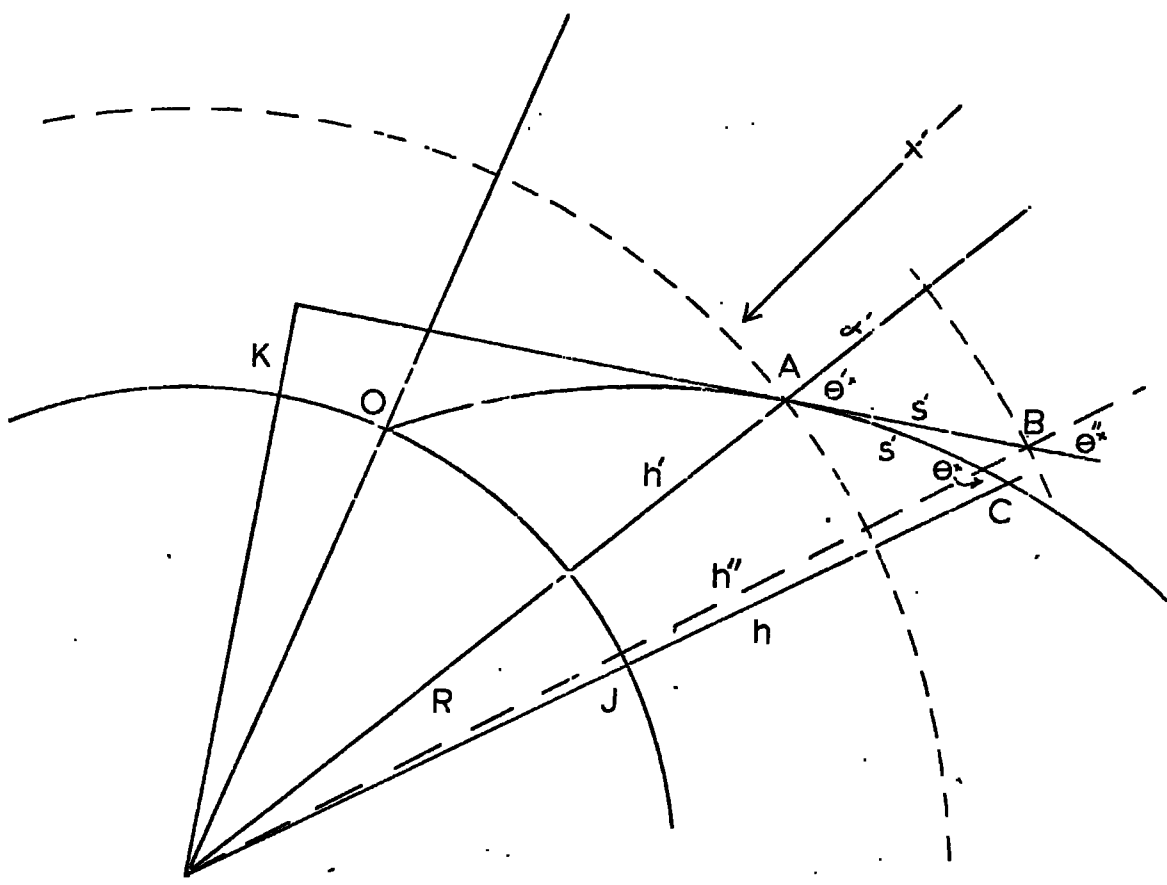
Fig. 5.3   Trajectory element

few hundred g cm^{-2} of the atmosphere, were small and so to a good approximation equ. (5.23) could be expressed in the form

$$g = \frac{J_{120}^{-}\int(E_{\nu}^{-})^{-2.65}.\exp(-\ell/120).D^{-}.SP^{-}.d\ell}{J_{120}^{+}\int(E_{\nu}^{+})^{-2.65}.\exp(-\ell/120).D^{+}.SP^{+}.d\ell} \qquad (5.25)$$

which for the purposes of the present treatment was convenient, allowing the problem to be broken down into three parts:-

a) Evaluation of the propagation parameters at various heights of production resulting in the solution of the integrands;

b) Calculation of the derivatives of the propagation parameters at a unique depth $1(x,\phi) = 120$ g cm^{-2}, these being needed in the evaluation of the Jacobian;

c) A consideration of the effects of Coulomb scattering on a) and b) separately.

5.4.3. Evaluation of the Propagation Parameters

For various arrival energies and zenith angles muon trajectories were constructed in an inverse computer simulation. The trajectory construction may be explained with reference to elements of the muon path from which the whole trajectory was comprised, fig. 5.3. The atmosphere was broken up into layers, typically of thickness α' g cm^{-2}; $\theta^{'*}$ represents the local zenith angle at point A at a depth x'; AO represents part of the trajectory already constructed. As AB is the tangent to the trajectory at A then from equ. (5.3) B must be at an altitude given by

$$h'' = 46.3807 - 13.3980.(x'-\alpha)^{0.179} \text{ km}. \qquad (5.26)$$

It follows, therefore, that

$$\theta''* = \text{Arcsin}\left[(K + R) / (h''-R)\right] \qquad \text{radians} \qquad (5.27)$$

where K is the propagation constant having the value

$$K = (R + h') . \sin(\theta'*) - R \text{ km.} \qquad (5.28)$$

Hence the separation of A and B follows directly and has a value

$$s' = (R + K).\left[1/\text{Tan}(\theta''*) - 1/\text{Tan}(\theta'*)\right] \quad \text{km.} \qquad (5.29)$$

Due to energy loss suffered by the muons in passing through the atmosphere, at points A and B on the trajectory the muon will have energies denoted by Ea and Eb. In the limit of small s', the muon energies may be related through

$$Eb = Ea + s.\rho(x' - \frac{\alpha}{2}) . \frac{dE}{dx}(\rho(x'- \frac{\alpha}{2}), Ea) \qquad (5.30)$$

where $\frac{dE}{dx}$ is defined as in equ. (5.8). The probability that the muon will travel the element of trajectory without decaying follows from equ. (5.11) and, again providing s' in small, becomes

$$SP' = \exp\left[- \frac{2.m_\mu c.s'}{c.\gamma_\mu.(E_a+E_b)}\right] \qquad (5.31)$$

Inorder to include the effects of curvature of the trajectory through geomagnetic deflection, it is convenient to retain s' as the elementary deflected path such that equs. (5.29) and (5.31) may be used without modification for the remainder of. the calculations. Therefore, it is necessary to calculate a modified local zenith angle and an altitude for C in figure 5.3. Providing that the elementary deflection δ is small and is in the plane containing the trajectory, the height of C may be approximated by

$$h = h'' - 0.5 \, s .\delta. \sin(\theta'* + \delta/2). \qquad (5.32)$$

Further,

$$\theta* \cong \theta'* + \delta \quad \text{and } E_c \cong E_b . \tag{5.33}$$

Since with high speed computers, such as the NUMAC IBM 360/67, it is possible to select values for s' such that the effect of the previous converging approximations are negligible, the above relationships provide the basis for an accurate computer trajectory reconstruction for muons travelling in a one dimensional magnetic field.

The geomagnetic field, however, can be resolved into a vertical and horizontal component causing the muon deflection to be in two dimensions. If AQ is the azimuthal angle of the muons relative to the local magnetic meridian, and δ is the deflection experienced by the the muons in the plane containing the centre of the earth and the tangent to the trajectory at the point of deflection,

$$\delta = (5.04.10^{-8}. \text{ Sin (AQ). Charge. s'})/P \text{ radians} \tag{5.34}$$

where P is the muon momentum expressed in units of GeV/c and s' is measured in centimetres, then the above description holds for the case of deflection in two dimensions. The approximation, which comes through the assumption of a pure rotation of the $\overline{(K + R)}$ vector, is of negligible effect as the lateral displacement of the muon trajectory is small relative to the magnitude of K + R for all zenith angles. The local azimuthal deflection which is accumulative in AQ, may be expressed by

$$\delta_A = (1.3567 \ 10^{-7}. \text{ Sin } (\theta*). \text{ Charge. s'})/P \text{ radians} . \tag{5.35}$$

In arriving at the above relationships for the magnetic deflections, the components of the geomagnetic field at Durham were taken to be

$$H_z = 0.168 \text{ gauss}$$

$$H_v = 0.452 \text{ gauss} .$$

Any variation in the components of the magnetic field along the muon
trajectory are only of minor importance but for completeness, they were
included in the calculations through the approximations

$$\delta \cong \delta (1 - OJ. \cos (AQ). 2.41 \ 10^{-4}) \\ \delta_A \cong \delta_A(1 + OJ. \cos (AQ). 8.45 \ 10^{-5})$$ (5.36)

OJ being measured in kilometres along the surface of the earth, c.f.
fig. 5.3.

The trajectory was constructed element by element; the total
probability of survival over the constructed trajectory was simply the
product of the survival probabilities over each element. At a number
of preselected depths in the atmosphere, the trajectory construction
was halted; the path length along the tangent to the trajectory from
this point to the top of the atmosphere was computed numerically. Also,
the pion decay factor as defined in equ. (5.20) was computed. The
atmospheric slant depth and the pion decay factor were stored together
with such other information as the survival probability to sea level,
the muon energy, the path length and the production coordinates. The
term inside the integrals of equ. (5.25) was also computed and stored.
So, for a muon arriving at sea level with a particular charge, energy
and zenith angle, the muon propagation parameters for a number of
possible depths of production were available.

Intermediate values of the stored information, corresponding to
inclined production depths of 15, 30, 60, 120 ....960 g cm^{-2}, were
obtained to 1 part in 10^7 following the Aitken scheme for Lagrange
interpolation; the high accuracy was necessary for subsequent

Fig. 5·4
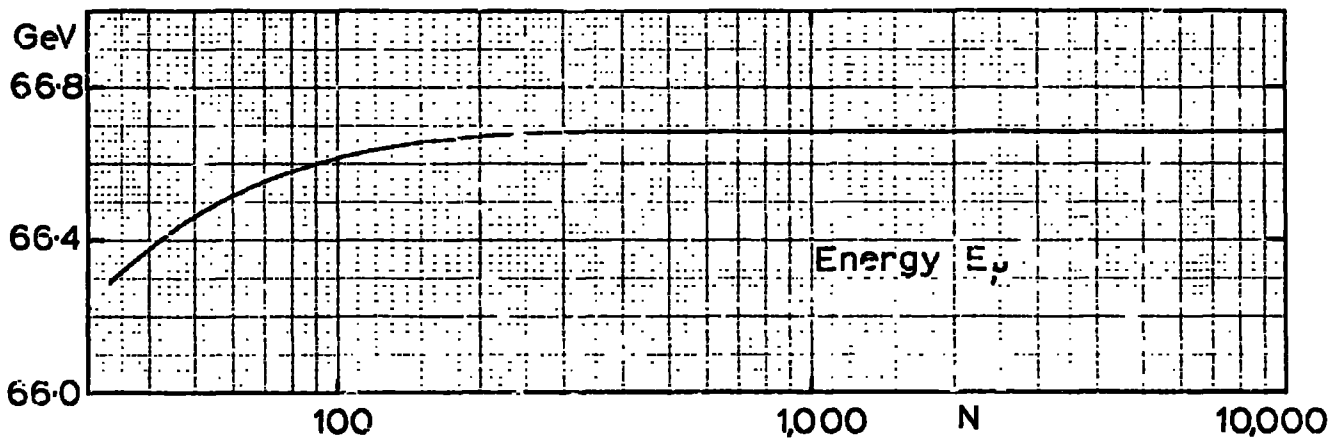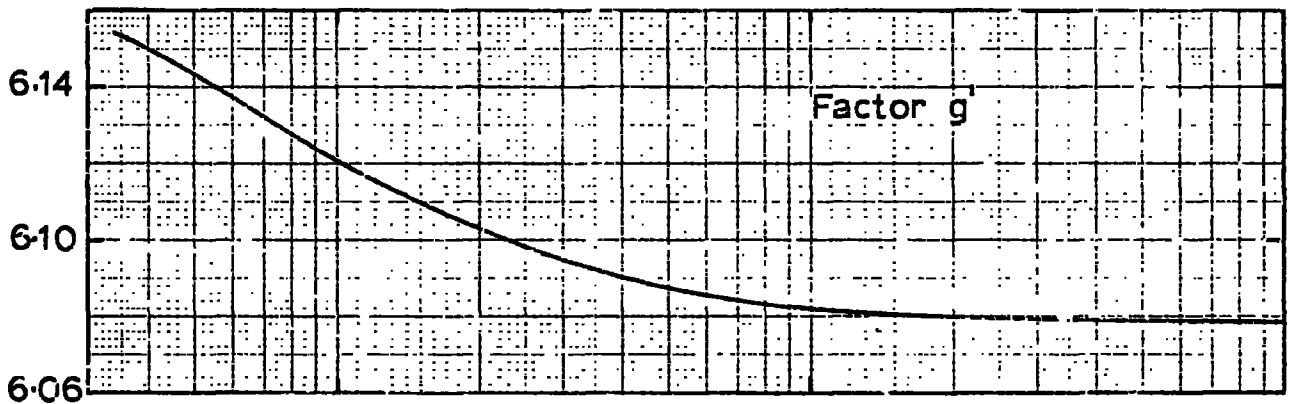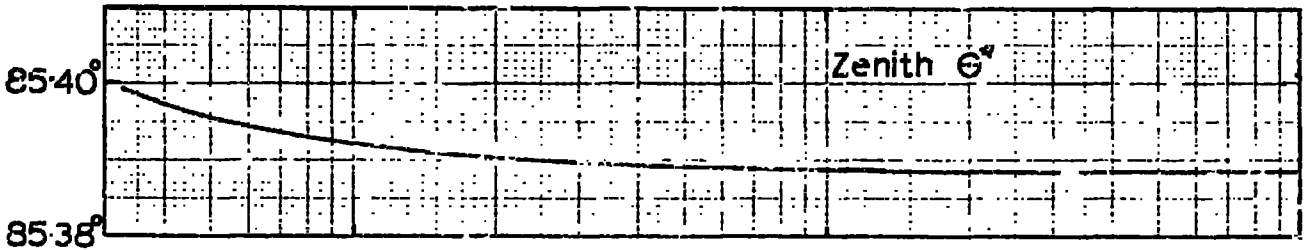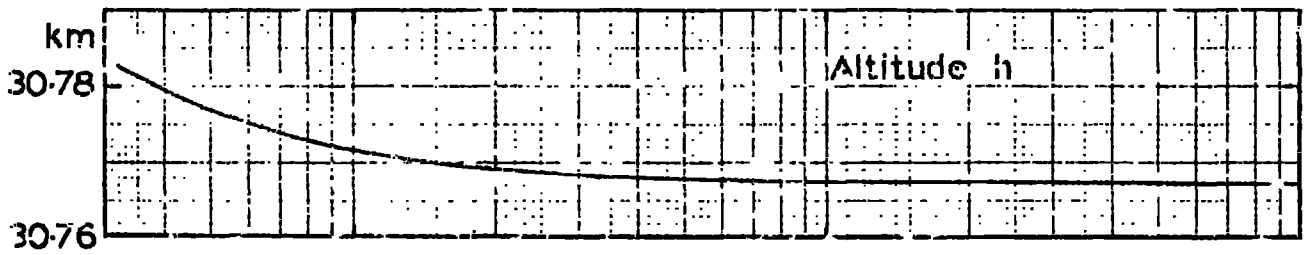
Sensitivity of the computed values to the number of elements comprising the constructed trajectories between $x = 65$-1030 g cm^{-2} ; $\theta = 87.5$, $E = 4$ GeV, ℓ - 33 , $\ell = 120$ g cm^{-2} .

computations on the Jacobians.

Fig. 5.4. shows the variation of some of the production parameters with the number of track elements comprising the trajectory for an inclined production depth of 120 g cm^{-2}; N represents the number of elements between the vertical depths 65 and 1030 g cm^{-2}. The plotted function g' represents the ratio of the integrals in equ. (5.25) through the approximation

$$g' = \frac{\sum_{\ell=1}^{5}\left((E^-_{(m)})^{-2.65} SP^-_{(m)}.D^-_{(m)}.\exp(-m/120).\frac{2}{3}m(\ell)\right)}{\sum_{\ell=1}\left((E^+_{(m)})^{-2.65} SP^+_{(m)}.D^+_{(m)}.\exp(-m/120).\frac{2}{3}m(\ell)\right)}$$

where m(1) = 30. 2^{-1}.

Figs. 5.5 a,b   demonstrate the near exponential dependance of the function g' on arrival azimuthal angles for Durham based spectro-graphs. Since the total muon spectrum varies only slowly with azimuthal angle, the effective arrival direction of the muons in the azimuth, for the purposes of an overall computed correction factor, may be found simply by weighting the azimuthal acceptance function with g'; the effective arrival direction can be taken as the so weighted mean azimuthal angle over the azimuthal range. In consideration of the case of the present spectrograph for high momentum particles, the main geometries could be represented by arrival directions in the azimuth of 21.6° and 32.4°. At large zenith angles, for particles with momenta 3 Gev/c, however, the weighted mean arrival angles were found to be close to 22° and 33°. Since it is at these large zenith angles and low energies that g' varies most rapidly with azimuthal angle, the angles 22° and 33° were used throughout the computations as represen-tative of the spectrograph's main geometries. Similarly for the previous horizontal Durham spectrographs, the axes of which lay along a line

Fig. 5·5a

$E_o = 2$ Gev

$\Theta = 88·75°$

$86·25°$

$83·75°$

$81·25°$

$78·75°$

$76·25°$
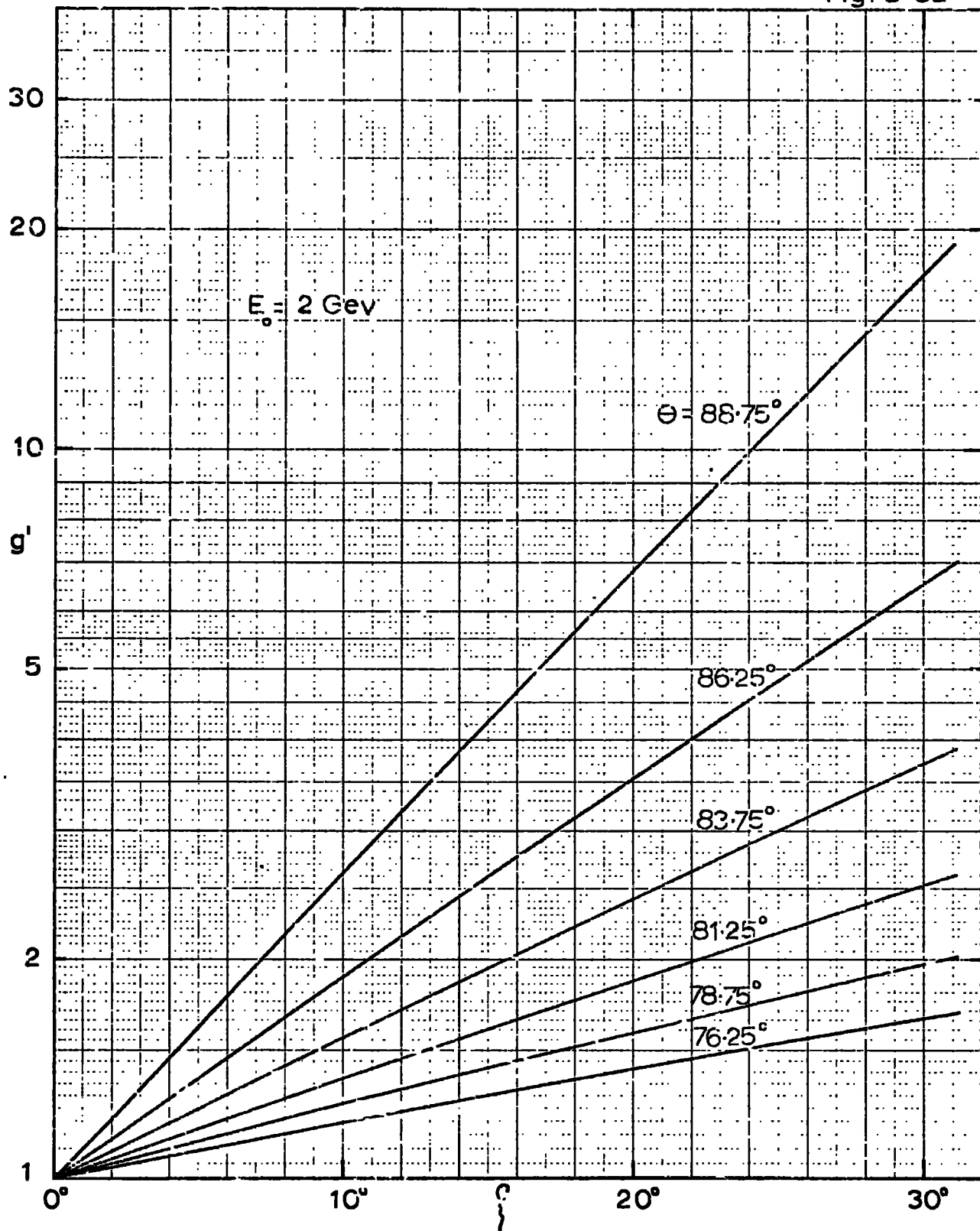
Fig. 5.5b
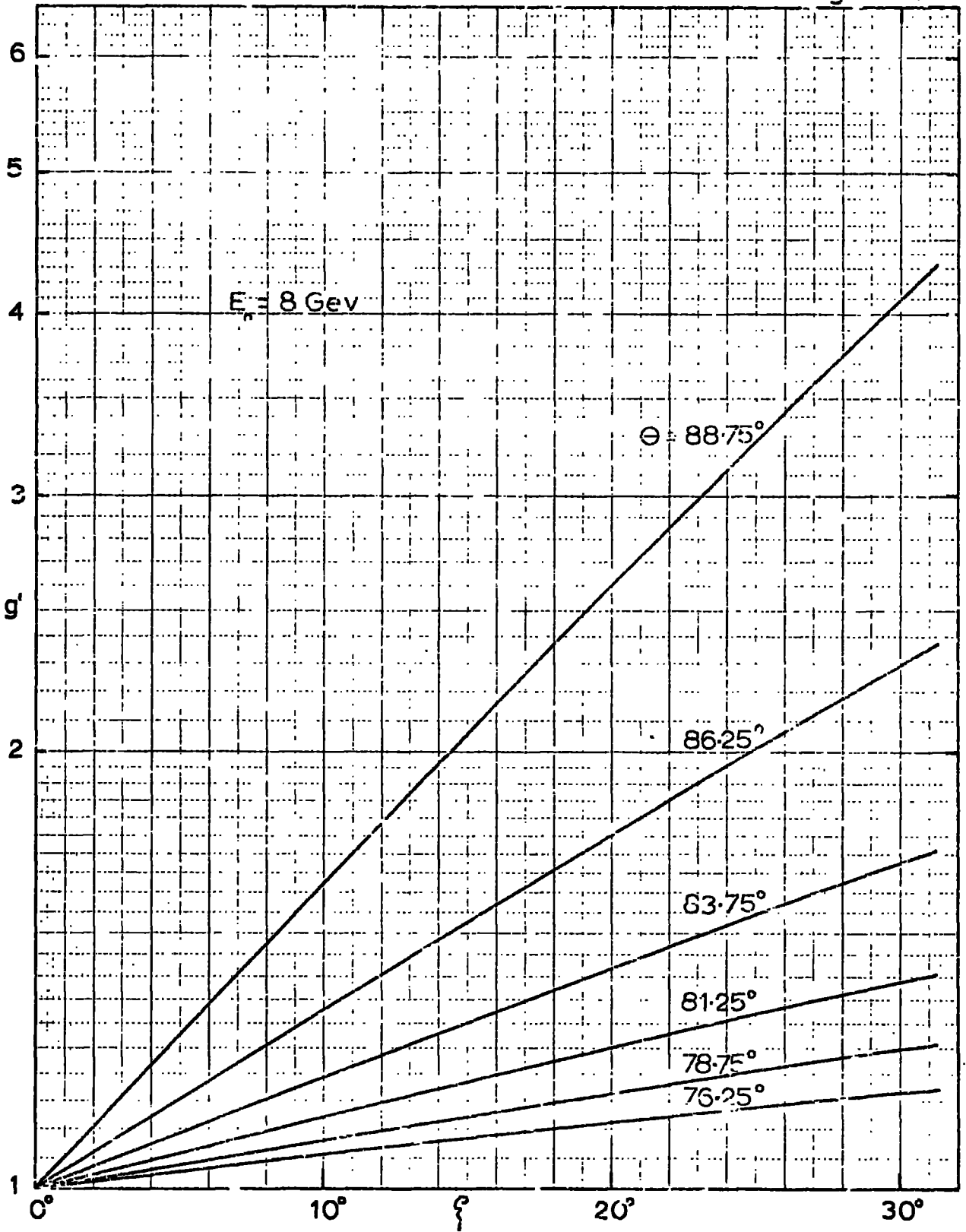
The correction term g'. ._ _ _ _ represents $(S/S^+).g'$

Fig. 5·6a

$\zeta = 33°$

$88·75°$

$86·25°$

$83·75°$

$81·25°$

$78·75$

$\Theta = 76·25°$

g'

5·0

4·0

3·0

2·0

1·0

10   E_μ at sea level (GeV)   100

Fig. 5·6b

Fig. 5.6c

Fig. 5.7a

Fig. 5.7b

Fig. 5·7c
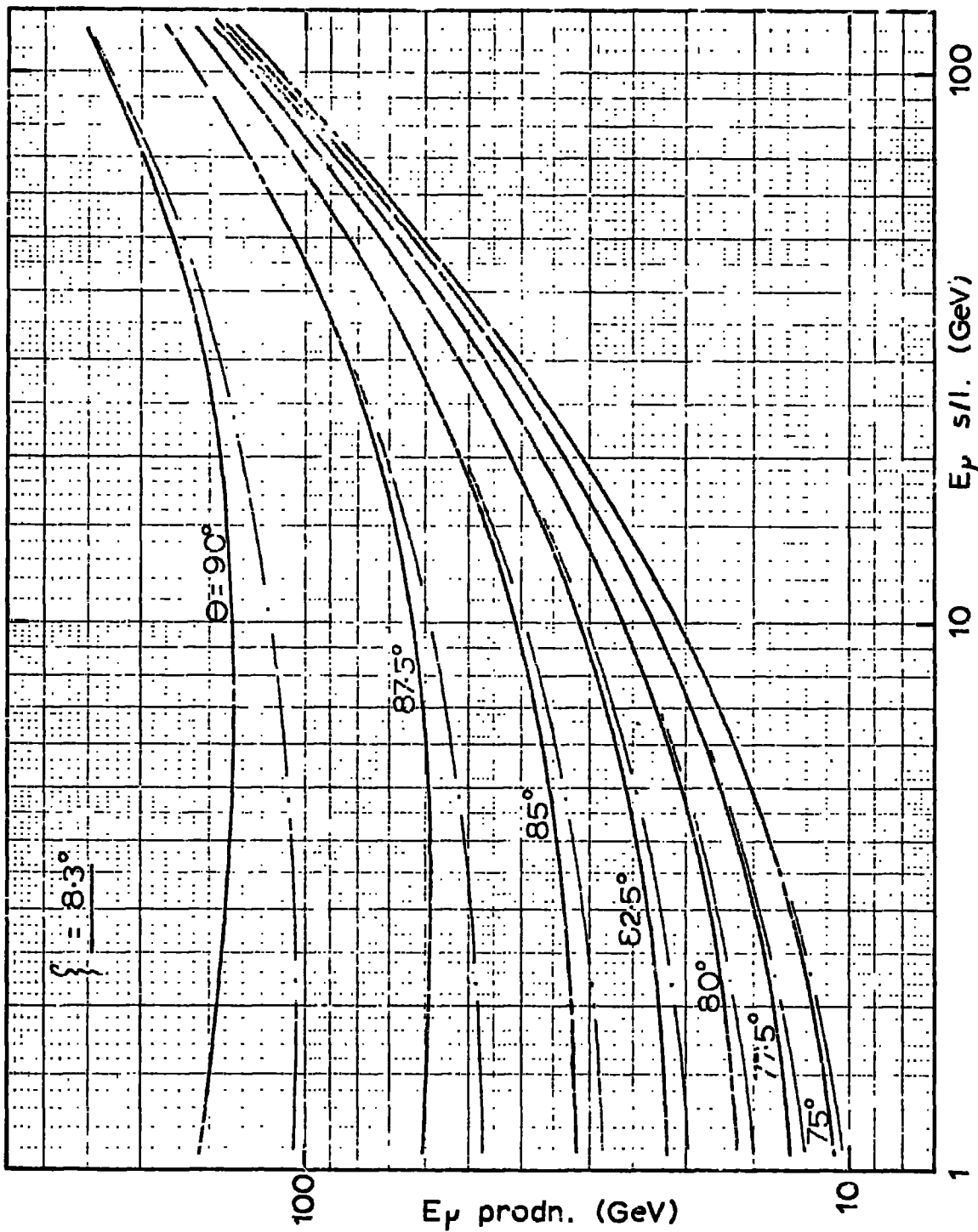
$\theta = 90°$

$\xi = 8·3°$

$87·5°$

$85°$

$82·5°$

$80°$

$77·5°$

$75°$

E_μ s/l. (GeV)

E_μ prodn. (GeV)

Fig. 5.8a

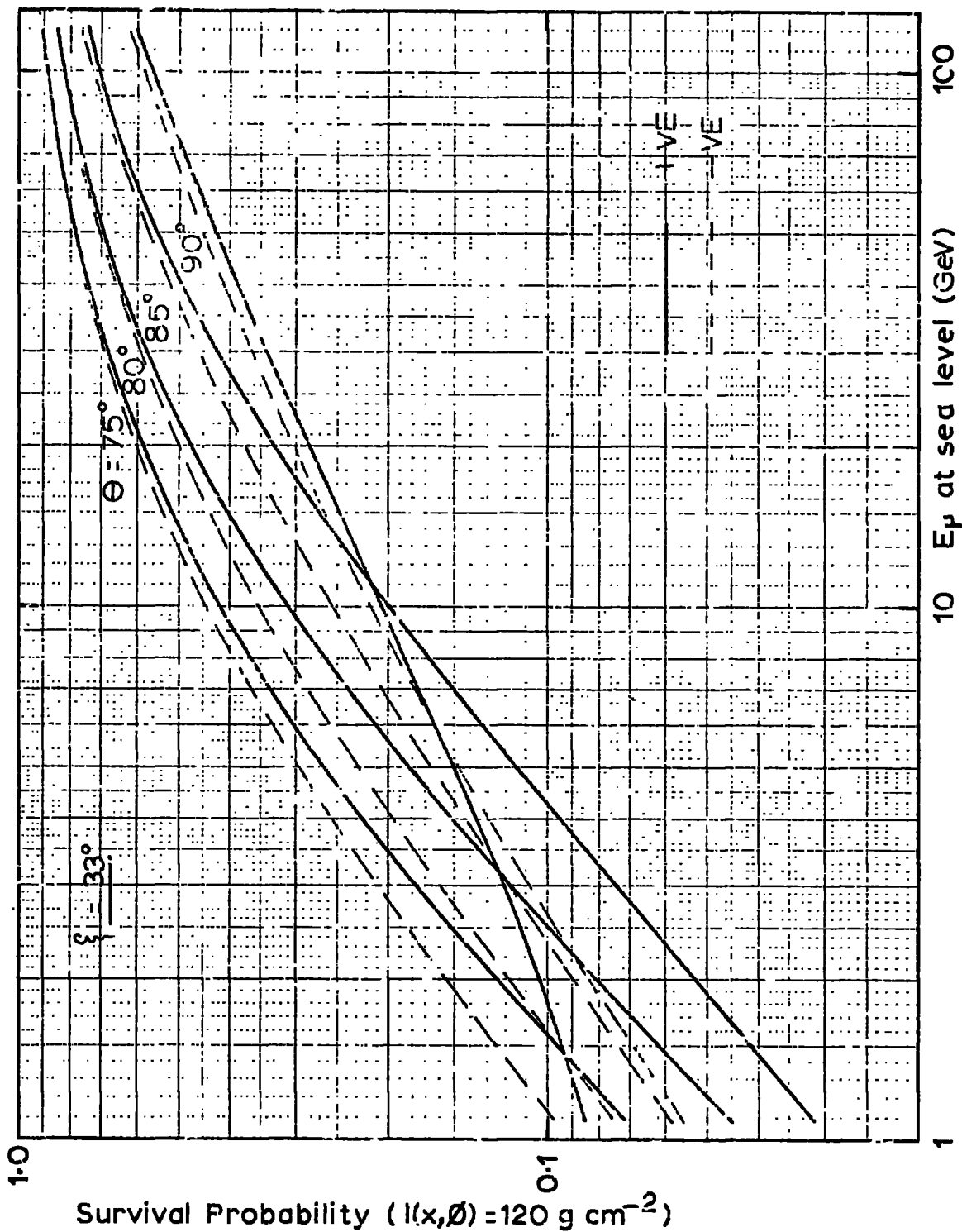Survival Probability ($I(x,\emptyset)$ =120 g cm^{-2})
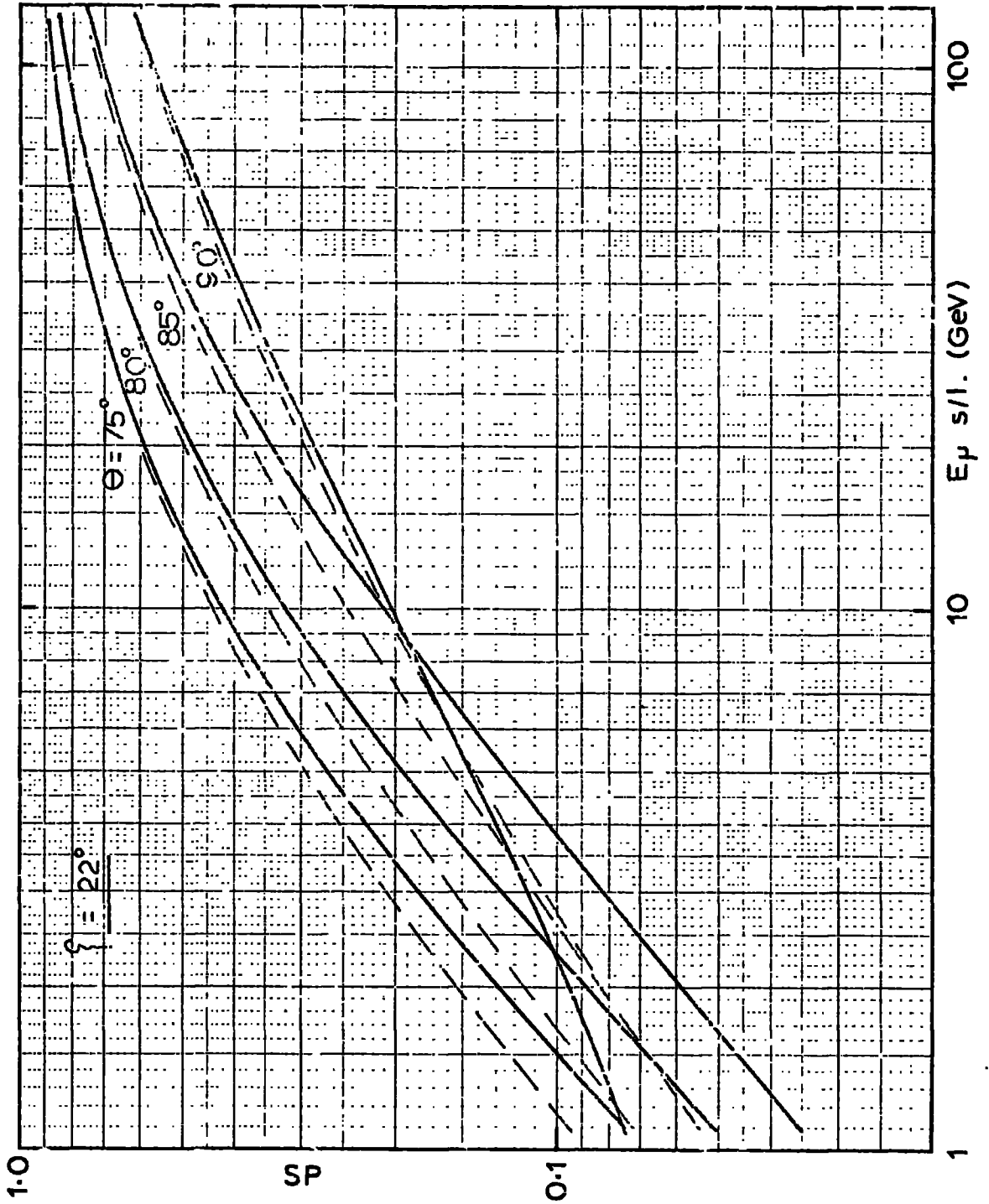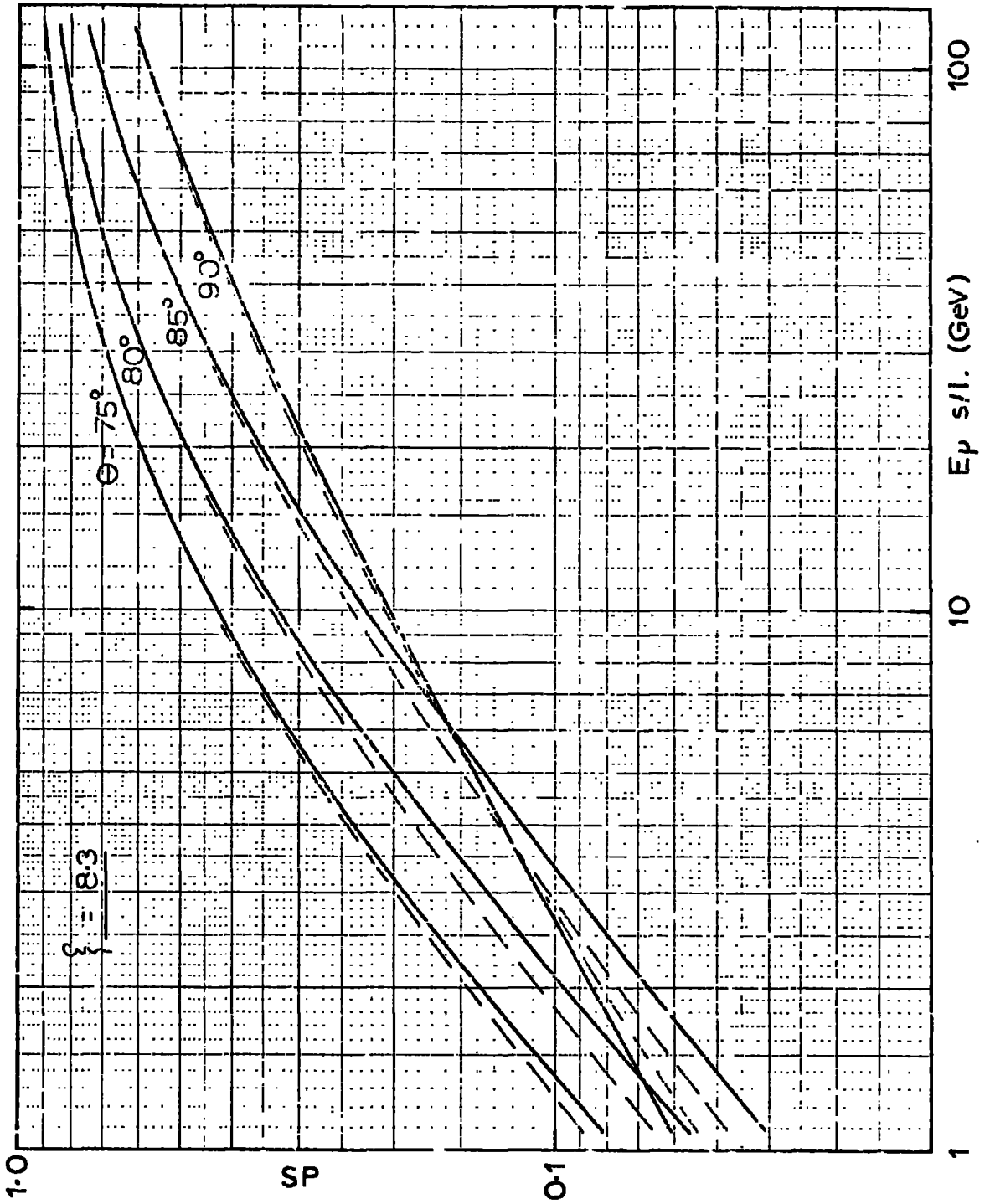
Fig. 5.8b

Fig. 5.8c

7.8^O East of the geomagnetic meridian, the operative azimuthal direction was 8.3^O East of the geomagnetic meridian.

Figs. 5.6. to 5.8 show the calculated variations of g', E and SP with sea level energy and zenith angle for each of the mean arrival azimuthal angles 33°, 22° and 8.3^O.

5.4.4. The Cell Width Factor

The cell width factor which appears through the Jacobian in equ. (5.12.) may be represented in determinant form

$$J_l\left(\frac{E_\nu, \emptyset, \Sigma, y, z}{E_o, \theta, \gamma, v, w}\right) =$$

$$\begin{vmatrix} \frac{\partial E_\nu}{\partial E_o} & \frac{\partial \emptyset}{\partial E_o} & \frac{\partial \Sigma}{\partial E_o} & \frac{\partial y}{\partial E_o} & \frac{\partial z}{\partial E_o} \\ \frac{\partial E_\nu}{\partial \theta} & \frac{\partial \emptyset}{\partial \theta} & \frac{\partial \Sigma}{\partial \theta} & \frac{\partial y}{\partial \theta} & \frac{\partial z}{\partial \theta} \\ \frac{\partial E_\nu}{\partial \gamma} & \frac{\partial \emptyset}{\partial \gamma} & \frac{\partial \Sigma}{\partial \gamma} & \frac{\partial y}{\partial \gamma} & \frac{\partial z}{\partial \gamma} \\ \frac{\partial E_\nu}{\partial v} & \frac{\partial \emptyset}{\partial v} & \frac{\partial \Sigma}{\partial v} & \frac{\partial y}{\partial v} & \frac{\partial z}{\partial v} \\ \frac{\partial E_\nu}{\partial w} & \frac{\partial \emptyset}{\partial w} & \frac{\partial \Sigma}{\partial w} & \frac{\partial y}{\partial w} & \frac{\partial z}{\partial w} \end{vmatrix}_{l\ const} \tag{5.38}$$

The variables being as defined in sect. 5.2.

As a consequence of the earth's diameter being large compared with the thickness of the atmosphere, small translations along the direction of w will cause negligible variations in the production parameters E, $\emptyset, \Sigma$ and y, and considering that the total azimuthal deflection is less

than 20 degress in the worst case, $(\partial z/\partial W)$ has a value close to unity. Consequently, the Jacobian may be approximated by the Jacobian $J(\frac{E, \theta, \Sigma, v}{E_o, \theta, \phi, v})$; the corresponding determinant is enclosed by the dotted lines in equ. (5.38).

Inorder to achieve an accuracy of 1% over the ranges covered in the present experiment, a value of N = 489 was used for trajectory construction, c.f. fig. 5.4. It was also necessary to ensure an internal consistancy within the programme of 1 part in 10^7. Although it would have been possible to have included the Jacobian in the treatment of the previous section by direct numerical differentiation of the stored production parameters, the amount of central processor time and storage space needed in such a computation was prohibitive. Making use of the approximate relationship in equ. (5.25), the Jacobian, for a fixed production depth $l(x, \theta) = 120$ g cm^{-2}, was computed by an examination of the variations in the production parameters resulting from small incremental variations in the sea level parameters. By this method it was possible to evaluate the Jacobian for four energies and four zenith angles using 79 k bytes of the IBM 360 main core store; the central processor was engaged for 20 minutes only.

In these calculations, as for those in the previous section, the trajectories were constructed assuming the static atmosphere outlined in sect. 5.2. The effects of scattering were not included in the treatment.

For the arrival azimuthal angles $33°$, values for J^+_{120} and J^-_{120} have been plotted seperately in figures 5.9 a,b. In figures 5.10 a,b,c the variation of the ratio J^-_{120}/J^+_{120} with sea level energy and zenith
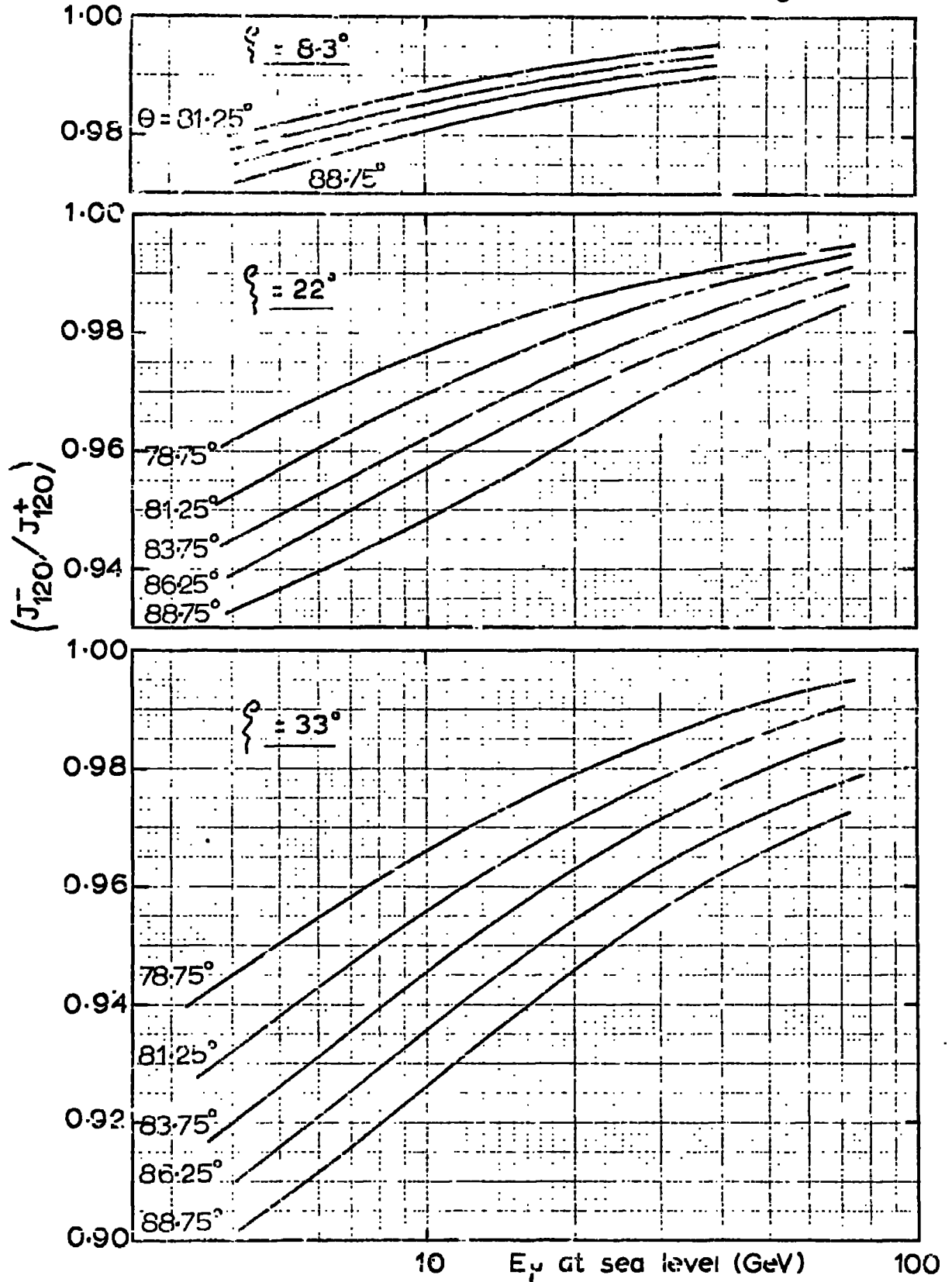
Fig. 5.9
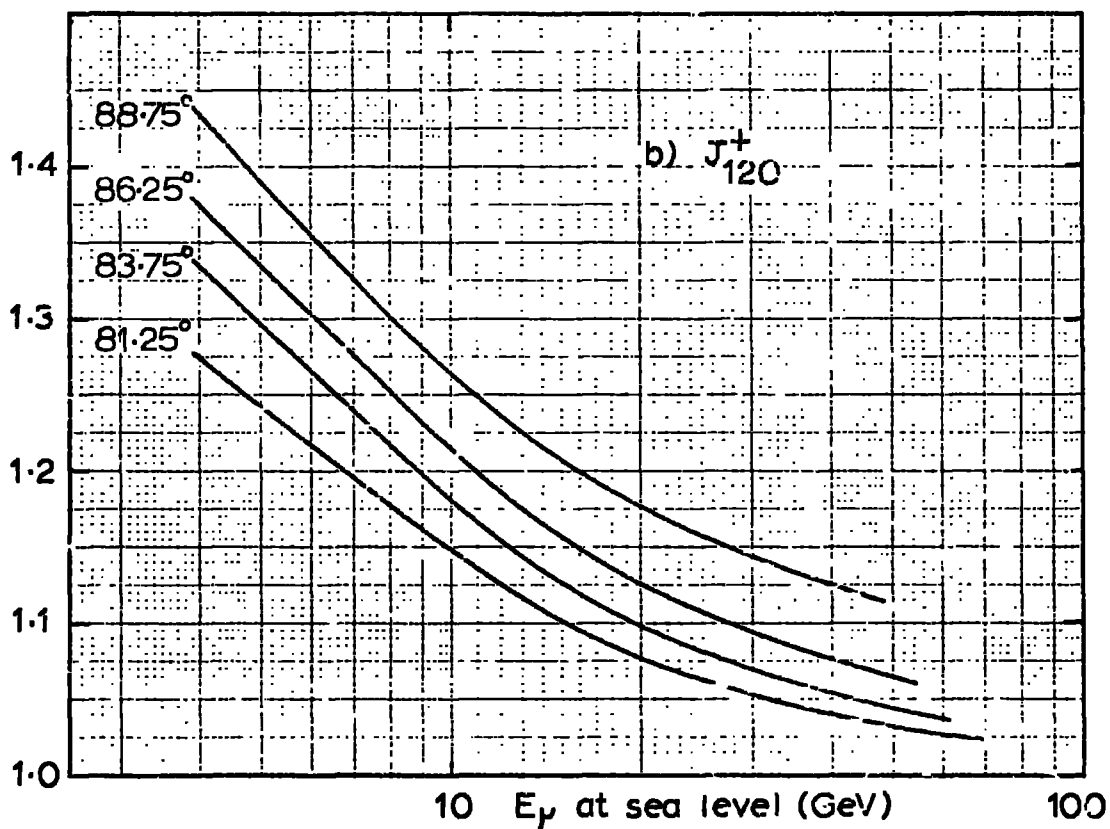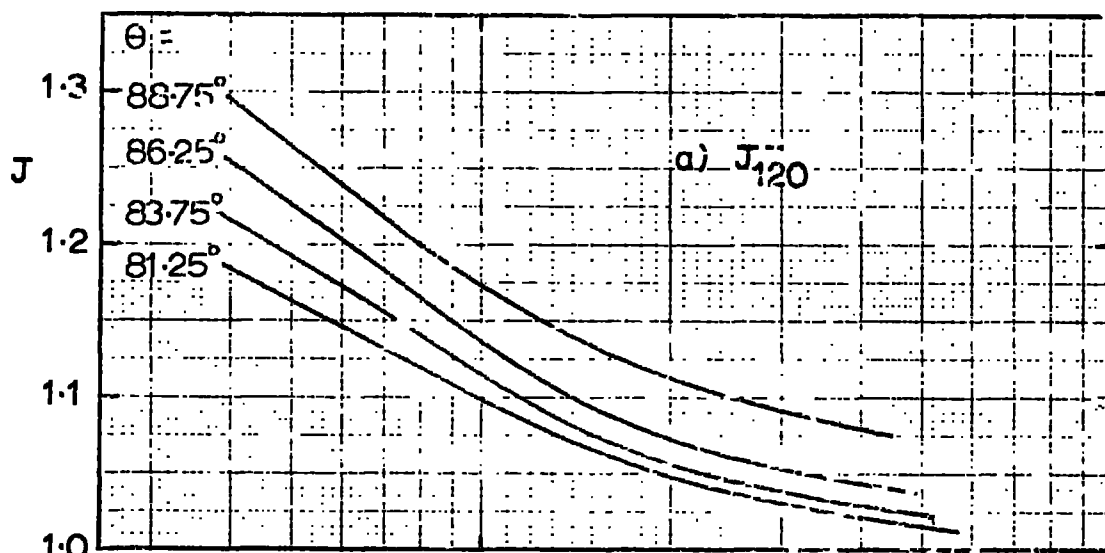
The Jacobian for positive and negative muons
evaluated for a prodn. depth 120 g cm^{-2}, $\xi = 33°$

Fig. 5·10

The Cell Width Factors plotted against E_μ at sea level (GeV), for $\zeta = 8·3°$, $\zeta = 22°$, and $\zeta = 33°$, with curves labelled by $\theta = 31·25°$, $78·75°$, $81·25°$, $83·75°$, $86·25°$, $88·75°$. Vertical axis $\left(J^-_{120} / J^+_{120}\right)$.

angle are shown for azimuthal angles 33°, 22° and 8.3^O.

5.5. Corrections for Local and Atmospheric Scattering

The treatment of the propagation problem so far has ignored the effects of Coulomb scattering. For a particular angle of production Coulomb scattering in the atmosphere will cause the arrival direction of the muon to vary about the expected sea level arrival angle for a propagation without scattering. Due to the rapidly falling nature of the muon spectrum with increasing zenith angle, the effect of scattering will be to produce an enhancement in the muon flux at these largest zenith angles.

As can be seen from the discussion of sect. 5.4, the non scattered angular spectrum for positive muons is appreciably steeper than that for negative muons, hence the correction to each must be different. Defining spectra enhancement through factors S^+ and S^- where

$$S^\pm = (\text{intensity}^\pm \underline{\text{with}} \text{ scattering})/(\text{intensity}^\pm \underline{\text{without}} \text{ scattering}) \tag{5.39}$$

then the geomagnetic correction factor, including the effects of Coulomb scattering, follows

$$g_s = (S^- / S^+) \, g. \tag{5.40}$$

The effects of Coulomb scattering on the muon spectrum has been considered previously by such authors as Allen and Apostalakis (1961), and Osborne (1966).

Allen and Apostalakis assumed that the angular spectrum could be approximated by

$$I(\theta) = I_o \exp(-k\theta) \tag{5.41}$$

and assuming that the scattering took place at sea level, used the relation as derived by Lloyd and Wolfendale (1955)

$$S = \exp(k^2 \sigma^2/2) \tag{5.42}$$

where σ should be the projected r.m.s. angle of scatter in the zenith plane which may be approximated by

$$\sigma^2 = 5.85 \ 10^{-6} \ (\text{path length, g cm}^{-2})/(E_o.E). \tag{5.43}$$

For zenith angles greater than 80°, the approximation of equ. (5.41) begins to break down. It would appear, however, that these authors used the total r.m.s. angle of scatter in evaluating S and so the square root of their values would be more realistic.

Osborne attempted the solution of the scattering problem through a Monte Carlo treatment. However, in his final interpretation of the scattered data, Osborne took the scattered intensity value to be that intensity associated with some mean"production environment" rather than taking an integral contribution from all possible production environments, so over estimating the scattering effect. From crude considerations, it would again appear that an approximation to the true scattering factors would be to take the square root of the Osborne values; this would account for the reasonable agreement between these results and those of Allen and Apostalakis.

Although it can be seen from the above discussions that the effect of atmospheric scattering is of less importance than hitherto realized, for the present experiment, however, the situation was complicated

63.

TABLE 5.1.

CONTRIBUTIONS TO SCATTERING

(Azimuth 33°)

Energy (Gev)	Zenith Angle (degrees)	σ_{local}	$\sigma_{air}{}^{+}$ (degrees)	$\sigma_{air}{}^{-}$
2.0 ↓	88.75	1.27	1.76	1.80
	86.25	1.27	1.79	1.82
	83.75	2.01	1.82	1.82
	81.25	1.56	1.82	1.82
	78.75	1.56	1.80	1.80
	76.25	0.90	1.79	1.79
32.0 ↓	88.75	0.08	0.35	0.34
	86.25	0.08	0.32	0.31
	83.75	0.13	0.29	0.28
	81.25	0.10	0.26	0.26
	78.75	0.10	0.25	0.24
	76.25	0.06	0.23	0.23

through muons, prior to detection by the spectrograph, being scattered in local structures. Fig. 5.11 is an angular representation of the local scattering elements; the dimensions refer to their thicknesses as measured in radiation lengths. 'A' represents a local building, and 'B' represents the steel and barytes screening associated with the Durham Horizontal Air Shower Array. The shaded areas in the diagram indicate those parts of the structures which obstructed the 33° geometry of the spectrograph only. The relative importance of atmospheric scattering to local scattering can be seen from an examination of the calculated values of the projected r.m.s. angles of scatter listed in table 5.1. σ_{air} values were calculated using equ. (5.43).

For the purposes of calculating the scattering correction for the present case, the muons were assumed to pass through the atmosphere unaffected by scattering and then were there redistributed in the zenith plane through a local scattering process. The resultant zenith angles were distributed about the original arrival direction in a Gaussian form, characterised by a standard deviation

$$\sigma = (\sigma^2_{local} + \sigma^2_{air})^{\frac{1}{2}}. \tag{5.44}$$

For the calculations, the unscattered muon intensities were estimated using the denominator and numerator of equ. (5.37). The values of $S^{\pm}$ were simply the ratios of the number of muons in each zenith cell after scattering to the number of muons in each zenith cell prior to scattering. The values of $(S^-/S^+).g'$ are denoted by the dashed curves in figures 5.6 a,b,c.

The scattering effect is discussed further in Appendix B2.

Fig. 5·11 Scattering elements

A
B

Array telescope

77·5°
82·5°
85°

9

45 9

Geography
Department

Array
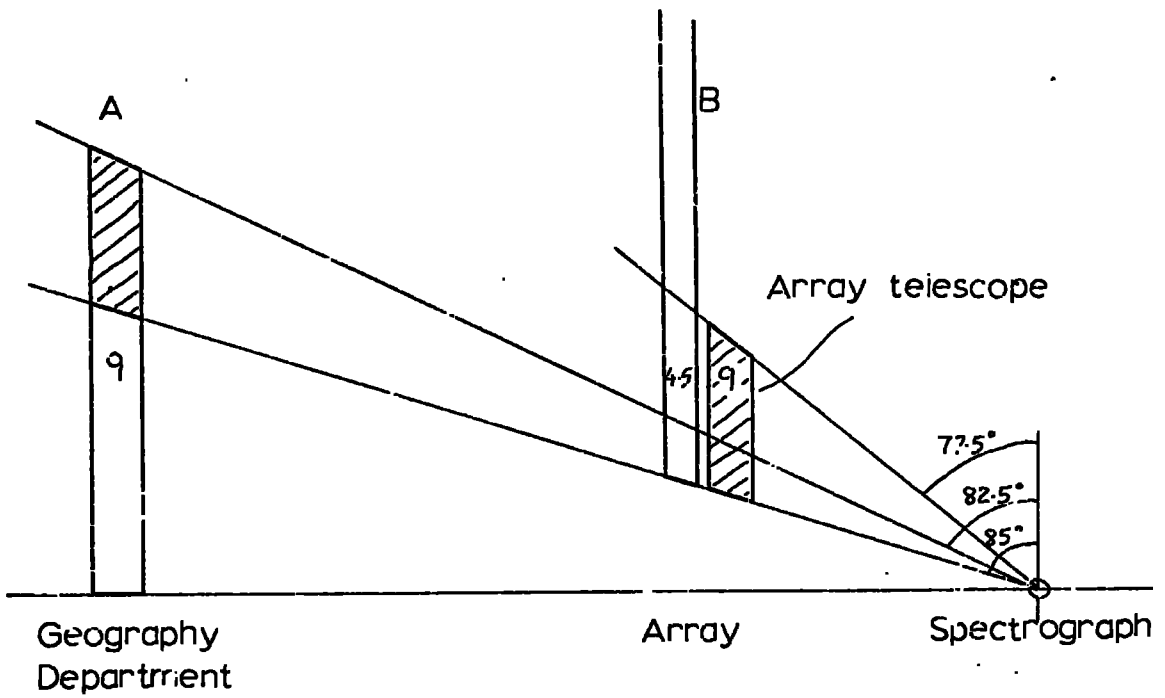
Spectrograph

Dimensions in radn. lengths

▨ at 33° only

CHAPTER 6

THE EXPERIMENTAL MUON CHARGE RATIO

6.1. The Charge Ratio of the Incident Muons

The resultant data from the main geometries of the spectrograph, as presented in table 4.1 a,b, were converted separately to the expected charge ratio values prior to detection. The charge ratio of the incident muons differed from the charge ratio of the observed muons because of the effect of instrumental noise as is discussed in sect. 3.3. The resultant charge ratio values from both geometries were combined and are presented as a single set in fig. 6.1. Muons arriving with momenta less than 1 GeV/c were not included.

In obtaining the combined values for the incident ratios, the following method was employed. With reference to the argument outlined in Appendix B1, it was necessary to represent the individual ratios in the form of a charge excess δ defined through
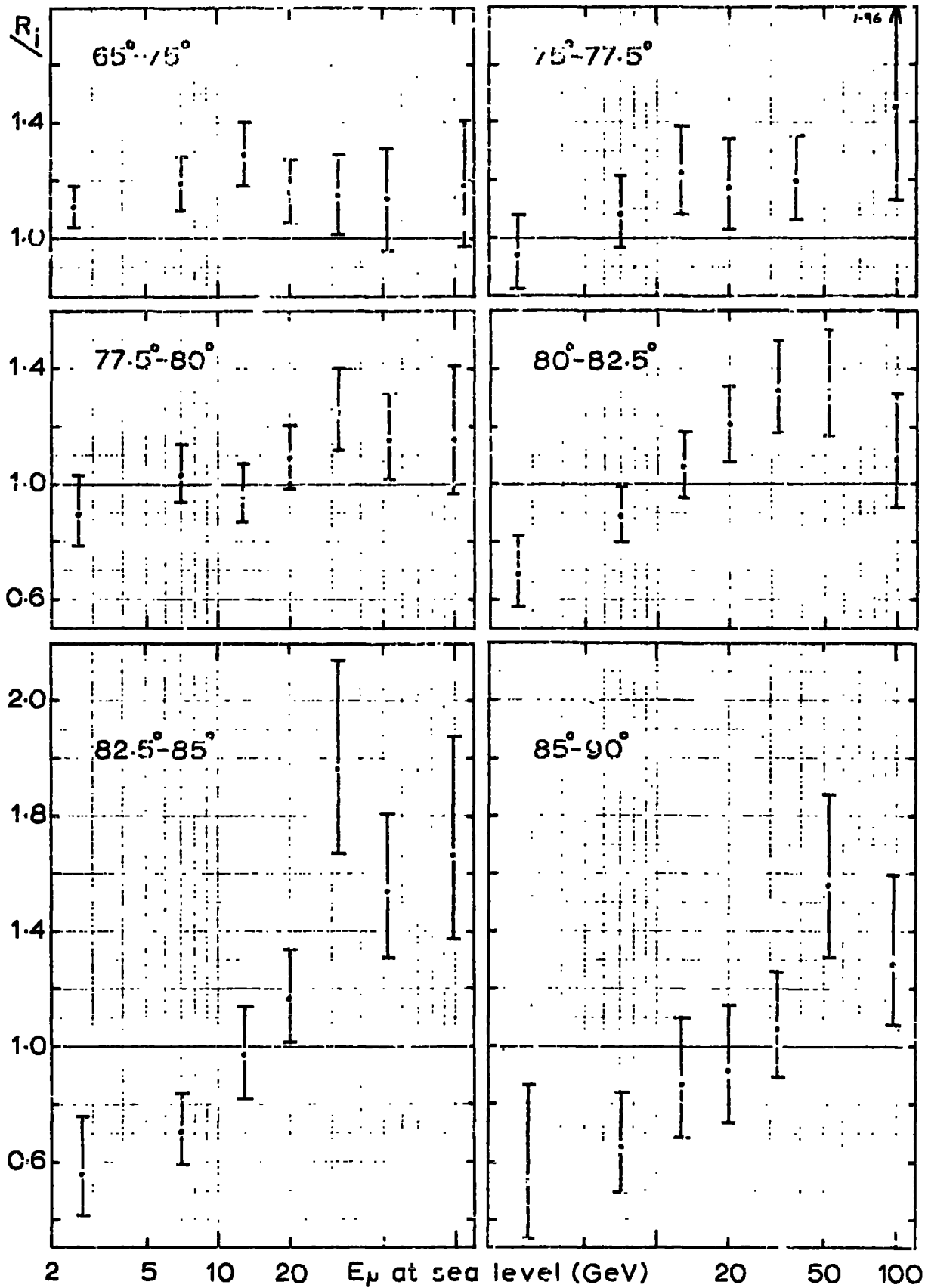
$$\delta = (N^+ - N^-)/(N^+ + N^-) \tag{6.1}$$

where the associated error σ becomes

$$\sigma = \frac{2}{(N^+ + N^-)^2} \left[(N^+.\sigma_+)^2 + (N^-.\sigma_-)^2 \right]^{\frac{1}{2}} \tag{6.2}$$

σ_+ and σ_-, the standard deviations on the positive and negative samples, N^+ and N^-, are assumed to be of Poissonian form, such that, for large N, $\sigma_\pm = (N^\pm)^{\frac{1}{2}}$. In order to take into account the asymmetry in the Poissonian errors for small N, the following artifice was used

$$\sigma_U = \frac{2}{(N^+ + N^-)^2} \left[(N^+.\sigma_{+U})^2 + (N^-.\sigma_{-L})^2 \right]^{\frac{1}{2}} \tag{6.3}$$

$$\sigma_L = \frac{2}{(N^+ + N^-)^2} \left[(N^+ \sigma_{+L})^2 + (N^- \sigma_{-U})^2 \right]^{\frac{1}{2}} \qquad (6.4)$$

the additional subscripts U and L refer to the upper and lower errors respectively. For the purposes of data combination, the statistical weight given to a particular charge excess value was either $1/\sigma_L{}^2$ or $1/\sigma_U^2$ dependent upon whether the combined charge excess value was estimated to be smaller or greater than the individual value. As this particular error treatment is only necessary when dealing with charge excess values having large associated errors, any inadequacies of the method will not be severe.

Of further significance in evaluating an incident charge ratio from the observed results, is the effect of additional fluctuations expected in the observed data through the increased number of "binomial channels" opened as a result of Coulomb scattering of the muons, c.f. Appendix B1. The effect of these fluctuations were included in the analysis by evaluating an error independent of the normal Poissonian error, the total error being taken as the errors combined in quadrature; the effect of the additional fluctuations was only important for muons arriving with energies below 10 GeV where scattering was appreciable.

In estimating the magnitude of this effect, the following approximate method was employed. During the computations on the scattering problem, as described in sect. 5.5, it was possible to assign a probability that particles arriving in each zenith cell would be scattered into a chosen zenith cell. It was then assumed that the particles arriving in the chosen zenith cell could be described as coming from a fixed source with a probability p equal to the mean of the computed probabilities associated

with each cell. The number of particles emanating from the fixed source
was taken to be $N^{\pm}/\rho$ where $N^{\pm}$ were the observed numbers of particles in
the chosen cell. The expected fluctuations followed directly from a
consideration of the associated binomial distributions. It follows from
such a description that for large N and small p the magnitude of the error
introduced through this effect tends to the value of the Poissonian error.

As mentioned in Appendix B2, this broadening in the error also becomes
of importance in the analysis of data at and beyond the m.d.m. of spectro-
graphs, but in the case of the results under consideration, the momentum
assigned to the last energy cell considered is below the m.d.m. of the present
instrument; the non-Poissonian contribution to the error was here assumed to
be negligible.

6.2. The Muon Charge Ratio at sea level after corrections for the Geomagnetic Effect.

The principles underlined in the previous section together with geo-
magnetic correction factors

$$g = (J^-/J^+) \cdot (S^-/S^+) \cdot g', \qquad (6.5).$$

as calculated in the previous chapter, were used to evaluate the charge
ratio, in each zenith and energy cell, expected for conditions of minimum
geomagnetic effect (propagation along the magnetic meridian). Fig. 6.2
shows the corrected charge ratios for the geometries at 22° and 33°
separately and for those muons arriving with zenith angles greater than
75°. The sets of data from each geometry may be considered to be
independent and so the consistency between the two sets of corrected ratios

CORRECTED CHARGE RATIO, $\theta = 75^{\circ}-90^{\circ}$. Fig. 6·2

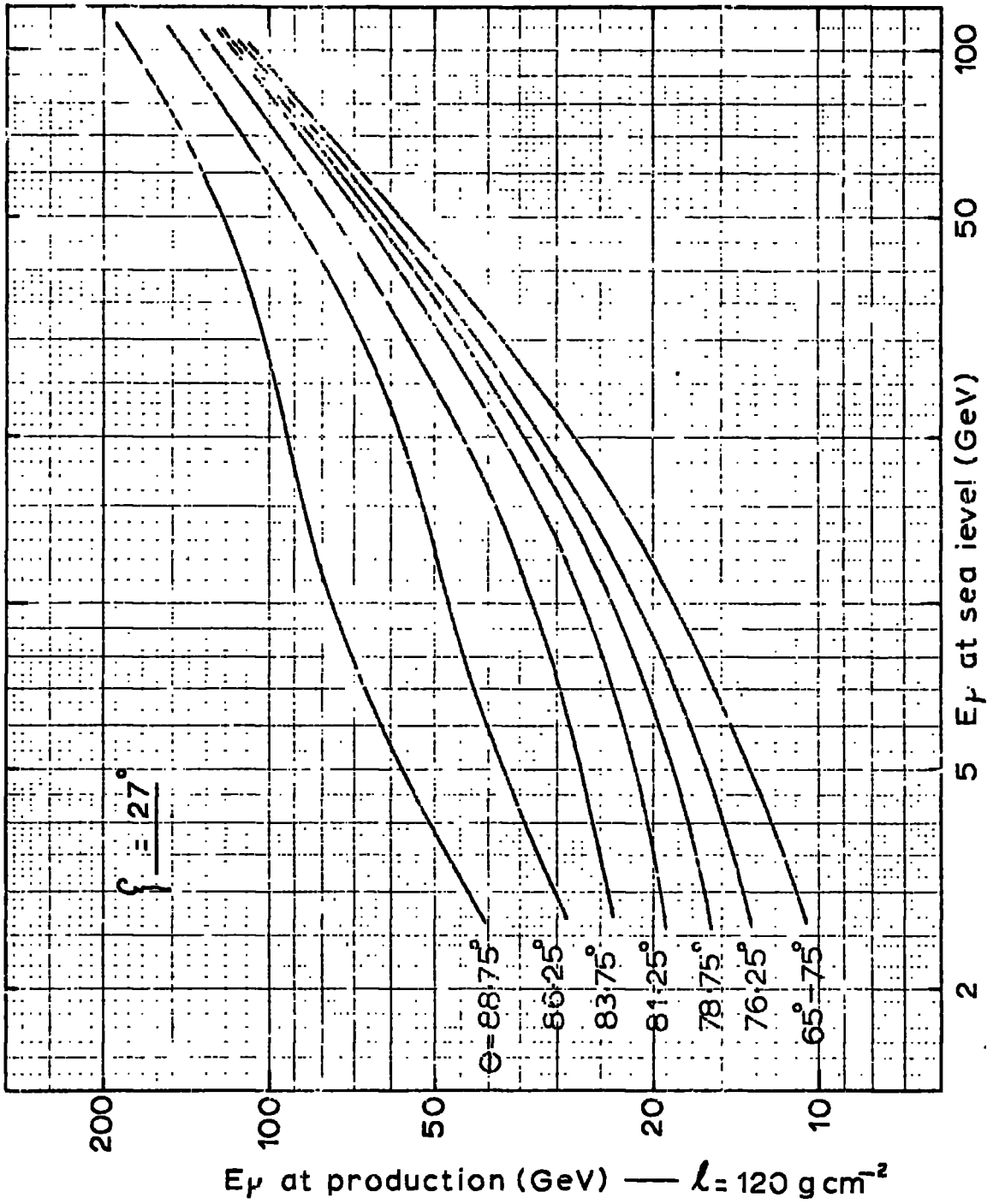CORRECTED CHARGE RATIO   Fig. 6·3
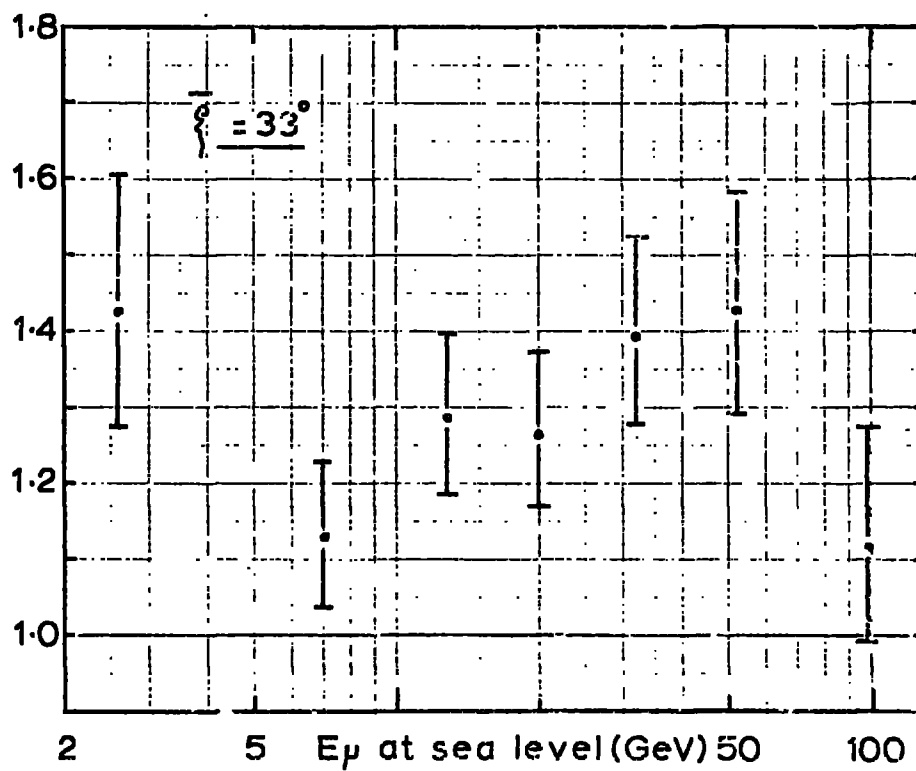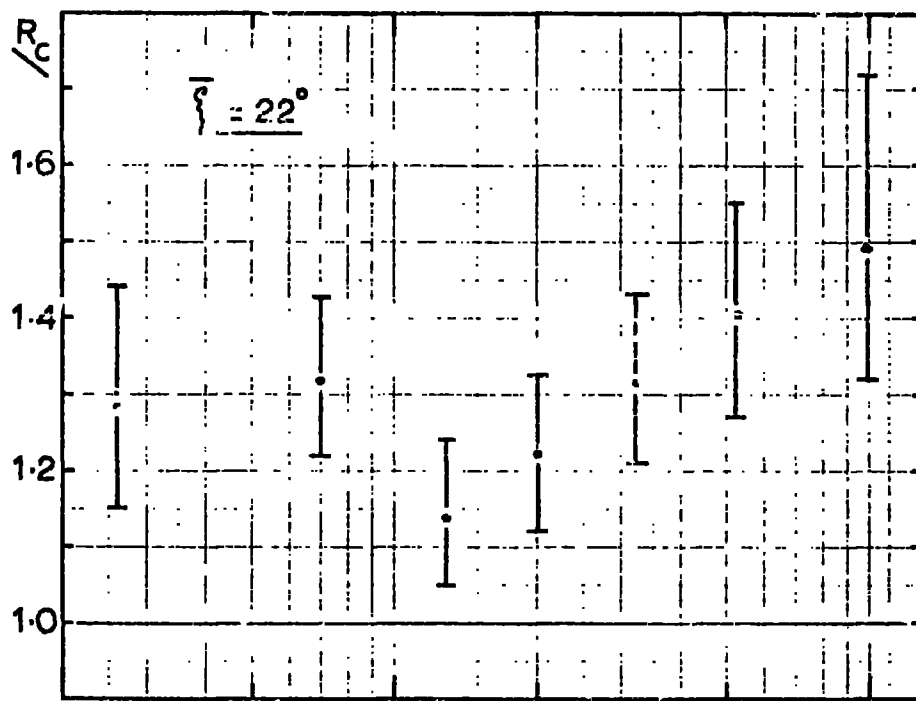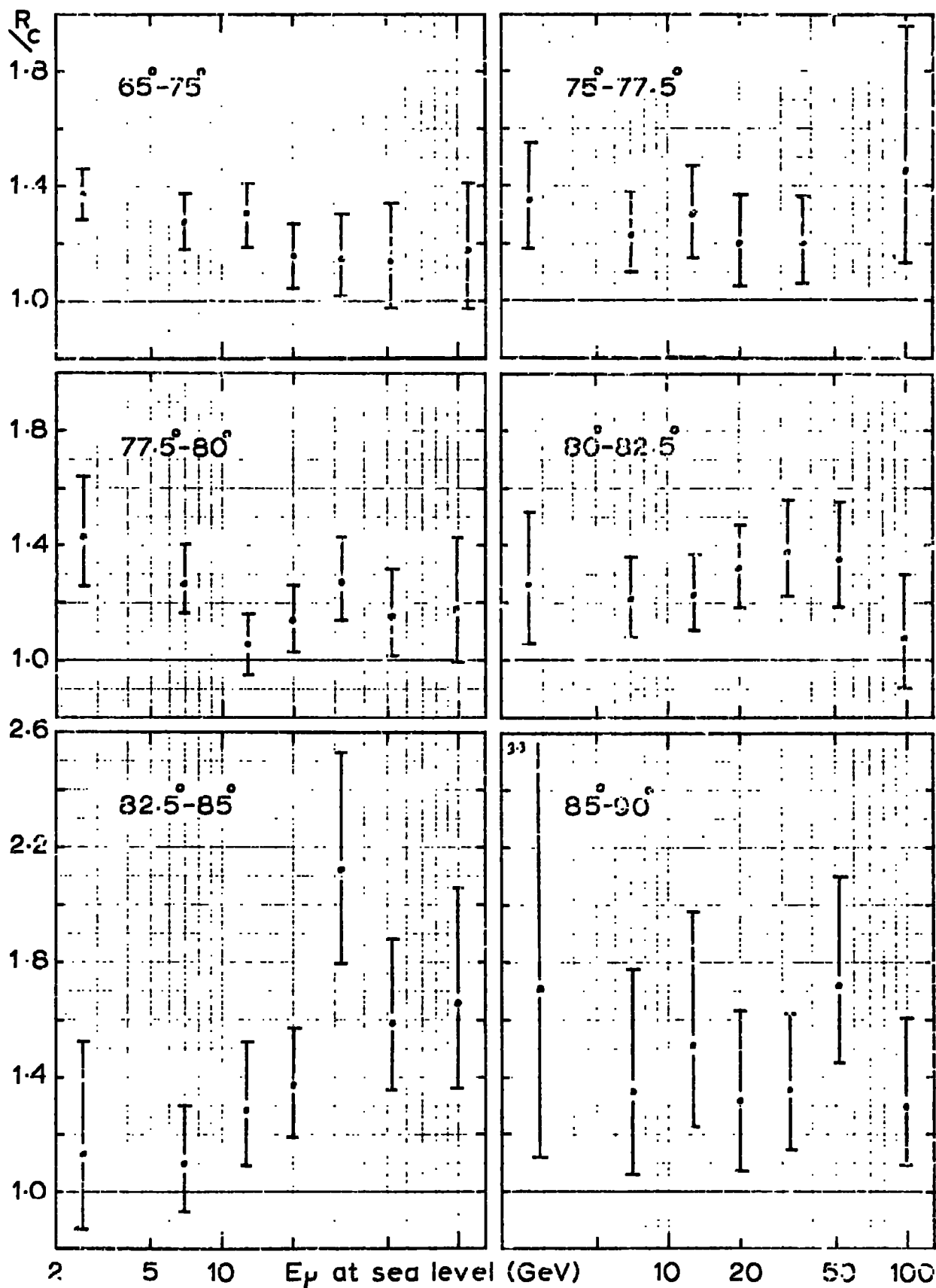
gives weight to their validity. Fig. 6.3 shows the corrected ratios after the results from the separate geometries were combined. As the corrections to be applied to the data on the muons arriving with zenith angles between 65° and 75° are small, then these results provide a reasonable datum for comparison with the corrected large angle data. The consistency between the charge ratio values observed in this zenith cell and the surveys of the charge ratio, reviewed in Chapter 1, also lend weight to the validity of the present results.

## 6.3. The Muon Charge Ratio at Production

The energy lost by muons during their passage through the atmosphere can be large and depends upon the arrival direction of the muons. Consequently the muons having the same energy on arrival at sea level, dependent on their direction of arrival, will have widely differing production energies. To gain the maximum information on any energy dependent production process it is therefore instructive to assign to each sea level ratio a corresponding production energy.

Taking into account the differences in the path lengths of the positive and negative muons arriving in each zenith and energy cell, the effective muon production energies were obtained from a consideration of such information as displayed in figs. 5.7 a,b together with the mean zenith angles of the muons prior to scattering estimated in the manner outlined in sect. 5.5. Fig. 6.4 shows the mean production energies associated with the muons detected by the present spectrograph. In fig. 6.5 , the corrected charge ratios have been plotted as a function of the muon production energy.

Mean production energy of scattered muons   Fig. 6.4

Variation of the charge ratio with prodn. energy   Fig. 6.5
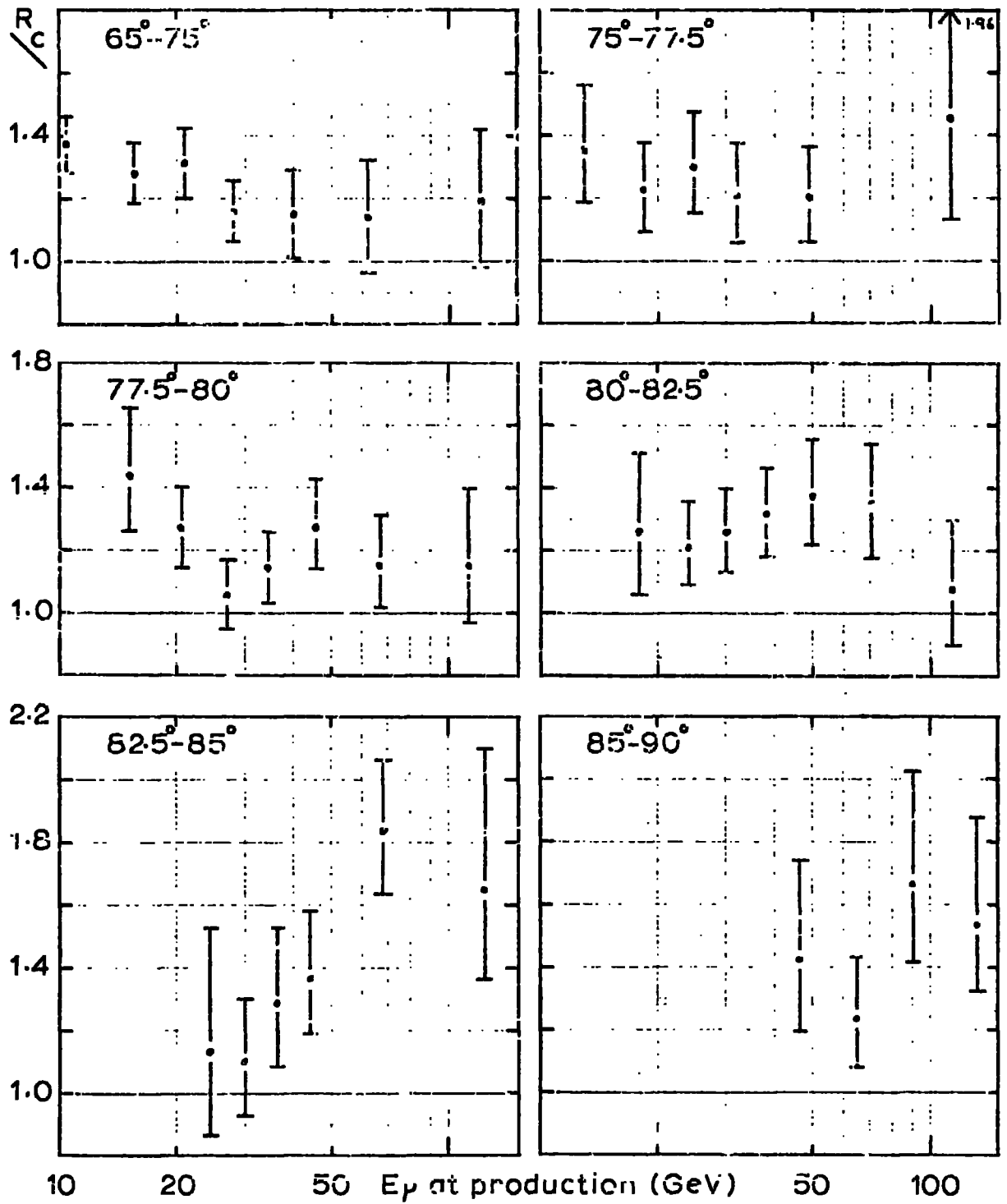
6.4. Previous Durham Results and Other Relevant Data

The previous Durham results, as corrected using factors supplied by Kamiya (sect. 5.4.1),have already been presented in fig. 1.7. Using the new correction factors, calculated in Chapter 5, the results of the Durham spectrographs have been recorrected. Due to the wider applicability of the present correction method, it has been possible to include the previously unpublished corrected charge ratio value at the lowest energy. The corrected results are presented in fig. 6.6.

The results from the Japanese experiment, Kamiya et al. (1969)., are of particular relevance to the present study as in this experiment the arrival directions of the muons in the zenith were recorded so allowing a subdivision of the data into zenith cells; the spectrograph was aligned along the magnetic meridian.

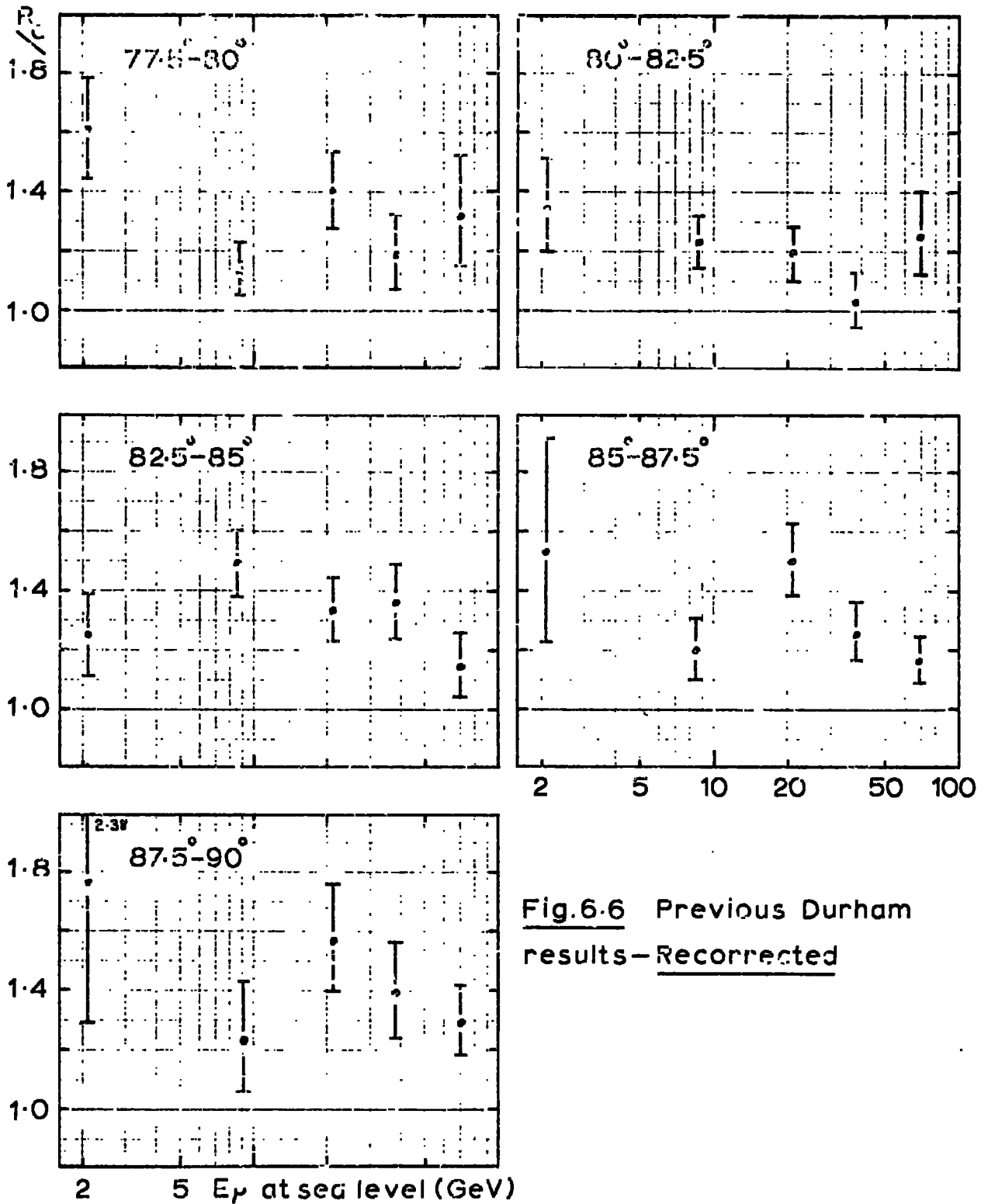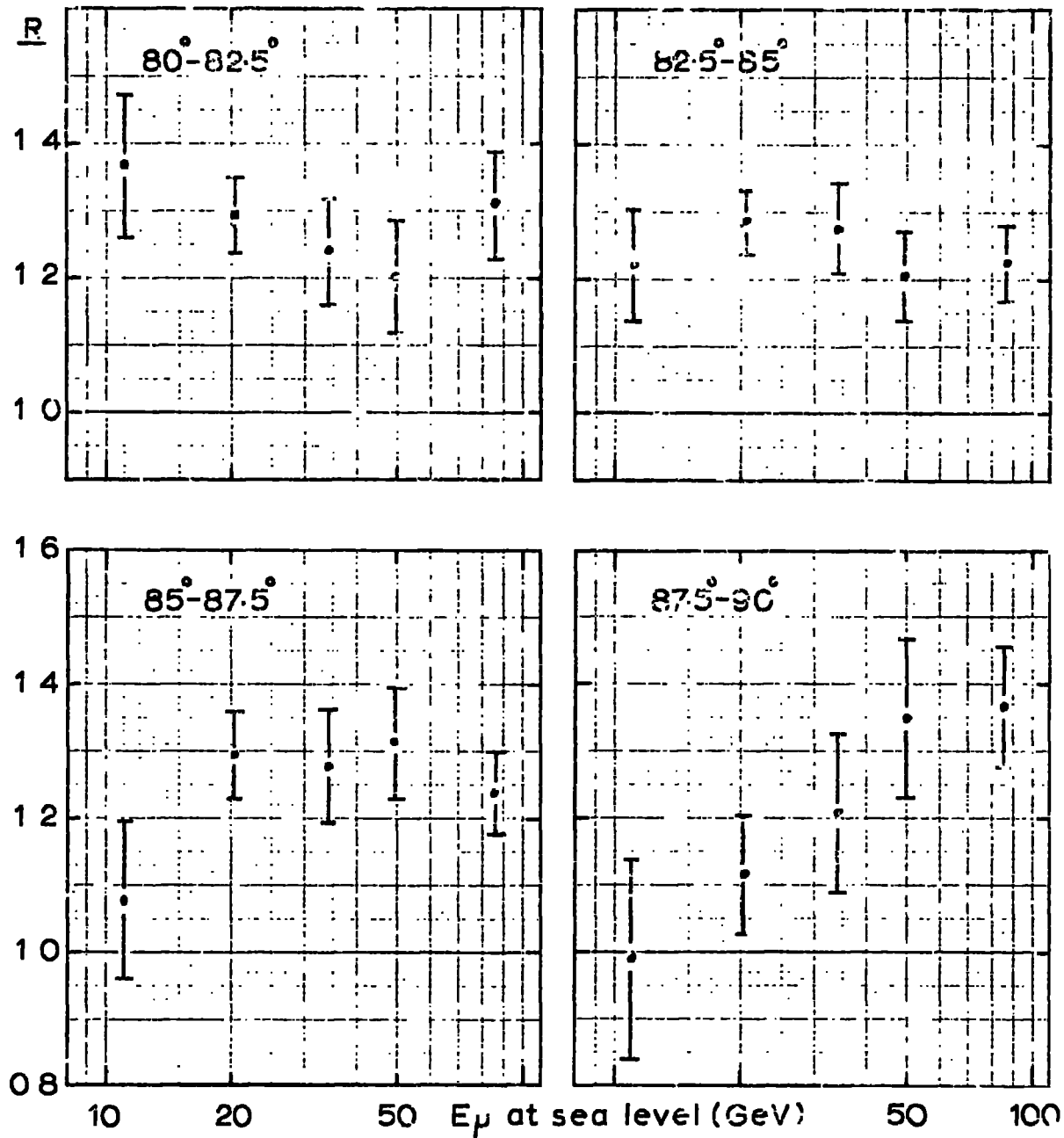Those results of this experiment pertaining to muon sea level energies < 100 GeV are reproduced in fig. 6.7.

Fig.6·6 Previous Durham results — Recorrected

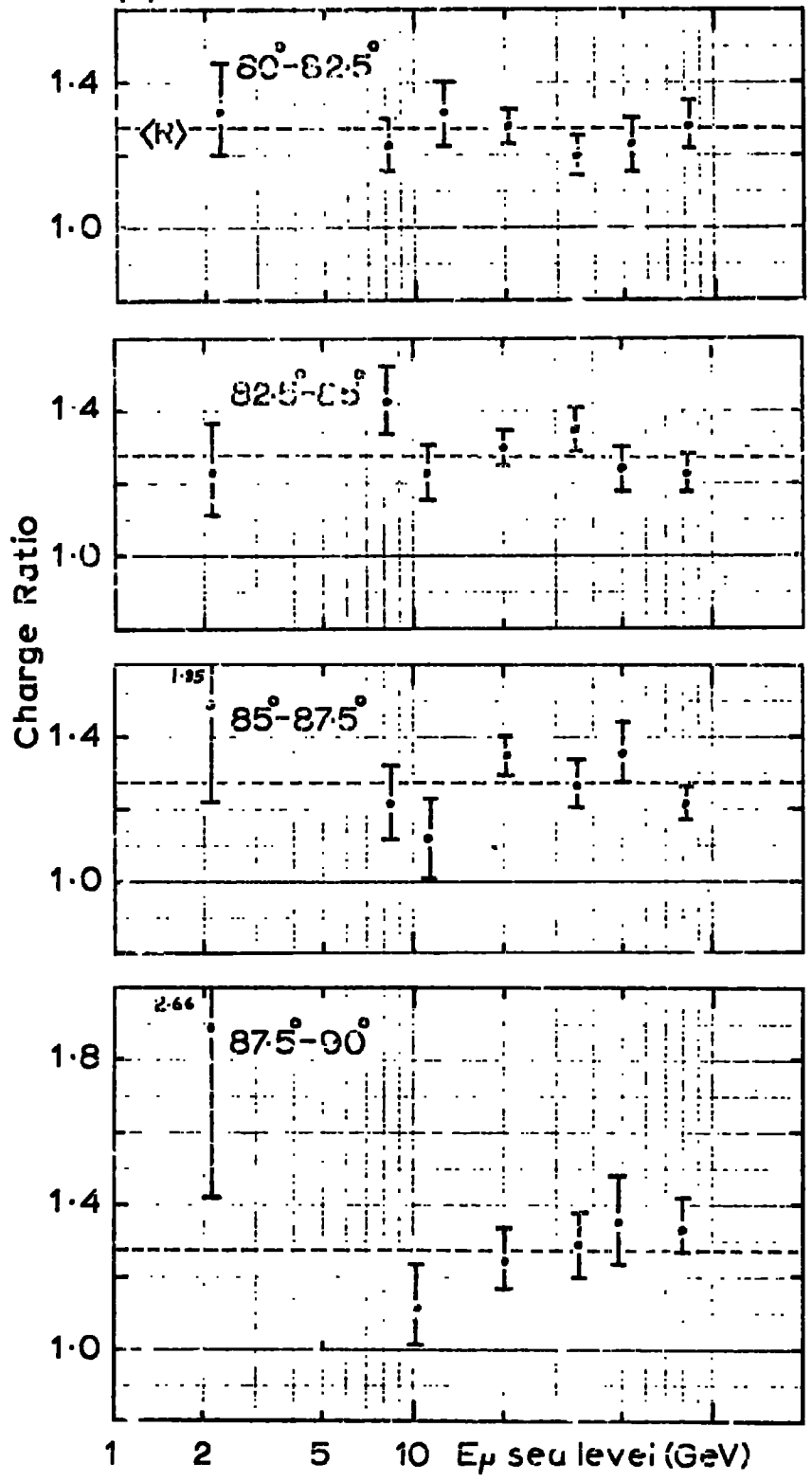MUON CHARGE RATIO — Kamiya et al. (1969)   Fig. 6·7

CHAPTER 7

DISCUSSIONS   AND   CONCLUSIONS

7.1.   Fine Structure in the Muon Charge Ratio

It is now possible to proceed with a comparison of the three sets of
experimental data on the muon charge ratio displayed in figs. 6.3, 6.6 and
6.7, the Durham results having been normalized to the operational conditions
similar to those encountered in the Japanese experiment (spectrograph axis
parallel to the magnetic meridian). As it was the peaking at 20 GeV in the
muon charge ratio as measured by the previous Durham spectrographs which
initiated the present investigations, the possibility of such a peaking
must be given first consideration. Clearly, both the results from the
present experiment and those from the Japanese experiment do not provide
supporting evidence for such a peaking in the charge ratio. Indeed, the
results from each experiment when combined, c.f. fig. 7.1, indicate a
continued constancy in the charge ratio for zenith angles greater than
80° over the whole range of energies considered.

Although in consideration of the combined results, it is tempting
to dismiss the observed peaking in the previous Durham results as merely
statistical in origin, there does remain the possibility that the peaking
was a consequence of some geomagnetic effect hitherto unaccounted for.
Support for such an effect comes from the high values of the charge ratio
observed in the present experiment for muons arriving at sea level in the
energy range 25-70 GeV, in particular those muons falling in the zenith
cell 82.5^o - 85°. If there does exist a geomagnetic effect, causing a
peaking at 20 GeV for the previous Durham experiment, then it might be

Combined data—$E_\mu < 150$ GeV   Fig. 7·1

$\langle R \rangle = 1·275$

60°-62·5°

82·5°-85°

85°-87·5°

87·5-90°

Charge Ratio

E_μ sea level (GeV)

expected that for different arrival directions in the azimuthal plane, but in the same zenith cell, a peaking would occur at energies where g_s, the computed geomagnetic correction factors, have similar values. In the case of the present experiment - the axis being inclined at 27° East of the geomagnetic meridian - for those muons arriving in the zenith cell 82.5^O- 85° the corresponding energy where peaking might be expected is 40 GeV.

It must be noted that at those energies where the results do indicate a peaking, the geomagnetic correction factors used were small. Also, as the previous Durham results as corrected by Kamiya, fig. 1.7, and as corrected in the present analysis, fig. 6.6., are consistent, an internal accuracy in the independent computations is indicated. Therefore, in view of the possibility of an azimuthal effect associated with the geomagnetic deflection of muons, some further examinations of the assumptions used in calculating the geomagnetic correction factors follow.

7.2. Further Considerations on the Geomagnetic Effect.

7.2.1 The Dilution Effect

For muon propagation without magnetic deflection, the dilution effect on the muon charge ratio of those muons produced other than in first generation collisions has been considered by such authors as MacKeown and Wolfendale (1966) and Pal and Peters (1964). The dilution effect arises from charge exchange in nucleon collisions. The results of these authors indicate that for zenith angles greater than 80°, and at the energies of interest, a charge ratio at sea level of 1.26 would correspond to a value of the charge ratio of the muons produced in first

generation collisions in excess of 1.5.

Any process which would act so as to reduce the effect of dilution would result in a corresponding increase in the observed charge ratio, but in the context of an azimuthal variation any modulation must arise from the differences in the path lengths of the positive and negative muons. For the purposes of investigating the consequences of geomagnetic deflections on the dilution effect, the number of those muons produced in first generation collisions relative to the number produced in all collisions, and which survive to sea level, was estimated through the relation.

$$G(E,\theta) = \frac{\sum_{m=1}^{5}\left((E_{(m)})^{-2.65}.SP_{(m)}.D_{(m)}.\exp(-m/80).\frac{1}{3}m(l)\right)}{\sum_{l=1}^{\infty}\left((E_{(m)})^{-2.65}.SP_{(m)}.D_{(m)}.\exp(-m/12.).\frac{1}{3}m(l)\right)} \tag{7.1}$$

where $m(1) = 30.(2)^{-1}$, the notation being as described for equ. (5.37). The summations of equ. (7.1) were carried out along positive muon trajectories and negative muon trajectories with $\zeta = 27^{\circ}$, the corresponding values of G were denoted by G^{+} and G^{-} respectively. The summation were also carried out along undeflected muon trajectories resulting in a value G°.

The computed values of G are presented in table 7.1. Implicit in equ. (7.1) is that the charge pion production spectra are the same for all generation collisions but as this can not be the case, G^{+} must be an underestimate and G^{-} an overestimate of the relative numbers of first generation muons surviving to sea level, so reducing further any significance in the differences observed in the values G^{+}, G^{-} and G°. Clearly the dilution effect is insensitive to geomagnetic deflection of the muons in the atmosphere. Further, as can be seen from fig. 7.2, in which G° has been plotted as a function of sea level energy for a number of zenith
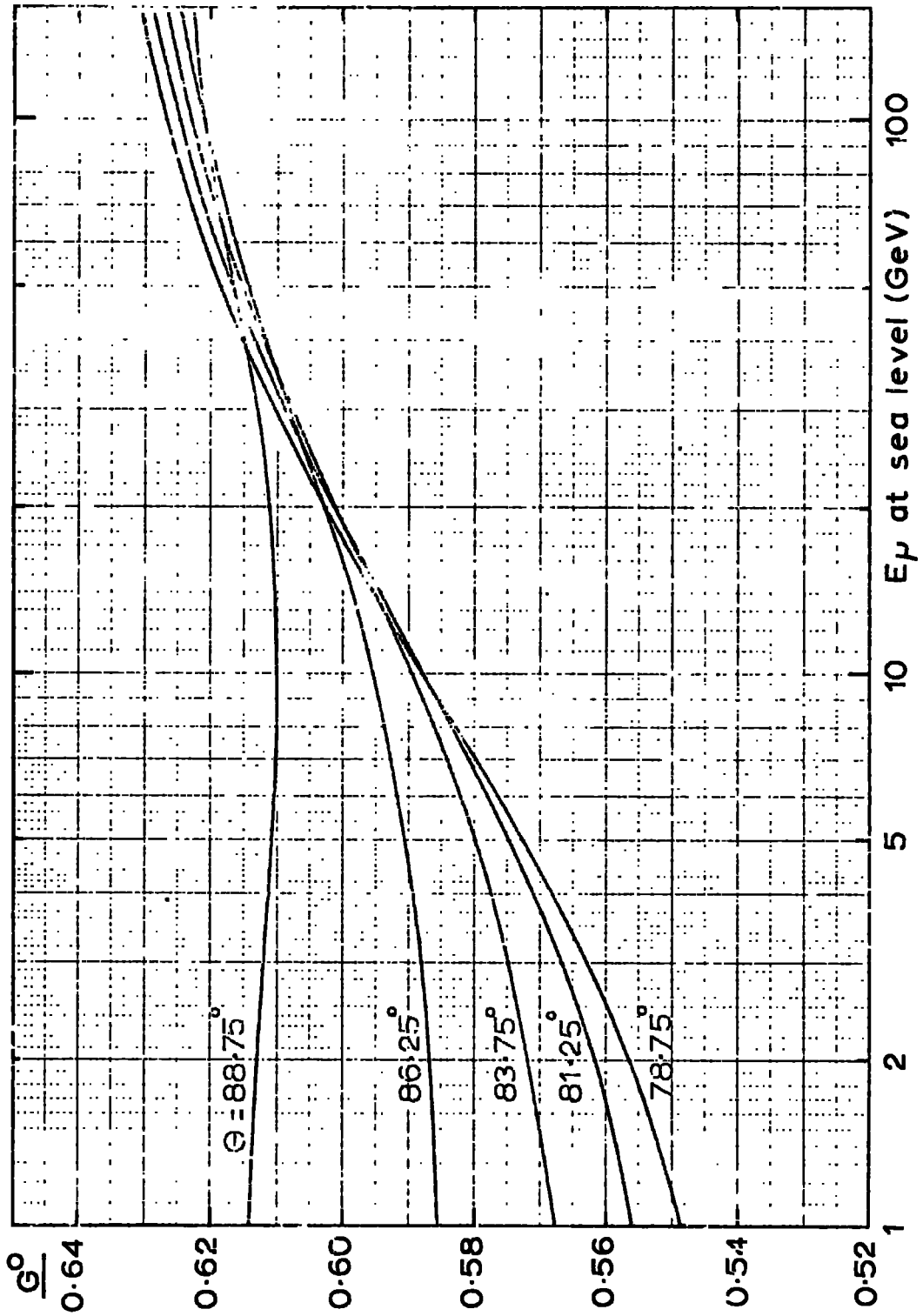
TABLE 7.1.

Fraction of muons arising from first generation interactions - G^{+}_{0}.

Zenith angle (degrees)	Charge	Sea Level Energy (GeV)			
		2	8	32	128
	−	0.605	0.610	0.615	0.622
88.75	o	0.613	0.610	0.613	0.622
	+	0.617	0.606	0.608	0.621
	−	0.587	0.597	0.610	0.623
86.25	o	0.587	0.594	0.609	0.623
	+	0.577	0.584	0.605	0.623
	−	0.575	0.590	0.609	0.625
83.75	o	0.572	0.586	0.609	0.625
	+	0.556	0.579	0.607	0.625
	−	0.567	0.586	0.610	0.627
81.25	o	0.562	0.584	0.610	0.627
	+	0.549	0.578	0.610	0.627
	−	0.557	0.585	0.614	0.629
76.25	o	0.552	0.583	0.614	0.630
	+	0.544	0.582	0.614	0.630

arrival directions, any zenith dependence of the charge ratio arising from the dilution effect is small.

7.2.2. Energy loss variations

The dominant term in the geomagnetic correction factor is g', equ. (5.37). In calculating g' it was assumed that both positive and negative muons lose energy through identical processes. Due to the strong energy dependence of g' entering through the term $E^{-2.65}$, even small differences in the behaviour of the muons would be expected to result in significant modulations of the observed charge ratio.

In estimating the variations in the observed charge ratio as expected from a difference in the behaviour of positive and negative muons, values of g' were calculated for $\zeta = 27^{\circ}E$ setting the energy loss of the negative muons 10% higher than that for positive muons. Denoting these new values of the correction term by g_e', then

$$R_e = (g'/g_e'). R \qquad (7.2)$$

gives a reasonable estimate of the enhanced corrected ratios which would arise from applying a correction factor including the term g'. In fig. 7.3, values of R_e are plotted for R set equal to 1.25. The dotted lines show the effect of including a lower cut-off such that the muons were considered to behave normally for energies less than 40 GeV.

By considering the calculated values of R_e, presented in fig. 7.3, the following are apparent:-

   a) the effect remains significant for zenith angles 80° and less, contrary to the experimental observations;

Enhanced Charge Ratio, $(d\bar{E}/dx)/(dE^+/dx) = 1.1$

Fig. 7.3
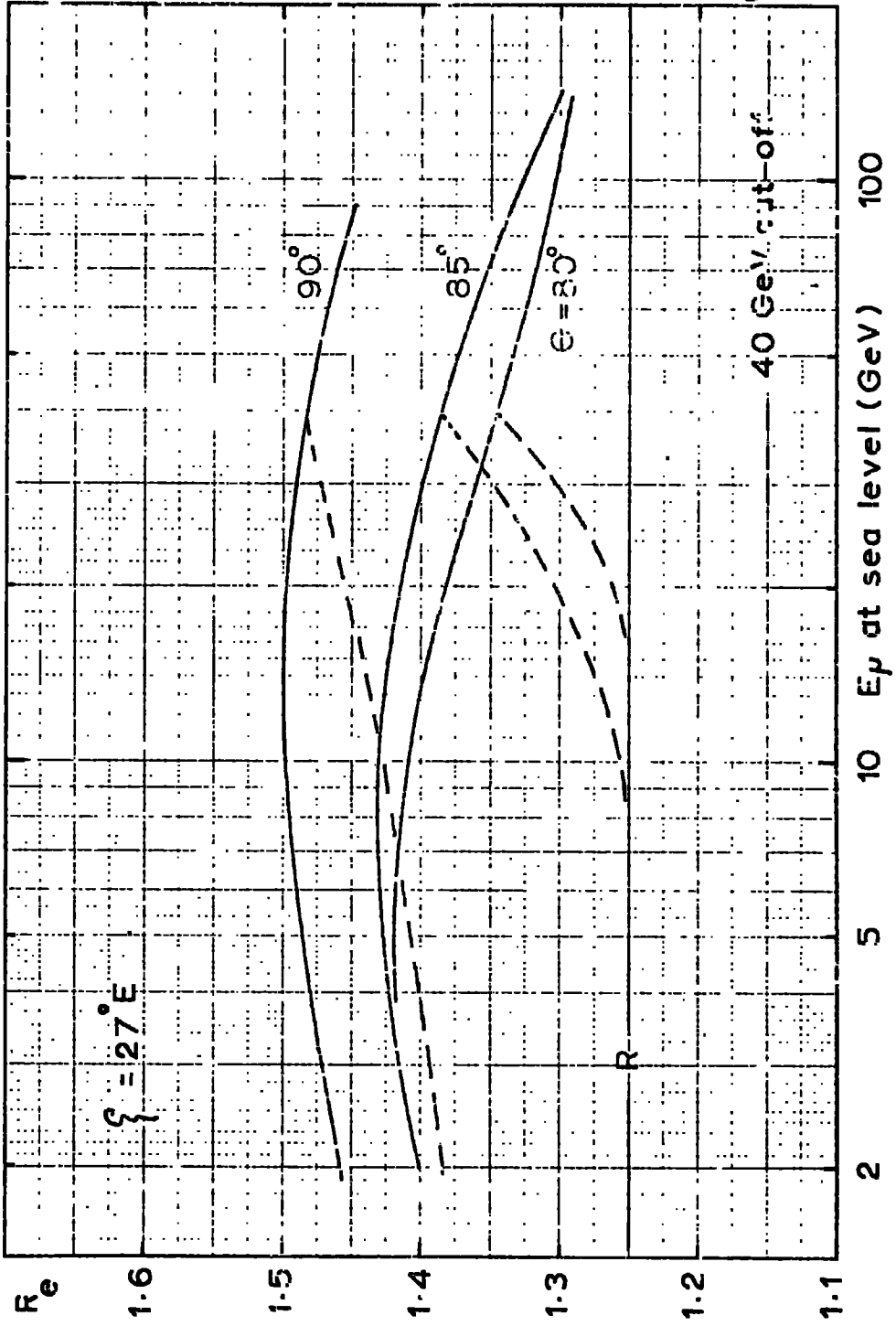
b) to produce an actual peak in R_e it was necessary to invoke a cut-off at 40 GeV, precluding any azimuthal dependence of the position of the peak.

In view of the above facts, as an explanation of the apparent fine structure in the muon charge ratio, differences in the behaviour of positive and negative muons may be ruled out without any further considerations.

7.2.3. Cell Width Factor

The cell width factor, due to it having a value less than unity, deserves some further consideration. It's contribution to the geomagnetic correction factor for the present experiment, computed in the manner outlined in sect. 5.4.4 was found to be less than 4% at 40 GeV, but an underestimate of its contribution would result in apparent high values in the corrected charge ratios.

For the purposes of the geomagnetic correction, the cell width factor was evaluated using the following approximations.

1) Coulomb scattering of the muons passing through the atmosphere was considered to affect only the final arrival direction of the muons and not the individual terms of the Jacobian.

2) Muons were assumed to be propagated in a non turbulent atmosphere as outlined in sect. 5.2.

3) Lateral trajectory displacements, displacement along the vector $\bar{w}$ - sect. 5.4.4, were considered to be unimportant.

Of the above assumptions, the first is perhaps the most likely source of error. At those energies where peaking occurs, angular scattering is small,

but as the scattering at these energies must be considered to occur through-
out the atmosphere, the resultant displacements are expected to be very much
larger than the dimensions of the spectrograph. It is not clear how this
would effect the terms of the Jacobian; an evaluation of the effect would
be best approached through an extensive computer simulation of muon
propagation through the atmosphere including scattering as well as
geomagnetic deflections. Because of the extent of the computations
required in the solution of such a problem, the possible azimuthal effect
needs substantiation with further measurements of the charge ratio of muons
with arrival directions off the magnetic meridian before a solution becomes
worthwhile.

7.3. Conclusions

In conclusion, if there does exist a peaking in the muon sea level
charge ratio, the position of the peak depending upon the muon arrival
direction in the azimuthal plane and independent of the zenith arrival
direction, then explanation through new particle production or anomalous
behaviour of the muons must be ruled out. This would appear to leave
as the only possible explanation a geometrical effect as discussed in
the previous section but detailed investigation of such a possibility
must await verification of the existence of the fine structure - (the
new Durham spectrograph described by Ayre et al. (1969), currently being
constructed, is expected to provide precise measurements of the muon
charge ratio at large zenith angles in   two years time - it is
proposed that the axis of the spectrograph shall lie along a line 27°

East of the magnetic meridian. However, whether in fact there does exist an azimuthal effect or the structures are of purely statistical origin, the results indicate that those muons arriving at sea level with energies $<$ 150 GeV are produced as a result of high energy nucleon interaction in the upper atmosphere with interaction characteristics consistent with those of the models outlined in sect. 1.3.

Collecting together the available charge ratio values the present work shows -

a) The measured charge ratio of muons at sea level varied between 0.65 and 1.4 (see figure 4.1), b) the corrections to the charge ratio indicated that the sea level charge ratio is in the range 1.15 to 1.45 (see figure 6.2) and c) that on converting the muon energies at sea level to the production energy, the charge ratio lies in the range 1.1 - 1.65 (see figure 6.5).

REFERENCES

Alexander, D., Holyoak, B., Thompson, M.G., Turner, M.J.L., (1968a), Proc. Int. Conf. Cosmic Rays, Canada; Can. J. Phys., 46, S273.

Alexander, D., Pathak, K.M., Thompson, M.G., (1968b), J. Phys. A, Proc. Phys. Soc., 1, 578.

Alexander, D., Thompson, M.G., Turner, M.J.L., Wolfendale, A.W., (1969a), Proc. Int. Conf. Cosmic Rays, Hungary. (In Press).

Alexander, D., Thompson, M.G., (1969), Proc. Int. Conf. Cosmic Rays, Hungary. (2 papers- in press).

Allen, J.E., Apostolakis, A.J., (1961), Proc. Roy. Soc., A265, 117.

Ashton, F., Coats, R.B., Holyoak, B., Simpson, D.A., Thompson, M.G., (1965), Nuc. Inst. and Methods, 37, 181.

Aurela, A.M., MacKeown, P.K., Wolfendale, A.W., (1966), Proc. Phys, Soc., 89, 401.

Ayre, C.A., Breare, J.M., Holroyd, F.W., Thompson, G.M., Wells, S.C., Wolfendale, A.W., (1969), Proc. Int. Conf. Cosmic Rays. Hungary. (In press).

Barrett, P.H., Bollinger, L.M., Cocconi, C., Eisenberg, Y., Greisen, K., (1952), Rev. Mod. Phys. 24, 133.

Bergeson, H.E., Keuffel, J.W., Larson, M.O., Martin, E.R., Mason, G.W., Stenerson, R.D., (1968), Proc. Int. Conf. Cosmic Rays, Calgary; Can. J. Phys., 46, S399.

Cocconi, G., (1965), Proc. Conf. Cosmic Rays, London; Inst. Phys. and Phys. Soc., 2, 616.

Coxell, H., (1961), Ph.D. Thesis, Univ. of Durham.

Dekkers, D., Geibel, J.A., Mermod, R., Weber, G., Willits, T.R., Winter, K., Jordan, R., Vivargent, M., King, N.M., Wilson, E.J.N., (1965), Phys. Rev., 137B, 962.

Earnshaw, J.C., Orford, K.J., Rochester, G.D., Somogyi, A.J., Turver, K.E., Walton, A.B., (1967), Proc. Phys. Soc., 90, 91

Flint, R.W., Nash, W.F., (1969), Proc. Int. Conf. Cosmic Rays, Hungary. (In press).

(1970), Proc. Conf. Cosmic Rays, La Paz.

Fowler, G.N., Wolfendale, A.W., (1961), Handb. der Physik, 46, 272.

Fowler, P.H., Adams, R.A., Cowen, V.G., Kidd, J.M., (1967), Proc. Roy. Soc. (London), A, 301, 39.

Greissen, K., (1965), Proc. Int. Conf. Cosmic Rays, London; Inst. Phys. and Phys. Soc., 2, 609.

Greissen, K., (1966), Phys. Rev. Lett., 16, 748.

Jones, I.S., Pathak, K.M., Thompson, M.G., (1968), J. Phys. A, Proc. Phys. Soc. (Gen), 1, 584.

Kamiya, Y., Kawaguchi, S., Fujii, Z., Iida, S., Mitsui, K., (1969), Proc. Int. Conf. Cosmic Rays, Hungary, (In press).

Kelly, G.N., MacKeown, P.K., Said, S.S., Wolfendale, A.W., (1968), Proc. Int. Conf. Cosmic Rays, Canada; Can. J. Phys., 46, S309; S365.

Koshiba, M., (1967), Proc. Int. Conf. Cosmic Rays, Canada, A, 525.

Koshiba, M., Nozaki, T., Totsuka, T., Yamada, S., (1968), Proc. Int. Conf. Cosmic Rays, Canada; Can. J. Phys. 46, S671.

Lloyd, J.L., Wolfendale, A.W., (1955), Proc. Phys. Soc. A., 68, 1045.

Liland, A., Pilkuhn, H., (1969), Proc. Int. Conf. Cosmic Rays, Hungary. (In press).

Linsley, J., (1962), Phys. Rev. Lett., 9, 126.

Linsley, J., (1963), Phys. Rev. Lett., 10, 146.

MacKeown, P.K., (1965), Ph. D. Thesis, Univ. of Durham.

MacKeown, P.K., Wolfendale, A.W., (1966), Proc. Phys. Soc., 89, 553.

Maeda, K., (1960), Journ. of Atmos. and Terr. Phys., 19, 184 (1964), Journ. of Geophys. Res., 69, 1725.

Matano, T., et al., (1968), Proc. Int. Conf. Cosmic Rays, Canada; Can. J. Phys., 46, S56.

McCusker, C.B.A., (1967), Proc. Int. Conf. Cosmic Rays, Canada, A, 397.

Miyake, S., Hinotani, K., Ito, N., Kino, S., Sasaki, H., Yoshii, H., Sakuyama, H., Kato, E., (1968), Proc. Int. Conf. Cosmic Rays, Canada; Can. J. Phys., 46, S25.

Okuda, H., (1963), Proc. Cosmic Ray Lab., Nagoya Univ., 10, 1.

Osborne, J.L., (1966), Ph. D.Thesis, Univ. of Durham.

Pal, Y., Peters, B., (1964), Mat. Fys. Medd. Dan. Vid. Selsk., $\underline{33}$, No. 15.

Parker, J.H., (1969), Ph.D. Thesis, Univ. of Utah.

Pattison, J.B.M., (1963), M.Sc. Thesis, Univ. of Durham.

Puppi, G., Dallaporta, N., (1952), Prog. in. Elem. Part. and Cosmic
        Ray Phys., $\underline{1}$, 317.

Reid, R.J., Gopanlsingh, K., Page, D.E., Idnurm, M., McCusker, C.B.A.,
        Malos, J., Millar, D.D., Winterton, G., (1961), Proc. Phys.
        Soc., $\underline{78}$, 103.

Smith, J.A., Duller, N.M., (1959), J. Geophys. Res., $\underline{64}$, 2297.

Wolfendale, A.W., (1969), Proc. Int. Conf. Cosmic Rays, Hungary. (In
        press).

Zatsepin, G.T., Kuzmin, V.A., (1961), Zhurn. Eksp. Teur. Fiz., $\underline{39}$,
        1677; Sov. Phys. JETP, $\underline{12}$, 171.

APPENDIX A

THE ANOMALOUS INCREASE IN THE ENERGY LOSS OF RELATIVISTIC PARTICLES?

A.1. Introduction

Organic plastic scintillators such as Ne 102a, manufactured by Nuclear Enterprises (GB) Ltd., are widely used in cosmic radiation studies. The most common application of the material is in the determination of the density of coincident highly relativistic particles at certain locations. In determining the particle density, a knowledge of the most probable energy deposited in the phosphor by a highly relativistic particle is required and this is further assumed to be constant for all relativistic velocities. This assumption is justified by Sterheimer (1952, 1953a and b, 1956, 1967) and other theorists who predict that due to the density effect the energy loss is sensibly constant for $\gamma \geqslant 10$. The results of Smith and Stewart (1966), however, indicate that for electrons, the most probable energy loss is not constant for $50 < \gamma < 300$, but increases by $(11.4 \pm 1.0)\%$ over this range. The results of other workers on this same material, Crispin and Hayman (1964) and Jones et al. (1968) also indicate a similar rise in the energy loss of muons over the same range of γ, but the results of the latter workers are very sparse over the region of interest and do not themselves justify the anomalous results of Smith and Stewart. Nevertheless, the three results together indicated that a further experiment was necessary, particularly over the range $50 < \gamma < 500$. Accordingly, the passage of cosmic ray muons in the momentum range 5 - 50 GeV/c, through Ne 102a phosphor has been reinvestigated; the experimental

description and results follow.

A.2. Experimental Details

The phosphor used in the investigation was that of the scintillation counter S1, described in sect. 2.2. The outputs from the counter's two photomultipliers were added and passed to a 400 channel, pulse height analyser; the analyser gate was opened by the spectrograph's coincidence pulse. The pulse height was displayed as a spot on a display screen; the spot was held in position for a few seconds after the occurrence of each event. A camera system was set up such that the pulse height was recorded as a line drawn on a moving film. The time and run number were recorded for each event, and at every tenth event, neon indicators, situated both on the spectrograph and on the analyser, were illuminated to ensure accurate matching of the spectrograph and analyser films during the subsequent film analysis.

Using the above method, the measurements of the pulse heights from the detector were free from the subjective errors frequently encountered when pulse heights are determined from photographic records of oscilloscope traces. Further, by using cosmic ray muons, all momenta were sampled randomly and continuously so eliminating any experimental error due to a drift of the gain of the detector or its associated electronics.

The response variation across the counter was found to be well represented by the relation

$$y = 52 + 0.075.|x| + 0.035.x^2 ; \qquad\qquad (A.1)$$

x was measured in centimetres from a point 2 centimetres East of the counter's centre. In the final data analysis, this response variation

was allowed for. Allowance was also made for the extra thickness of
scintillation material traversed by those muons arriving obliquely.

A.3. Data Analysis

The pulse height distributions obtained for the various ranges of
muon momenta, given in table 1, were skewed distributions. The method
adopted to determine the mode of the distributions was that as described
by Bowen (1954). In the present work the theoretical curve required
for the analysis was taken as the master histogram obtained by adding
all the data into a single histogram, which is shown in figure 1. The
ratio of the areas on either side of the mode of the master histogram
was assessed and this then applied to the individual histograms using
1% cut-offs of the tails of the distributions. The modes of the
distributions were also estimated using a least squares fit of the
master distribution to each histogram, cut-offs of 15% were applied, and
these results were in sensible agreement with those obtained using the
Bowen method of analysis. The statistics of the individual distributions
and the modes calculated using the Bowen method are given in table 1;
the modes are also plotted in figure 2.

A.4. Discussion and Conclusions

To each of the sets of results of the previous workers, collected
together in figure 3, a weighted least squares fit of the points to a
straight line in the region of interest was made, yielding values for
the slopes of the lines as follows: Smith and Stewart (1966) (11.4 ± 1.0)%,

Crispin and Hayman (1964) (10.8 ± 0.6)% and Jones et al. (1968)(11.5 ± 1.4)%.
These three sets of experimental results were normalised so that the best
straight lines, obtained as described above, intersected at a γ value of
140. The slope of a similar best fit line to the present data, namely
(3.07 ± 2.65)%, was much less than those of the previous experiments. Two
points concerning the present analysis must however be made. Firstly,
any real divergence of the slope of the suggested straight line from zero
is minimised by the method of analysis and secondly, the uncertainties
attached to the estimates of the gradients of each of the lines are
underestimates because no account has been taken of the uncertainties
on the individual points of figure 3.

The data from the present experiment were also analysed by the χ^2
method. In this treatment the following question was asked. What were
the respective likelyhoods that the present results had arisen as a
consequence of the following:

a) a straight line relationship between the energy loss and the
   logarithm of the muon momentum, the energy loss increasing
   by 11% over the range, or

b) the energy loss being energy independent?

The likelyhood of (a) was found to be 0.35% whereas, the likelyhood
of (b) was found to be 72%.

It is therefore concluded that, although the energy loss of the
muons in the last energy cell considered was high, the present results
point to a behaviour of the muon as predicted by the Sternheimer theory.

TABLE 1

Distribution of the events in the momentum cells

Momentum range of cell (GeV/c)	Mean momentum of cell (GeV/c)	Number of particles in cell	Mode of Distribution
4.0 - 7.0	5.3	267	21.86 ± 0.37
7.0 - 10.7	8.7	241	21.73 ± 0.39
10.7 - 15.7	13.0	282	21.58 ± 0.37
15.7 - 21.5	18.4	221	21.58 ± 0.41
21.5 - 31.6	26.1	300	21.71 ± 0.37
31.6 - 50.0	40.0	278	22.74 ± 0.39
50.0 - 100	77.0	267	22.40 ± 0.40

A PULSE HEIGHT RECORD
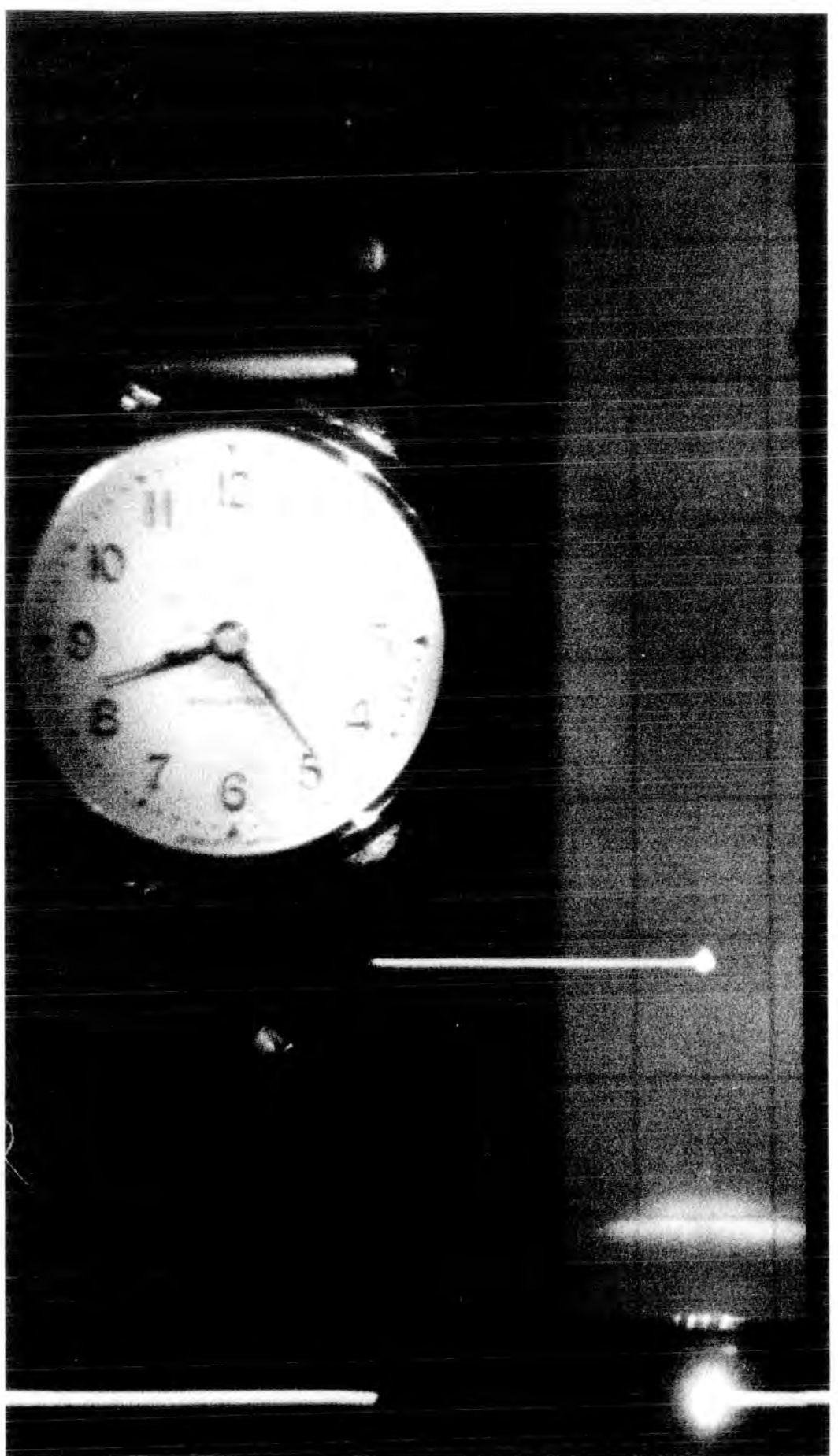
Captions to Figures

Figure 1.   Pulse height spectrum for all muons for which

        $50 \leqslant \gamma \leqslant 500$, in Ne 102a.

Figure 2   Variation of the most probable energy loss of

        muons in Ne 102a with muon momentum.

Figure 3.   Variation of the most probable energy loss in

        Ne 102a as a function of γ . $\oplus$ Jones et al. (1968),

     $\bullet$ Smith and Stewart (1966), + Crispin and Hayman

        (1964).

Fig. 3
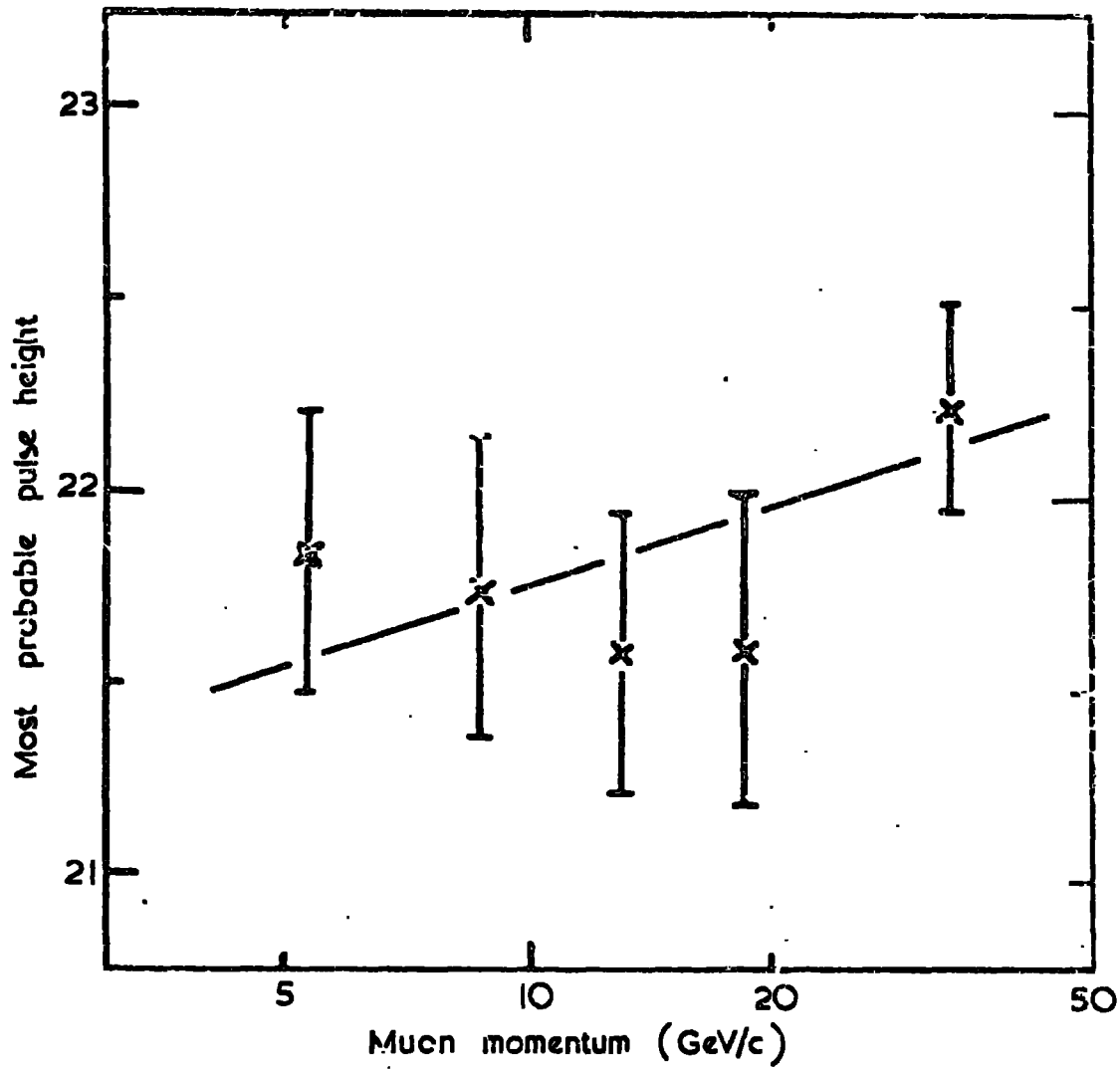
Fig. 1
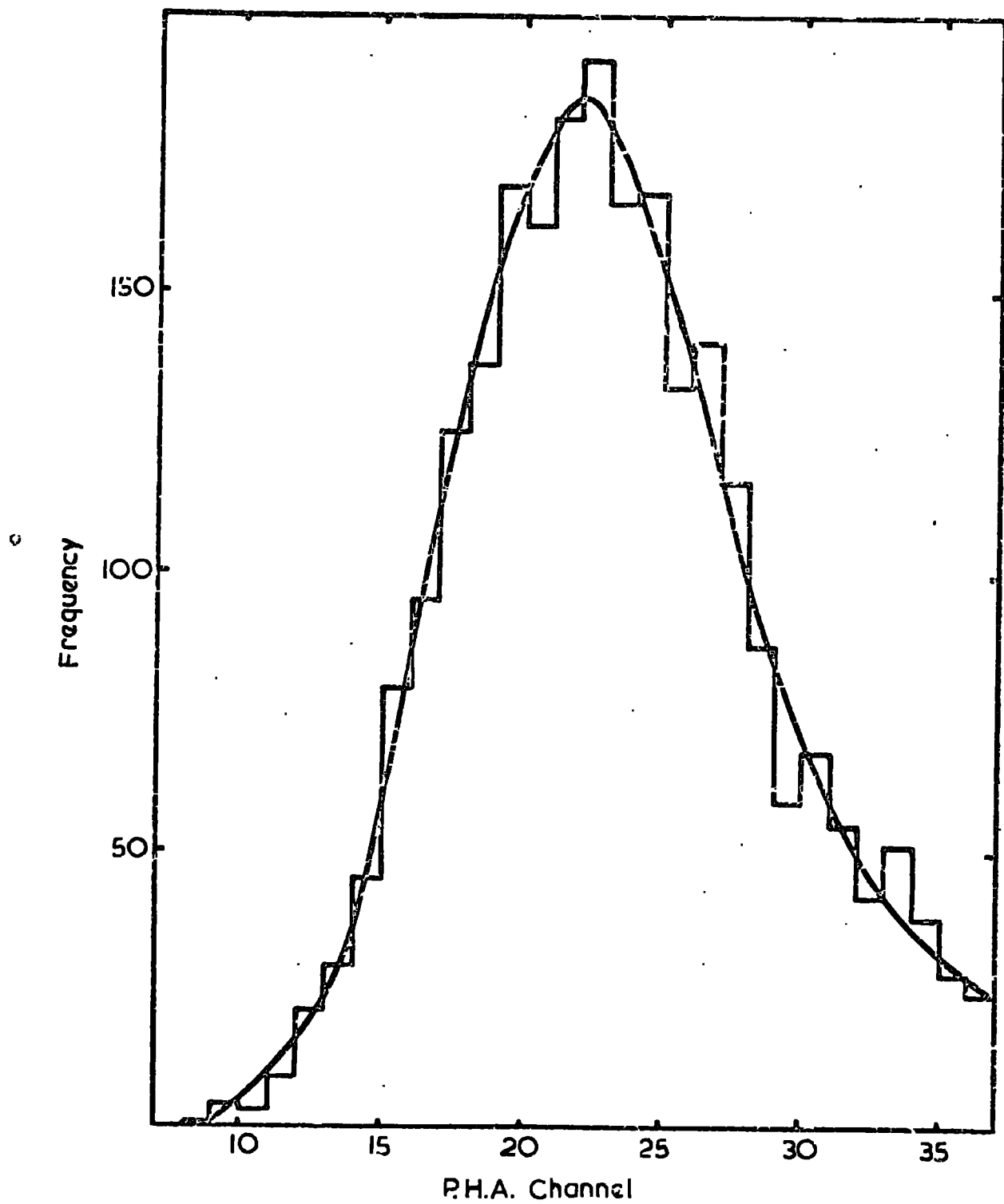
Fig. 2
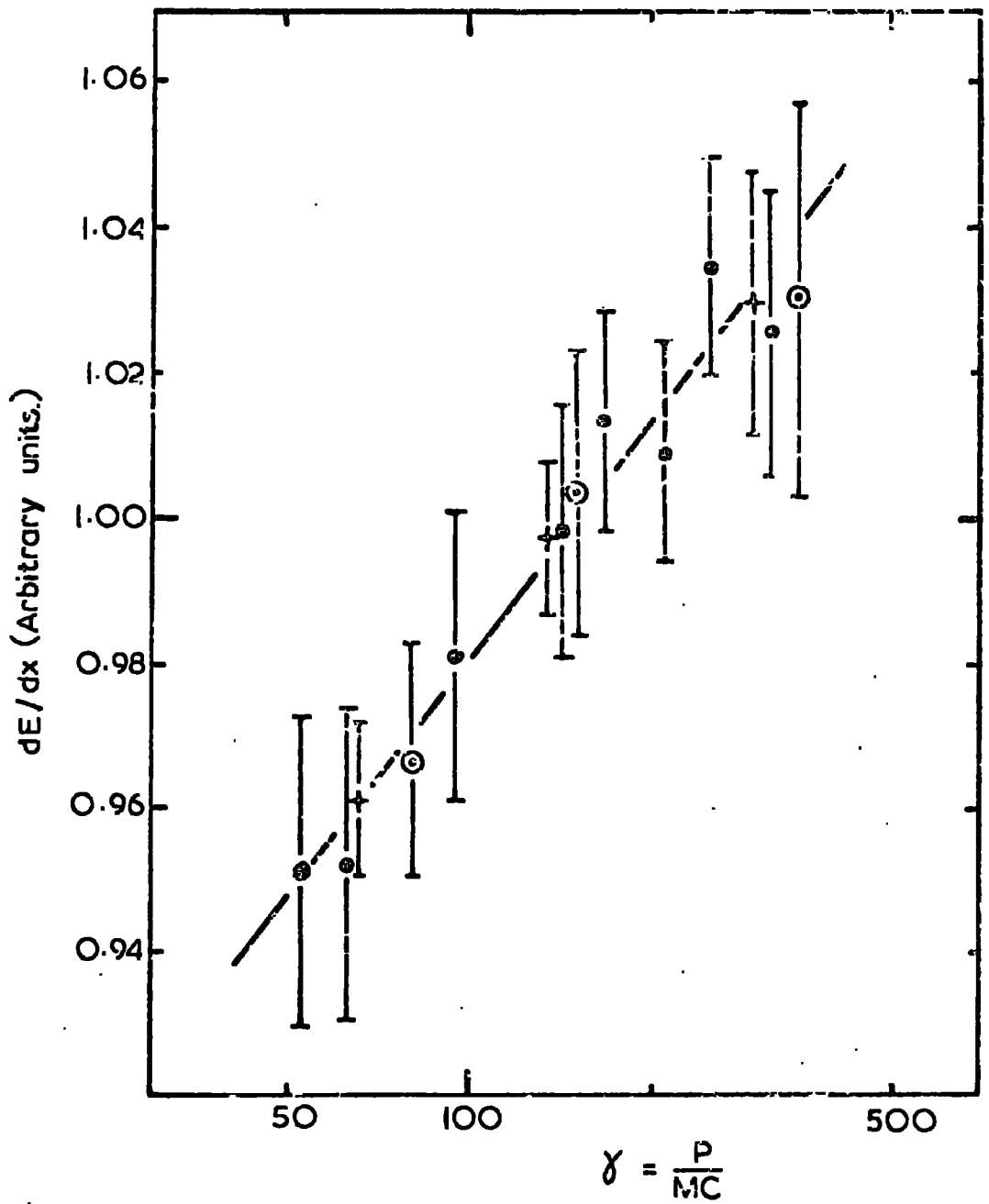
References for Appendix A .

Ashton, F., et al., 1965, Nucl. Inst. & Methods, $\underline{37}$, 181-2.

Bowen, T., 1954, Phys. Rev., $\underline{96}$, 754.

Crispin, A., and Hayman, P.J., 1964, Proc. Phys. Soc., $\underline{83}$, 1051-8.

Jones, I.S. et al., 1968, J. Phys. A (Proc. Phys. Soc.) $\underline{1}$, 584-7.

Smith, A.M., and Stewart, D.T., 1966, Phys. Letts., $\underline{22}$, 633-5.

Sternheimer, R.M., 1952, Phys. Rev., $\underline{88}$, 851- 9.

$\qquad$ 1953a,Phys. Rev., $\underline{89}$, 1148.

$\qquad$ 1953b,Phys. Rev., $\underline{91}$, 256 - 65.

$\qquad$ 1956, Phys. Rev., $\underline{103}$, 511 - 5.

$\qquad$ 1967, Phys. Rev., $\underline{164}$, 349 - 51.

APPENDIX B1

Data Representation

If N+ and N- represent a sample of positive and negative muons, each with respective error σ_+ and σ_- , then the expected error on the charge ratio, R = N+/N-, follows from the general relation

$$\sigma_R = \left[\left(\frac{\partial R}{\partial N+} \right)^2 \cdot \sigma_+^2 + \left(\frac{\partial R}{\partial N-} \right)^2 \cdot \sigma_-^2 \right]^{\frac{1}{2}}$$

$$= R \left[\left(\frac{\sigma_+}{N+} \right)^2 + \left(\frac{\sigma_-}{N-} \right)^2 \right]^{\frac{1}{2}} \qquad (B1.1)$$

Providing that the variation in N+ and N- are of Poissonian form, then for large N, when $\sigma_\pm = \sqrt{N_\pm}$, equation B1.1 reduces to

$$\sigma_R = R \left(\frac{1}{N+} + \frac{1}{N-} \right)^{\frac{1}{2}}. \qquad (B1.2)$$

This relationship is the one used by previous workers. This description, however, can be seen to be anomalous from a consideration of the following discussion.

Let us suppose that a random sample of particles, having a charge ratio R' = N+/N-, with a standard deviation σ_R' as given by equ. (B1.2), is selected from an infinite distribution of particles containing equal numbers of positive and negative particles. If R'' = N-/N+, then the corresponding standard deviation in this inverse description is $\sigma_R'' = \sigma_R'(R''/R')$; the charge ratio of the parent distribution remains unchanged in such a change of description. As the deviation of the sample's ratio from the parent ratio should be independent of the particular description used, then $(1.0 - R'')/\sigma_R''$ and $(R' - 1.0)/\sigma_R'$, which define the deviation for each description, should be equal in magnitude. Representing R'' and σ_R'' in terms of R' and σ_R', then

$$(1.0 - R'')/\sigma_R'' \longrightarrow (1.0 - R'^{-1}) \, R'^2/\sigma_R' = R'(R'-1.0)/\sigma_R'. \qquad (B1.3)$$

The deviation for the two description clearly differ by the factor R'.

This anomaly shows the inadequency of the charge ratio representation and arises from the asymmetry in the possible values that the charge ratio can take. Similarly, these comments must apply to the statistical analysis using any asymmetric representation. The important consequence of such a description, in the analysis of charge ratio data, is to give excessive weighting to the smallest ratios encountered. Depending on the values of the ratio itself, this effect is independent of the size of the sample.

This anomaly may be avoided if the data is interpreted in terms of the excess of one type of the sample over the other. The charge excess δ may be defined as

$$\delta = (N_+ - N_-)/(N_+ + N_-) \qquad (B1.4)$$

The standard deviation σ_δ is as follows

$$\sigma_\delta = \frac{2}{(N_+ + N_-)^2} \cdot \left[(N_+ \sigma_+)^2 + (N_- \sigma_-)^2 \right]^{\frac{1}{2}} \qquad (B1.5)$$

and for $\sigma_\pm = (N_\pm)^{\frac{1}{2}}$ reduces to

$$\sigma_\delta = \frac{2}{(N_+ + N_-)^2} \cdot \left[N_+^3 + N_-^3 \right]^{\frac{1}{2}}. \qquad (B1.6)$$

Clearly, the magnitude of δ and σ_δ are unaltered by an exchange of N_+ with N_- as is required.

APPENDIX   B2

Error Propagation

Due to the nature of the production of single cosmic ray muons, the Poissonian distribution lends itself to the description of the muon sampling errors as quoted in the previous section. In certain cases, however, modifications to this description are necessary as may be seen from the following example of the local scattering of cosmic ray muons arriving at sea level.

For the purposes of a Monte Carlo analysis of the effect of Coulomb scattering of muons arriving at sea level prior to detection, it was necessary to construct a scattering model. Muons were assumed to arrive at sea level in the fixed proportions as presented in table B2.1. The individual muons from each zenith cell were randomly scattered in turn according to the r.m.s. angle of scatter in the zenith, σ_{total}. The contributions to σ_{total} were from scattering in the structures of a local building and in the steel and barytes screening of the Durham Horizontal Air Shower Array. A contribution to σ_{total} from atmospheric scattering was also included; this being justified by a consideration of the fact that the majority of the muon energy loss and Coulomb scattering, occur near sea level as a consequence of the increasing atmospheric density with depth.

Using the fixed incident spectra 20 independent Monte Carlo operations were performed. The number of scattered muons from all cells, arriving in the zenith cell $82.5^{\circ} - 85^{\circ}$, are recorded in table B2.2. together with the calculated charge excesses. Without

TABLE   B2.1

THE 2.0 GeV MUON SCATTERING MODEL

Zenith Angle (degrees)	Spectra N_+	N_-	σ_{total} (degrees)	Contributions to σ_{total}			
				$\sigma_{building}$	σ_{array}	σ_{air}^+	σ_{air}^-
88.75	0.2	2.8	2.17	1.27	0	1.76	1.80
86.25	1.95	10.9	2.20	1.27	0	1.79	1.82
83.75	10.5	30.5	2.71	1.27	1.56	1.82	1.82
81.25	35.25	66.75	2.39	0	1.56	1.82	1.82
78.75	87.15	128.6	2.38	0	1.56	1.80	1.80
76.25	220.9	271.5	2.01	0	0.90	1.79	1.79

TABLE   B2.2.

<u>RESULTANT   DATA   AFTER   SCATTERING   IN   THE   ZENITH   CELL 82.5^{o}-85°</u>

Run	N_+	N_-	Charge Excess	Run	N_+	N_-	Charge Excess
1	19	48	-0.463.	11	18	38	-0.357
2	30	40	-0.143.	12	15	46	-0.508
3	26	36	-0.161.	13	26	23	-0.061
4	22	43	-0.323.	14	21	39	-0.300.
5	26	34	-0.133.	15	21	47	-0.382.
6	19	42	-0.404.	16	20	50	-0.429.
7	29	52	-0.284.	17	23	42	-0.292.
8	17	51	-0.500.	18	25	48	-0.315.
9	28	45	-0.233.	19	19	43	-0.387.
10	19	39	-0.345.	20	20	37	-0.298.

scattering, the expected charge excess at a zenith angle of 83.75°,
has a unique value of -0.488 but on scattering of the fixed spectra,
a value of -0.311 with a standard deviation of 0.135 was returned.
The scattered sample typically contained 60 particles.

The above approach to the scattering problem does not allow for
the possibility of statistical variations of the incident spectra
which are expected to be of Poissonian form. The effect of imposing
Poissonian variations on the incident spectra used, would have been
to produce an increased spread in the deviations of the computed
scattered excesses about the mean value -0.311. For the present
case, the standard deviation, considering only Poissonian fluctuations,
would be 0.142 and since the two above mentioned processes are only
weakly dependent, an overall standard deviation of 0.196 would be
expected, representing a 38% increase in the error as expected from
the Poissonian fluctuations alone.

Although the above effect has been included in the treatment of
the present spectrograph's data for those energies where scattering
was important, of further significance is its application to the
problem of analysing data obtained beyond the m.d.m. of all spectrographs.
The limited resolution of spectrographs in high energy measurements
causes similar increases in the number of "binomial channels" opened
by the uncertainty in muon momentum and charge determinations.

ACKNOWLEDGEMENTS